COPPE
UFRJ
Instituto Alberto Luiz Coimbra de
Pós-Graduação e Pesquisa de Engenharia

# SYNCHRONVERTER-BASED STATCOM CONTROL WITH VOLTAGE IMBALANCE COMPENSATION

Lucas do Nascimento Gomes

Dissertação de Mestrado apresentada ao Programa de Pós-graduação em Engenharia Elétrica, COPPE, da Universidade Federal do Rio de Janeiro, como parte dos requisitos necessários à obtenção do título de Mestre em Engenharia Elétrica.

Orientadores: Robson Francisco da Silva Dias
Luis Guilherme Barbosa Rolim

Rio de Janeiro
Agosto de 2020

# SYNCHRONVERTER-BASED STATCOM CONTROL WITH VOLTAGE IMBALANCE COMPENSATION

Lucas do Nascimento Gomes

DISSERTAÇÃO SUBMETIDA AO CORPO DOCENTE DO INSTITUTO ALBERTO LUIZ COIMBRA DE PÓS-GRADUAÇÃO E PESQUISA DE ENGENHARIA DA UNIVERSIDADE FEDERAL DO RIO DE JANEIRO COMO PARTE DOS REQUISITOS NECESSÁRIOS PARA A OBTENÇÃO DO GRAU DE MESTRE EM CIÊNCIAS EM ENGENHARIA ELÉTRICA.

Orientadores: Robson Francisco da Silva Dias
Luis Guilherme Barbosa Rolim

Aprovada por: Prof. Robson Francisco da Silva Dias
Prof. Luis Guilherme Barbosa Rolim
Dr. Emanuel Leonardus van Emmerik
Prof. Bruno Wanderley França

RIO DE JANEIRO, RJ - BRASIL
AGOSTO DE 2020

Gomes, Lucas do Nascimento

Synchronverter-based STATCOM Control With Voltage Imbalance Compensation/Lucas do Nascimento Gomes. – Rio de Janeiro: UFRJ/COPPE, 2020.

XIII, 96 p.: il.; 29, 7cm.

Orientadores: Robson Francisco da Silva Dias
Luis Guilherme Barbosa Rolim

Dissertação (mestrado) – UFRJ/COPPE/Programa de Engenharia Elétrica, 2020.

Referências Bibliográficas: p. 85 – 93.

1. Eletrônica de Potência. 2. Qualidade de Energia. 3. Desbalanço de tensão. 4. Synchronverter. 5. STATCOM. I. Dias, Robson Francisco da Silva *et al.* II. Universidade Federal do Rio de Janeiro, COPPE, Programa de Engenharia Elétrica. III. Título.

*A minha esposa, pelo*
*companheirismo, compreensão e*
*paciência.*

# Agradecimentos

Gostaria de agradecer primeiramente a Deus por ter me dado a oportunidade de viver, continuar vivendo e ter chegado até aqui.

A minha mãe Andréa Alves do Nascimento, pelo apoio incondicional e quitudes que alegram até defunto.

Ao meu pai Mauro Barbosa Gomes, que, através da música, volta e meia me lembra e relembra da alegria de viver.

A minha esposa, Paula Padilha Cerqueira, por ter me acompanhado durante todo esse árduo processo, cheio de altos e baixos, alegrias imensas, tristezas profundas, muito aprendizado e crescimento pessoal. Seu amor, apoio, paciência, compreensão me ajudaram a chegar aqui sendo uma pessoa muito melhor (embora nem sempre pareça).

A minha irmã Victoria do Nascimento Gomes pelo ombro amigo em momentos difíceis, mesmo quando muitas vezes não pude/soube fazer o mesmo por ela.

Aos meus orientadores, Prof. Robson Dias e Prof. Luis Guilherme Barbosa Rolim, por terem compartilhado seu imenso conhecimento comigo e todos a sua volta, acreditado no meu trabalho e fornecido ideias cruciais para o desenvolvimento do mesmo.

A família do ELEPOT: Laís, André A., Elienai, Paulo, Gleydson, Lauro e tantos outros. Nós ganhamos o concurso da Typhoon e levamos o HIL pra casa!

Ao Armando Ferreira, um irmão que ganhei na UFRJ e vou levar para a vida! Foi muito bom poder compartilhar os momentos bons e ruins dessa empreitada com você meu amigo. Obrigado pelas conversas profundas, pelas noites em claro no laboratório tentando botar o maldito *LaunchPad* para funcionar, por toda ajuda, desde a dúvida banal de uma disciplina até a revisão de artigo.

Por fim, concluo agradecendo a banca pelas sugestões dadas a este trabalho e ao apoio financeiro da CAPES e INERGE.

Resumo da Dissertação apresentada à COPPE/UFRJ como parte dos requisitos necessários para a obtenção do grau de Mestre em Ciências (M.Sc.)

# CONTROLE DE STATCOM BASEADO EM *SYNCHRONVERTER* COM COMPENSAÇÃO DE DESBALANÇO DE TENSÃO

Lucas do Nascimento Gomes

Agosto/2020

Orientadores: Robson Francisco da Silva Dias
Luis Guilherme Barbosa Rolim

Programa: Engenharia Elétrica

Neste trabalho, um controle baseado em *synchronverter* é proposto para operar um STATCOM como compensador síncrono. Além disso, para lidar com condições de desequilíbrio de tensão que podem aparecer na rede, um novo método de compensação de desequilíbrio de tensão é desenvolvido para funcionar em harmonia com os modos de operação do controle principal. O modelo de gerador síncrono usado é derivado de um modelo de máquina CA genérica na representação de vetor espacial. Detalhes práticos sobre o projeto do controlador são abordados, bem como um modelo de pequenos sinais para análise de estabilidade e parametrização. Dois cenários são simulados: um sistema em grande e outro pequena escala, sendo este último utilizado como uma etapa de validação para implementação em protótipo experimental. As simulações e os resultados experimentais confirmam um desempenho satisfatório do controle proposto.

Abstract of Dissertation presented to COPPE/UFRJ as a partial fulfillment of the requirements for the degree of Master of Science (M.Sc.)

# SYNCHRONVERTER-BASED STATCOM CONTROL WITH VOLTAGE IMBALANCE COMPENSATION

Lucas do Nascimento Gomes

August/2020

Advisors: Robson Francisco da Silva Dias
Luis Guilherme Barbosa Rolim

Department: Electrical Engineering

In this work, a synchronverter-based control strategy is proposed to operate the STATCOM as a synchronous compensator. Moreover, to cope with unbalanced conditions that may appear at the grid, a novel voltage imbalance compensation control is developed to work harmoniously with the main synchronverter model. The used base synchronous generator model is derived from a general AC machine in space vector representation. Practical details about the controller design are addressed as well as a small-signal model for stability analysis and parameter tuning. Two scenarios are simulated: large-scale and small-scale system, the latter being used as a validation step for implementation in a small experimental setup. Both simulations and experimental results confirm the suitable performance of the proposed control.

# Contents

**List of Figures** **x**

**List of Tables** **xiii**

**1 Background and Motivation** **1**
1.1 Introduction . . . . . . . . . . 2
1.2 Objectives . . . . . . . . . . 4
1.3 Document Structure . . . . . . . . . . 4

**2 Overview of the Synchronverter Concept** **6**
2.1 Synchronverter concept . . . . . . . . . . 9
2.2 Non-generating Synchronverters . . . . . . . . . . 14
2.3 Power Quality Applications . . . . . . . . . . 17
2.4 Partial conclusions . . . . . . . . . . 20

**3 Synchronous Generator model in the $\alpha\beta$ reference frame** **21**
3.1 General symmetric AC machine model in space vector representation 22
3.2 Synchronous generator model . . . . . . . . . . 24

**4 S-STATCOM Proposed Control Scheme** **29**
4.1 Control Strategies to Mitigate Voltage Imbalance . . . . . . . . . . 30
4.2 S-STATCOM Model . . . . . . . . . . 33
4.2.1 CL 1: Startup and Synchronization . . . . . . . . . . 34
4.2.2 CL 2: Active power loop . . . . . . . . . . 36
4.2.3 CL 3: Decoupled Reactive power and Voltage Regulation Loops 37
4.2.4 Voltage Imbalance Compensation Loop . . . . . . . . . . 39
4.3 Small-signal model . . . . . . . . . . 41

**5 Evaluation of the Proposed Control** **47**
5.1 The Implementation Process . . . . . . . . . . 48
5.1.1 Simulation time-step . . . . . . . . . . 49
5.1.2 Model Discretization . . . . . . . . . . 49

5.1.3 Simulation fine-tuning . . . . . . . . . . . . . . . . . . . . . . 52
5.2 Simulation Results - Scenario 1: 25 kV Distribution Feeder setup . . 53
5.2.1 Case 1: S-STATCOM Main modes . . . . . . . . . . . . . . . . 56
5.2.2 Case 2: Voltage Imbalance Compensation . . . . . . . . . . . 60
5.3 Simulation Results - Scenario 2: Small-scale, grid connected setup . . 63
5.3.1 Startup and grid connection . . . . . . . . . . . . . . . . . . . . 64
5.3.2 S-STATCOM Operation Modes . . . . . . . . . . . . . . . . . . 65
5.3.3 Voltage Imbalance Compensation . . . . . . . . . . . . . . . . . 67
5.4 S-STATCOM Small-Scale Experimental Setup . . . . . . . . . . . . . 71
5.4.1 Voltage measuring circuit . . . . . . . . . . . . . . . . . . . . . 73
5.4.2 Startup Sequence . . . . . . . . . . . . . . . . . . . . . . . . . . 75
5.4.3 DSP code implementation . . . . . . . . . . . . . . . . . . . . . 75
5.4.4 Experimental Results . . . . . . . . . . . . . . . . . . . . . . . . 76
5.4.5 Voltage Imbalance Compensation . . . . . . . . . . . . . . . . . 80
5.5 Results discussion . . . . . . . . . . . . . . . . . . . . . . . . . . . . 81

**6 Conclusions and Future Work** **83**

**Bibliography** **85**

**A Space Vector Concept** **94**

# List of Figures

2.1 Emulation of synchronous machine [1]. . . . . . . . . . . . . . . . . . . 7
2.2 Comparison between synchronous machine emulation strategies. . . . 8
2.3 Synchronverter power part from [2]. . . . . . . . . . . . . . . . . . . . . . 10
2.4 Synchronverter control block diagram [2]. . . . . . . . . . . . . . . . . . 13
2.5 Synchronverter-based STATCOM from Nguyen *et al* [3] . . . . . . . . 15
2.6 Non-generating synchronverter used in [4] . . . . . . . . . . . . . . . . 16
2.7 Improved non-gerenerating synchronverter from [5]. . . . . . . . . . . 17
2.8 Synchronverter based control to compensate grid harmonics by Conrado *et al*[6]. (a) One-line diagram of the system showing control blocks; (c) Multi-frequency tuned PR controller transfer function; (b) Current controller for harmonic compensation. . . . . . . . . . . . 18
2.9 Synchronverter with resonant harmonic compensator proposed in [7]. (a) Detailed synchronverter control structure; (b) Synchronverter with resonant harmonic compensator . . . . . . . . . . . . . . . . . . 19

3.1 Symmetrical AC machine . . . . . . . . . . . . . . . . . . . . . . . . . . . 24
3.2 a) Equivalent rotor circuit for a Permanent Magnet Synchronous Motor; b) Adapted virtual rotor circuit for the synchronous generator model. . . . . . . . . . . . . . . . . . . . . . . . . . . . . . . . . . 25
3.3 Synchronous generator in the stationary frame . . . . . . . . . . . . . 28

4.1 DSOGI+PNSC structure [8][9]. . . . . . . . . . . . . . . . . . . . . . . . 32
4.2 Double Synchronous Reference Frame Current Controller. . . . . . . . 32
4.3 Proposed S-STATCOM control strategy. . . . . . . . . . . . . . . . . . . 34
4.4 S-STATCOM one-line diagram . . . . . . . . . . . . . . . . . . . . . . . 36
4.5 Grid unbalance control strategy . . . . . . . . . . . . . . . . . . . . . . 40
4.6 Small-signal model of S-STATCOM without DC bus voltage PI controller. . . . . . . . . . . . . . . . . . . . . . . . . . . . . . . . . . . . . 42
4.7 Block diagram of S-STATCOM small-signal model with PI controller 43
4.8 Bode plots of each S-STATCOM transfer function . . . . . . . . . . . 44
4.9 Phase Margin of $\Delta P/\Delta V_{dc}^{*}$ for different $K_i/K_p$ values. . . . . . . . . . 45

4.10 Root loci of $\Delta P/\Delta V_{dc}^{*}$ for different $K_{i_V dc}/K_{p_V dc}$ values, with focus on the design region. . . . . . . . . . . . . . . . . . . . . . . . . . . . 46

5.1 Bode-diagram of PR-controller for comparison of discretization methods. $T_s = 160\ \mu s$, $K_p = 0.1$, $K_r = 100$, $\omega_c = 3.77\ rad/s$ . . . . . . . . 51
5.2 Grid used for analysis of D-STATCOM in [10] . . . . . . . . . . . . . 54
5.3 IGBT model used in the three-phase bridge model in Simulink. . . . . 55
5.4 3-ph diagram of S-STATCOM converter structure for Scenario 1 simulations . . . . . . . . . . . . . . . . . . . . . . . . . . . . . . . . . . 56
5.5 One-line diagram of the Case 1 system . . . . . . . . . . . . . . . . . 57
5.6 S-STATCOM Synchronization Process: a) Phase A Voltages, b) back-EMF and Grid Voltage Amplitudes, c) Phase A voltage difference, d) Power angle . . . . . . . . . . . . . . . . . . . . . . . . . . . . . . . 58
5.7 S-STATCOM Main Modes: a) Frequency tracking by CL1a, b) DC bus voltage transients, c) Grid and back-EMF voltage amplitudes, d) Active Power, e) Reactive Power, f) Power angle $\delta$ . . . . . . . . . . . 59
5.8 One-line diagram of the Case 2 system . . . . . . . . . . . . . . . . . 60
5.9 Results for Scenario 1 modes when VIC is on. a) Frequency tracking by CL1a; b) DC bus voltage; c) Internal and grid voltage amplitudes; d) Reactive power . . . . . . . . . . . . . . . . . . . . . . . . . . . . 62
5.10 Effect of the voltage imbalance on load L1 and subsequent activation of S-STATCOM's VIC mode. . . . . . . . . . . . . . . . . . . . . . . 62
5.11 VIC performance of the S-STATCOM in Scenario 1. a) Phase voltages before and after VIC activation. b VUF throughout the simulation . 63
5.12 S-STATCOM line currents when VIC is activated. . . . . . . . . . . . 64
5.13 S-STATCOM power circuit . . . . . . . . . . . . . . . . . . . . . . . . 65
5.14 Simulation results for Synchronism mode in Scenario 2. (a) DC Voltage at the capacitor, (b) Three-phase line currents, (c) Internal voltage $E$ (red) and Grid voltage $V_g$ (blue) amplitudes (d) Voltage difference $e_a - v_{ga}$, (e) Power angle, (f) Grid Frequency tracking. . . . . . 66
5.15 Simulation results for the remaining operation modes of Scenario 2. (a) DC bus capacitor voltage. (b) Active Power (c) Reactive power. (d) Grid (blue) and internal (red) voltage amplitudes. (e) Grid frequency tracking. . . . . . . . . . . . . . . . . . . . . . . . . . . . . 67
5.16 S-STATCOM power circuit with $Z_U$ added to phase C to create voltage imbalance . . . . . . . . . . . . . . . . . . . . . . . . . . . . . . . 68
5.17 Simulation results for VIC-mode in Scenario 2. (a) Three-phase grid voltages (b) Voltage Unbalance Factor $V^{-}/V^{+}$ throughout the simulation. . . . . . . . . . . . . . . . . . . . . . . . . . . . . . . . . . 69

5.18 Results for Scenario 2 modes when VIC is on. a) Frequency tracking by CL1a; b) DC bus voltage; c) Internal and grid voltage amplitudes; d) Reactive power . . . . . . . . . . . . . . . . . . . . . . . . . . . . . 70
5.19 S-STATCOM line currents when VIC is activated . . . . . . . . . . . 70
5.20 Texas Instruments development kit LaunchXL-F28377S, now discontinued . . . . . . . . . . . . . . . . . . . . . . . . . . . . . . . . . . 71
5.21 BoosterPack BOOSTXL-DRV8305EVM add-on for the LauchPad . . 72
5.22 S-STATCOM experimental prototype . . . . . . . . . . . . . . . . . . 73
5.23 Voltage sensor used in the experimental small-scale prototype . . . . 74
5.24 Three-phase currents at system startup i.e. DC bus capacitor precharge. . . . . . . . . . . . . . . . . . . . . . . . . . . . . . . . . . 76
5.25 Step-up ramp on the DC bus voltage reference. . . . . . . . . . . . . 77
5.26 DC Voltage and line current transients for a -1 pu Reactive power order. (a) $V_{dc}$ (blue) and $i_{abc}$ on the oscilloscope screen. (b) $V_{dc}$ signal acquired from the oscilloscope. . . . . . . . . . . . . . . . . . . . . . . 77
5.27 (a) Phase voltages A and B (blue and red) and line currents A and B (green and orange) for the S-STATCOM experimental setup in q-mode @ $q_{ref} = -1pu$; (b) Calculated reactive power signal in q-mode with an average value of -79.82 VAr . . . . . . . . . . . . . . . . . . 78
5.28 V-mode measurements data, with $V_{ref} = 1.0pu$. (a) $V_{dc}$ and $i_{abc}$ transients when switching from Q to V-mode. (b) Three-phase voltages at V-mode on steady-state. . . . . . . . . . . . . . . . . . . . . . . . 79
5.29 Droop-mode measurements. (a) $V_{dc}$ and $I_{abc}$ transients when switching from V to Droop-mode. (b) Phase voltages A and B (blue and red) and line currents A and B (green and orange). (c) Three-phase voltages at Droop-mode on steady-state. (d) Calculated reactive power signal in Droop-mode with an average value of -48.69 VAr . . . . . . 79
5.30 Initial unbalanced grid conditions. (a) Three-phase (phase-neutral) voltages: A in blue, B in red and C in green. (b) Three-phase (line) currents: A in red, B in green and C in orange. . . . . . . . . . . . . 80
5.31 Measurements for VIC-mode. (a) VIC-mode activation transients of the three-phase voltages, (b) Three-phase voltages at steady-state with VIC-mode activated, (c) VIC-mode activation transients of the three line currents, (d) Three line currents at steady-state with VIC-mode activated. . . . . . . . . . . . . . . . . . . . . . . . . . . . . . 81

# List of Tables

4.1 S-STATCOM's Operation Modes. . . . . . . . . . . . . . . . . . . . . . 35

5.1 Scenario 1 Grid parameters. . . . . . . . . . . . . . . . . . . . . . . . . . 54
5.2 Scenario 1 Converter parameters. . . . . . . . . . . . . . . . . . . . . . 55
5.3 Scenario 1 Control parameters. . . . . . . . . . . . . . . . . . . . . . . . 57
5.4 Converter losses comparison for case 2, Scenario 1. . . . . . . . . . . . 61
5.5 Scenario 2 converter parameters. . . . . . . . . . . . . . . . . . . . . . . 64
5.6 Scenario 2 Control parameters. . . . . . . . . . . . . . . . . . . . . . . . 65

# Chapter 1

# Background and Motivation

This chapter presents a background and motivation for this thesis. At the end, the document's structure is outlined.

## 1.1 Introduction

The use of renewable energy resources to supply the ever growing demand is changing the way how power grids are operated. Wind and solar photovoltaic (PV) Distributed Generation (DG) units rely on power electronic systems to connect and exchange power with the grid, due to their intermittent nature [11] and inherent grid frequency incompatibility. They also have little to no mechanical inertia, thus if they are not connected to an energy storage system, the overall grid inertia will be reduced, compromising the system stability and power quality[12]. For microgrid control and protection, those are challenges that deserve special attention [13].

From a power quality point of view, the presence of non linear loads along with those DG converters units contribute to a high harmonic current injection in the microgrid, which may cause interference in communication systems, increase in losses and spurious tripping of circuit breakers. Voltage and current unbalance due to uneven distribution of single-phase loads and DG units are also a concern for microgrid operation and control. Such conditions increase losses due to excessive neutral current in the distribution feeder, reduce the transformer capacity and, in synchronous machines, produce an oscillating active power component at double system frequency causing excessive vibration and mechanical stress, thus reducing its efficiency[14]. Therefore, great effort is being employed to mitigate or solve those issues[15].

To handle power system stability issues, synchronous condensers (SCs) and static synchronous compensators (STATCOMs) are well known to have satisfactory performance dealing with frequency and voltage deviations within both bulk power systems and microgrids [16–18]. For power quality issues, series and shunt active filters are used in [19] to compensate source voltage unbalance and current harmonics, while [20] utilizes an unified power quality compensator (UPQC) to provide a complete compensation solution at the point of common coupling (PCC). A microgrid unbalance compensator is proposed in [21] to compensate the negative effects of unbalanced microgrid operation by using a three-phase four-leg power converter at the PCC, eliminating excessive neutral current. However, with a high penetration of non-inertial DGs, simple addition of these equipments to the grid may not be physically and economically feasible. So, a great deal of research effort is invested in control strategies for power-electronic interfaced DG units to handle stability and power quality issues locally. A local control strategy is proposed in [22] to compensate voltage unbalance in a droop-controlled microgid while sharing the compensation effort without dedicated communication between DG units, whilst [23] creates a set of primary (local) and secondary (centralized) controls to compensate voltage unbalance in the same conditions.

A control strategy that has become popular in recent years is the concept of

Static Synchronous Generators [24], which consists of making a power-electronic interfaced DG mimic the behavior of a synchronous machine from the point of view of the power system operator. In literature, some schemes go by different names: Virtual Synchronous Generators or Virtual Synchronous Machines (VSG or VSM/VISMA)[1, 25] and Synchronverters [2]. They have some structural differences between them, however, both show great potential in dealing with stability and power quality issues for bulk power systems and microgrids. The reasons for this are: (i) decades of experience with control and stability studies for synchronous machines that can be directly applied to these solutions; (ii) some variables of their mathematical models are no longer bound by the physical characteristics of conventional generators, meaning they can be dynamically changed in real-time within the physical limits of the controlled converter, i.e. rotor inertia, presence of damper windings, etc; (iii) possibility of adding control loops to perform different tasks. Several studies have been made exploring the aforementioned features. In [26] and [27], VISMA and VSG algorithms were used, respectively, to make DG units contribute to power system stability and comparing different inertia and droop values, while [28] explores wind and photovoltaic DG integration with the grid using a synchronverter algorithm with a variable inertia function. In [3] the first synchronverter-based STATCOM is introduced, while [4] takes it one step further and designs a modified synchronverter-based Static Var Compensator (SVC) with Power System Stabilizer capabilities to damp electromechanical oscillations.

Few works, however, explored improvement of grid power quality in terms of harmonic content and voltage imbalance. In [29], [30] and [31], the VSG strategy is employed with a comprehensive control framework to compensate current imbalance and active power oscillations under unbalanced grid voltage conditions. Since the VSG is a current control strategy and especially after droop controllers were found to be intrinsically phase-locked loops [32], several works were developed by combining the Double Synchronous Reference Frame (DSRF) current control loop with VSG algorithms, aiming to improve its power delivery performance under unbalanced grid conditions [33] or to compensate voltage imbalance in isolated microgrids [34]. Although they achieved the desired results, this type of control is complex to tune and synchronous reference frame transformations are very computational intensive.

There are even less works with synchronverter based strategies with power quality improvement controls. To compensate harmonic content in the grid, [6] and [7] both employ the synchronverter strategy coupled with resonant or proportional-resonant controllers. In both works, the systems have generator roles and focus on mitigating power quality issues on the grid aiming to improve their own power delivery performance. Therefore, there is a gap in research for synchronverter based solutions aimed exclusively for power quality improvement in distribution and microgrids, especially regarding voltage imbalance.

## 1.2 Objectives

Motivated by the aforementioned issues, the main objective of this thesis is to design a synchronverter-based STATCOM control with a voltage imbalance compensation capability: the S-STATCOM. It is intended to mitigate voltage imbalance at the PCC in distribution and microgrids, while also providing the standard operation modes of a regular STATCOM at the distribution level (D-STATCOM), which are reactive power delivery, voltage support at the PCC and reactive power load sharing through droop control. Also, it has the ability of grid synchronization without the use of Phase-Locked Loop (PLL) or Frequency-Locked Loop circuits. This is achieved by combining the contributions of [3] and [64], respectively.

The starting point was deriving a synchronous generator model in space vector representation from the general AC machine model of [36] that will be used for the S-STATCOM, which will naturally lead to the model equations in the stationary reference frame $\alpha\beta$, thus making the design and implementation of the synchronverter straightforward.

Finally, the voltage imbalance compensation capabilities were implemented through Proportional-Resonant (PR) controllers fed by a Decoupled Second-Order Generalized Integrator (DSOGI). This structure is easily integrated to the main control due to also being in the stationary reference frame, which keeps the tuning and implementation of the whole S-STATCOM control straightforward. By compensating the voltage imbalance at the PCC, it actually supplies the required fundamental frequency oscillating power downstream of the PCC and balances the power flow upstream.

Frequency and time domain analyses were also conducted. In the frequency domain, a small-signal model was developed for the S-STATCOM and its transfer functions for each signal. Input and output relationships were obtained to evaluate its stability and tune the parameters. As for time domain analysis, two simulation scenarios were built in MATLAB/Simulink to evaluate the proposed control performance: a large-scale and small-scale system, the latter being a validation step to implement the control in an experimental setup.

## 1.3 Document Structure

Chapter 2 introduces the current concepts for emulation of synchronous machines and focus on the synchronverter and applications relevant to this work.

Chapter 3 focuses on deriving the synchronous generator model in space vector representation to be used in the S-STATCOM.

Chapter 4 develops the actual S-STATCOM model, describing each of its operation modes. Development of the voltage imbalance compensation and small-signal model are also addressed. In addition, practical details for building the simulations and small-scale experimental setup are discussed.

Chapter 5 shows simulation and experimental results to evaluate the proposed control.

Chapter 6 presents conclusions and suggestions for future work, based on the results and performed analysis.

# List of Publications

There is a manuscript derived from this work under review process with the title:

> L.N Gomes, A.J.G.A Ferreira, R.F.S Dias and L.G.B Rolim, "Synchronverter-based STATCOM with Voltage Imbalance Compensation Functionality", in *IEEE Transactions on Industrial Electronics*.

# Chapter 2

# Overview of the Synchronverter Concept

This chapter presents an overview of the Synchronverter concept. It addresses details of the synchronous generator model, design of control loops and power stage, applications and differences between similar emulated synchronous machine strategies.

Emulation of synchronous machine characteristics as a control strategy to drive inverter-connected energy sources has been a growing trend in this decade. This approach can be divided in two groups: Synchronverters and Virtual Synchronous Generators or Virtual Synchronous Machines (VSG or VSM/VISMA). A quick search on 06/04/2020 in the IEEE database revealed 123 results for Synchronverter and a combined total of 834 for Virtual Synchronous Machine and Virtual Synchronous Generator, which is a significant increase compared to the results found by the author of [5], especially for the Synchronverter concept. Advantages of using this approach include years of experience in modeling and stability studies of synchronous machines, that can be incorporated in the design of VSI control strategies. Also, parameters such as rotor inertia and number of poles are no longer bound by constructive characteristics of the machine and can be chosen or dynamically changed in real-time to meet performance and stability requirements suitable for operation of a grid connected converter, all within its physical constructive limits. In addition, droop control usually embedded in these models allows intermittent renewable energy sources to share power and interact with the power system as synchronous machines do, by allowing the use of secondary and tertiary controls to regulate grid frequency and voltage by the power system operators. Figure 2.1 shows the concept's idea, in which several types of energy sources can be seen as a single synchronous machine connected to the grid.

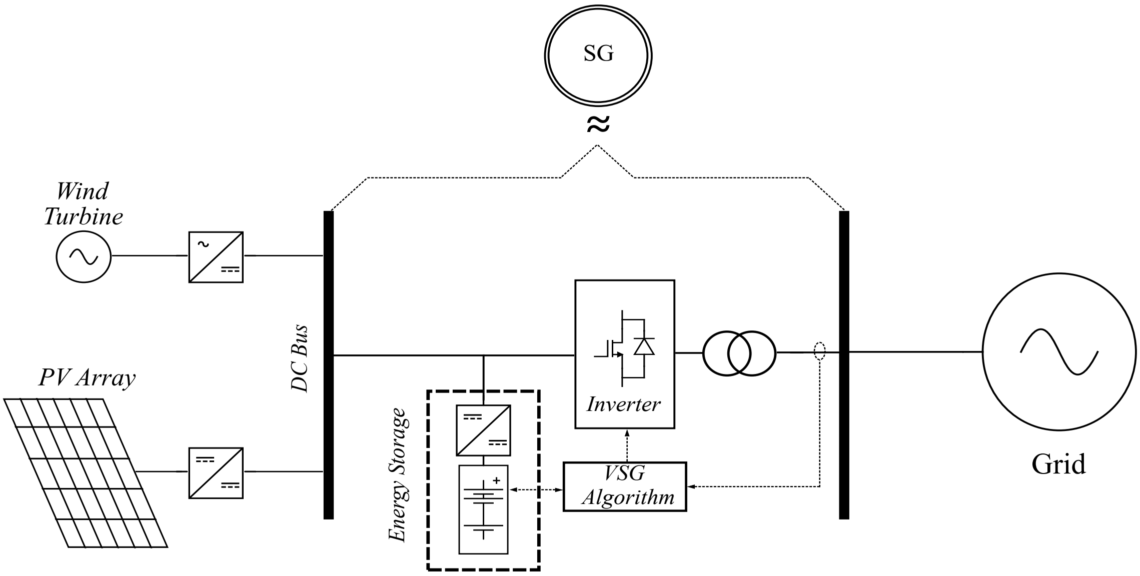

Figure 2.1: Emulation of synchronous machine [1].

As for the control strategies themselves, Synchronverter and VSG or VSM/VISMA both rely on emulating virtual inertia through the swing equation, however, there are some structural differences between them. Although [37] states that VSG and VSM/VISMA are different controls in the sense that the former is voltage controlled and the latter is current controlled, [1], [38] and [39] show examples of the same VSG nomenclature being used for several topologies that can be voltage or current controlled. Therefore, strategies different from the Synchronverter will be referred to as VSG herein. Figures a and b show a basic VSG and Synchronverter control structures, respectively.

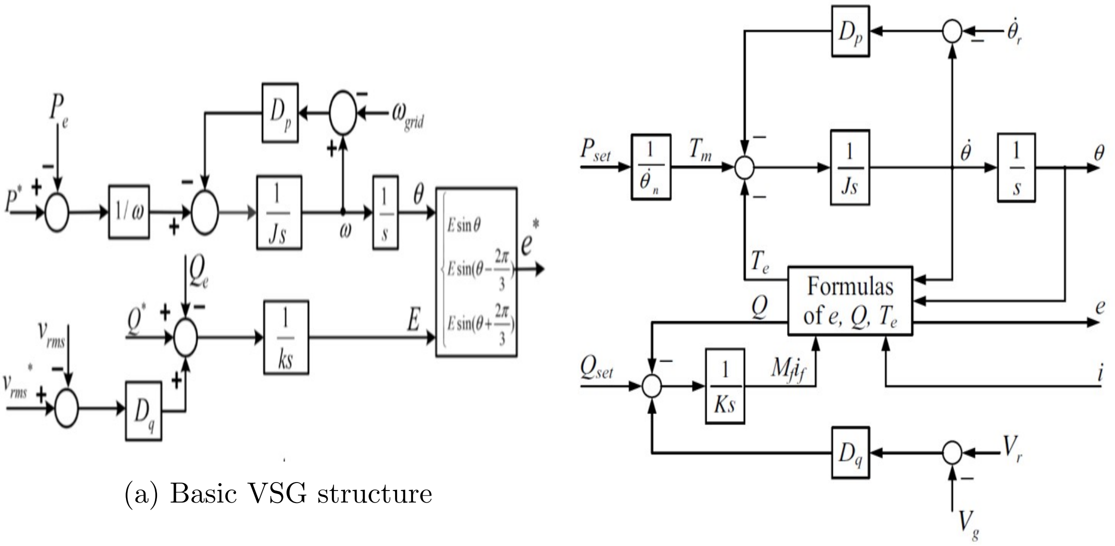

(a) Basic VSG structure

(b) Synchronverter control

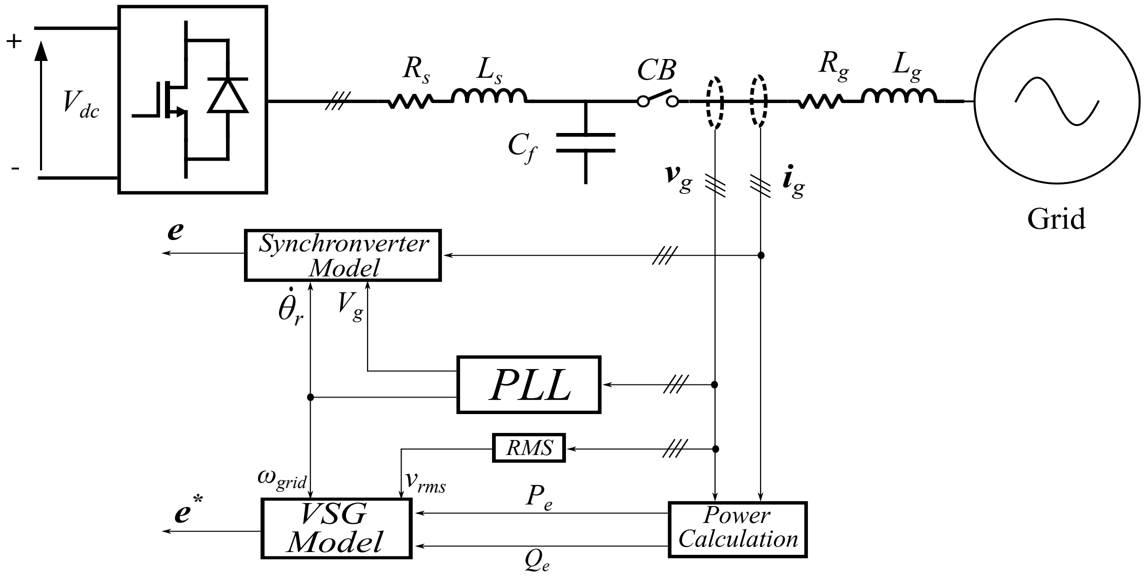

(c) Emulated Synchronous Machine Power Circuit

Figure 2.2: Comparison between synchronous machine emulation strategies.

The main difference that can be observed is that the VSG gets phase and magnitude information for the PWM control signal, $\mathbf{e}^*$, directly from the active and reactive power droop control loops, respectively. Those in turn, rely on accurate power measurements at the PCC for its correct operation. As for the synchronverter, it only needs the PCC current measurement to work, since it calculates reactive power and electrical torque internally through the synchronous machines' dynamic equations [2]. It does need voltage measurement at the PCC for its regulation, but it is not nearly as critical as the one needed in the VSG structure. In addition, the synchronverter was designed to control power electronic converters through its output voltage, while most VSG structures rely on the utilization of virtual impedances or dedicated current control loops to control converters through their output currents, thus requiring additional synchronization circuits, since it requires an active grid to connect. Figure c shows a basic power circuit that can be used by both control strategies, highlighting their main differences. The synchronverter requires a PLL only for initial grid synchronization, while the VSG may depend on its measurements for the entire operation.

Due to the aforementioned reasons and growing research interest in the synchronverter concept, this control structure was chosen to develop the work presented in this thesis. In addition, few works were found in literature that address the synchronverter concept as base control of power quality enhancement, STATCOM or equivalent devices. Therefore, in this chapter, the synchronverter concept will be addressed in detail and some applications in power quality and non-generating devices will be discussed.

## 2.1 Synchronverter concept

The concept of synchronverter is to operate a converter in a way that mimics the behavior of a synchronous machine, by using its dynamic equations [2]. It consists of a power part and an electronic part, i.e, the controller. The power part is a three-phase bridge connected with a LC filter, as shown in Figure 2.3. The filter inductors $L_S$ and resistors $R_S$ represent the series impedance of the virtual stator of the machine, while $L_g$ and $R_g$ represents an equivalent grid impedance, allowing the system downstream of the circuit breaker (CB) to be modeled as an infinite bus. Voltages $v_{abc}$ of the filter capacitors are considered the virtual synchronous machine terminal voltages. $V_{dc}$ is the dc-side voltage of the converter, which is considered to be constant. However, in real world applications, this voltage is tied to a DC source that can be a PV, energy storage, fuel cell, etc, meaning it can no longer be considered constant as its variations represent the available energy at the DC source. Nevertheless, it allows the converter to operate on all of the synchronous machine modes: power sharing through frequency and voltage droop or constant power exchange. For a STATCOM, this voltage is held by a capacitor, which is responsible for supplying converter losses and store enough energy to compensate grid disturbances, the latter being also true for the rotor of a synchronous condenser.

The synchronous machine dynamic model used in this concept is presented with the following considerations [2]: it has a round rotor so that all stator inductances are constant, only one pair of poles per phase so that the mechanical speed of the

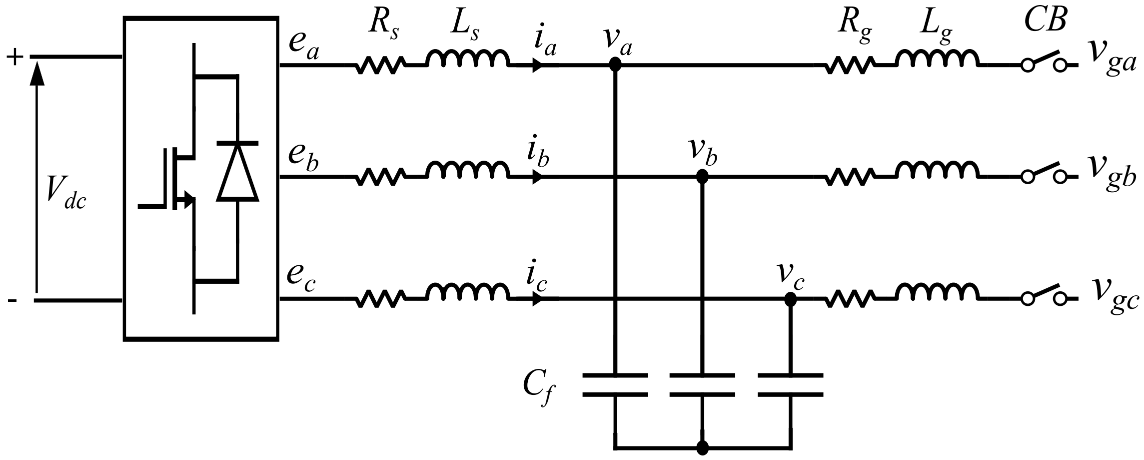

Figure 2.3: Synchronverter power part from [2].

rotor matches the grid frequency, no damper windings in the rotor, no saturation of the iron core and no eddy currents. The equations that describe this model are:

$$\dot{\omega} = \frac{1}{J}[T_m - T_e - D_p(\omega - \omega_{ref})], \tag{2.1}$$

$$T_e = M_f i_f \langle \mathbf{i}, \widetilde{\sin\theta} \rangle, \tag{2.2}$$

$$\mathbf{e} = \omega M_f i_f \widetilde{\sin\theta}, \tag{2.3}$$

$$Q = -\omega M_f i_f \langle \mathbf{i}, \widetilde{\cos\theta} \rangle, \tag{2.4}$$

where

$$\widetilde{\sin\theta} = \begin{bmatrix} sin\theta \\ sin(\theta - \frac{2\pi}{3}) \\ sin(\theta + \frac{2\pi}{3}) \end{bmatrix}, \tag{2.5}$$

$$\widetilde{\cos\theta} = \begin{bmatrix} cos\theta \\ cos(\theta - \frac{2\pi}{3}) \\ cos(\theta + \frac{2\pi}{3}) \end{bmatrix}, \tag{2.6}$$

and $\langle \cdot, \cdot \rangle$ is the vector inner product. Each parameter is described as follows:

- $J$ is the virtual rotor inertia;
- $T_m$ and $T_e$ are the applied mechanical torque and electrical torque, respectively;

- $\omega$ and $\omega_{ref}$ are the actual and reference virtual rotor angular speed, respectively;
- $D_p$ is the damping coefficient;
- $M_f$ is the maximum mutual inductance between the virtual stator windings and virtual field winding;
- $i_f$ is the virtual rotor field winding current;
- $\mathbf{e}$ is the back-electromotive force or back-EMF, also referred to as the internal voltage of the synchronverter;
- $\mathbf{i}$ is the virtual stator current vector;
- $Q$ is the reactive power.

In this model, 2.1 is the classical swing equation. The damping coefficient $D_p$ works as a combination of the virtual mechanical friction losses in the virtual rotor and the frequency-drooping coefficient [2], responsible for active power sharing with other machines and/or inverters with droop control. Since the prominent effect of this parameter is for droop control, it will be referred to as droop coefficient from now on. For non-generating synchronverters, $D_p$ can be 0 since it does not exchange active power with the grid, however, it contributes to stability of the system and its removal must be carefully studied [3][5]. As for equations 2.2, 2.3 and 2.4, they are all proportional to the product of $M_f$ and $i_f$. Since $M_f$ is a constant and $i_f$ is regarded in this model as a constant adjustable parameter [2], they are considered as a single variable $M_f i_f$ that represents the magnetic flux generated by the virtual rotor field circuit. Amplitude of the back-EMF voltage vector $\mathbf{e}$ is given by $E = \omega M_f i_f$, meaning that it is also proportional the virtual machine angular speed, which makes the synchronverter dynamics closer to a real synchronous machine than the VSM strategy.

The electronic part is responsible for calculating this model, which is shown in Figure 2.4. Interaction with the power part is made through the internal voltage signal $\mathbf{e}$, which acts as a three-phase reference signal to be used in a PWM technique. Synchronverter control is achieved through two loops, one of active power and one of reactive power. The active power loop is responsible for regulating the active power output by adjusting the phase angle $\theta$ of the back-EMF voltage through the swing equation. It contains the frequency-droop loop that can be easily tuned through its main parameters, which are the droop coefficient $D_P$ and the virtual inertia $J$. $D_P$ is defined as [2]:

$$D_P = -\frac{\Delta T}{\Delta \omega}, \tag{2.7}$$

which is the ratio between change in total torque and change in angular speed. As for the virtual inertia $J$, since it is not tied to physical constructive aspects of the machine, can be calculated from the loop's time constant $\tau_f = J/D_P$, that can be chosen to meet desired performance requirements. Moreover, the virtual inertia can be expressed as a normalized per unit inertia constant $H$, defined by [40]:

$$H = \frac{\frac{1}{2} J \omega_n^2}{S_{base}}. \tag{2.8}$$

To converter based generation, especially the ones using controls mentioned in this chapter, definition of $H$ can be expanded to:

$$H = \frac{Available/Stored \quad Energy}{System \quad Base \quad Power}, \tag{2.9}$$

which is a more convenient way to associate it with energy storage. Meaning that, with proper controls, PV generators working in setpoints below the MPPT or fast-acting storage units can provide inertial response to the system [12]. For a STATCOM, the per unit moment of inertia $H$ is calculated for the energy stored in the DC bus capacitor:

$$H = \frac{\frac{1}{2} C V_{dc-n}^2}{S_{base}}, \tag{2.10}$$

where $C$ is the capacitance and $V_{dc-n}$ is the nominal voltage of the DC bus. In addition, variable inertia strategies can be employed to achieve improved system dynamics. In [28], this idea is used to couple wind and PV generation through the DC link, since both have intermittent power outputs, i.e., inertial responses. In [41] is implemented an adaptive virtual inertia scheme with fuzzy logic, to improve the dynamic response of a PV generator connected to a microgrid. In [39], adaptive virtual inertia is investigated in detail and proved its effectiveness in damping power and frequency oscillations, while keeping satisfactory system response.

The reactive power loop is in charge of providing reactive power support and voltage regulation at the virtual stator terminals or PCC. Voltage droop constant $D_Q$ is responsible for the reactive power sharing with the grid and/or other converters and synchronous machines with similar functionalities. The constant K is the dual equivalent of J in the reactive power loop and generates the excitation flux $M_f i_f$ from the virtual rotor field circuit [2], as described by the following equation:

$$M_f i_f = \frac{1}{K} \int [Q_{set} - Q + D_Q (V_{ref} - V_g)] dt. \tag{2.11}$$

The logic to calculate the voltage droop coefficient $D_Q$ is equivalent to calculating $D_p$. It is defined as the ratio between change in reactive power and change in voltage, i.e:

$$D_Q = -\frac{\Delta Q}{\Delta V}. \tag{2.12}$$

And K, similarly to J, can be tuned through the voltage-droop loop time constant $\tau_v = K/\omega_n D_Q$ by assuming that $\mathbf{v}_g \approx \mathbf{e}$, hence $V_g \approx E$.

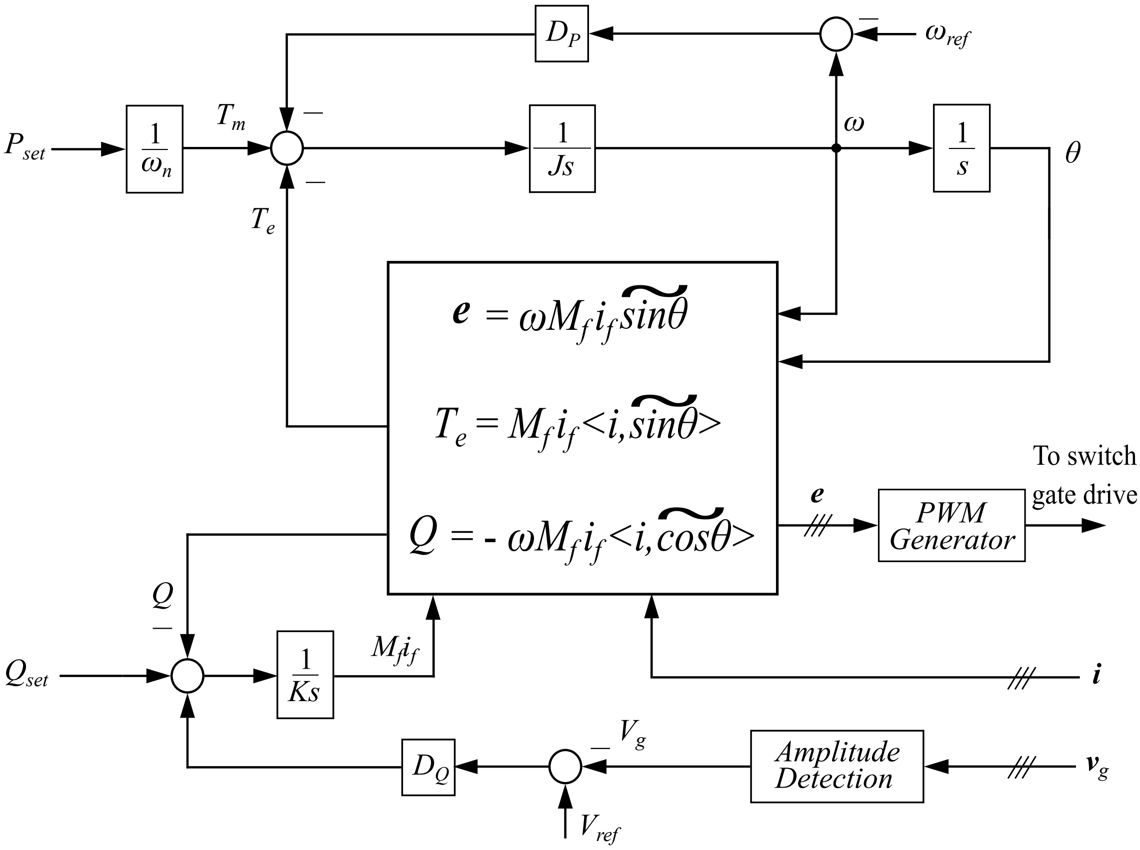

Figure 2.4: Synchronverter control block diagram [2].

The synchronverter control benefits from years of experience in modeling of synchronous machines for all types of analysis. Small-signal modeling for stability studies can be found in [42], which also proposes the use of virtual resistance to improve stability and efficiency. A modified virtual flux control loop is proposed in [43] to improve the synchronverter dynamic response, while [44] seeks more resemblance to a real synchronous machine with its model, including response for 3-phase faults and severe voltage sags. Especially for the synchronous machine emulation controls mentioned in this chapter, [45] explores the synchronous frequency resonance effect that may cause power oscillations and power angle instabilities due to the fast acting flux dynamics in inverters driven by these controls. The synchronous machine model that will be used in this thesis has the same constraints and assumptions of [2], but will be defined from a space-vector generic AC machine model developed in [36], which will result in a model in the stationary $\alpha\beta$ reference frame. From a control design point of view, the synchronverter is a non-linear MIMO system, which is not trivial to tune for exact dynamic response. In [46], the authors give some helpful insight about the influence of internal and grid parameters on the synchronverter's performance and stability that can aid in the tuning process, however, only [35], [47] and [48] provided actual tools to achieve it. The first is an HVDC transmission system based on synchronverter control, aiming to improve stability of the system itself and the neighboring AC areas connected to each end, which was achieved by employing a coordinated tuning technique based on pole placement of the system modes. The last two works presented parameter tuning solutions through small-signal analysis of the synchronverter model, although the former is for a heavily modified version of it. In this thesis, an approach similar to the one found in [47] will be used to tune the S-STATCOM parameters due to its compromise between simplicity and accuracy.

Besides the ones already mentioned, applications of the synchronverter strategy range from grid-friendly PV and wind power systems [49][50] to damping of inter-area power oscillations [51]. And since it is able to control the active and reactive powers independently, it can be used to implement the control of a STATCOM, i.e., a synchronous machine equivalent operating as a synchronous condenser, when $P_{set} = 0$. Using this premise, the standard synchronverter presented in this section will be used as baseline to develop the S-STATCOM control. Few publications and works were found on this subject and some will be addressed in the next section.

## 2.2 Non-generating Synchronverters

The term "non-generating synchronverter" was first used in [5] to define applications of the synchronverter strategy that do not focus on active power generation. This is not a new concept for VSM strategy, as can be seen in [52], [53] and [54] where the authors design and analyze a VSM-based STATCOM.

However, for synchronverter control, the first work of the kind was published in 2012 by Nguyen *et al* [3], presenting a synchronverter-based STATCOM control shown in Figure 2.5. It still calculates the back-EMF and reactive power through equations 2.3 and 2.4, but it eliminates electrical torque calculation. Instead, the active power loop is entirely modified to associate the phase angle of $\mathbf{e}$ to the DC bus capacitor voltage. The PI controller generates a signal based on the DC bus voltage difference to be compared to the angular speed reference, resulting in the synchronverter speed tracking the grid. This speed is utilized to the calculation of system equations and into the integrator to generate the back-EMF phase angle, regulating the active power to maintain the DC bus voltage. The PI controller generating the phase angle is meant to speed up the process.

Another change compared to the original synchronverter [2] is the decoupling of reactive power and voltage loops, allowing independent regulation of reactive power output or voltage at the PCC by activating switches $S_Q$ or $S_V$, respectively. When both switches are activated, the voltage-droop functionality for reactive power sharing is enabled. This structure is used in the proposed control and will be better explained in chapter 4.

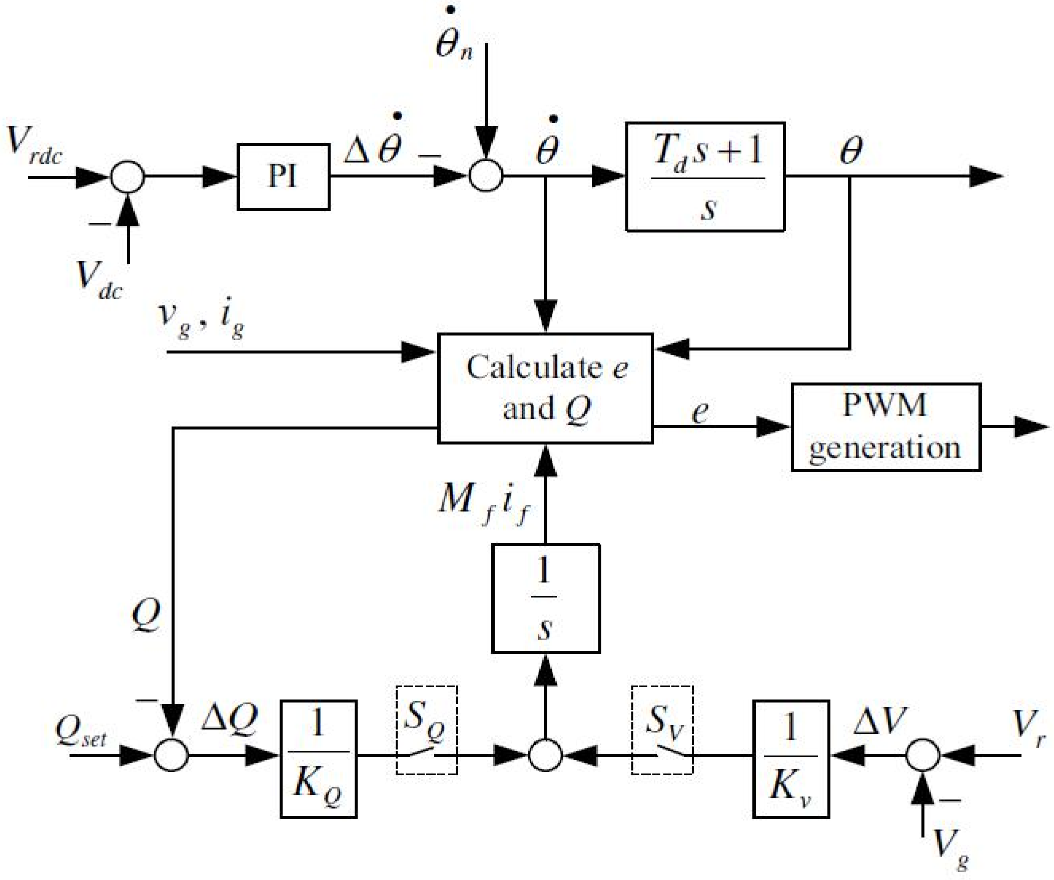

Figure 2.5: Synchronverter-based STATCOM from Nguyen *et al* [3]

In 2015, a paper was published by Emmerik *et al* [4] entitled “A Synchronverter to Damp Electromechanical Oscillations in Brazilian Power Grid”. It modifies the original synchronverter structure shown in Figure 2.6 to substitute the shunt connected Static VAR Compensator (SVC) in Bom Jesus da Lapa bus that currently performs this task. When combined with a regular Power System Stabilizer (PSS), it showed great performance in damping the typical oscillations that appeared after a perturbation was applied to the system. Only difference between this structure and the original is the lack of frequency droop coefficient, since it did not have an energy storage to exchange active power with the grid.

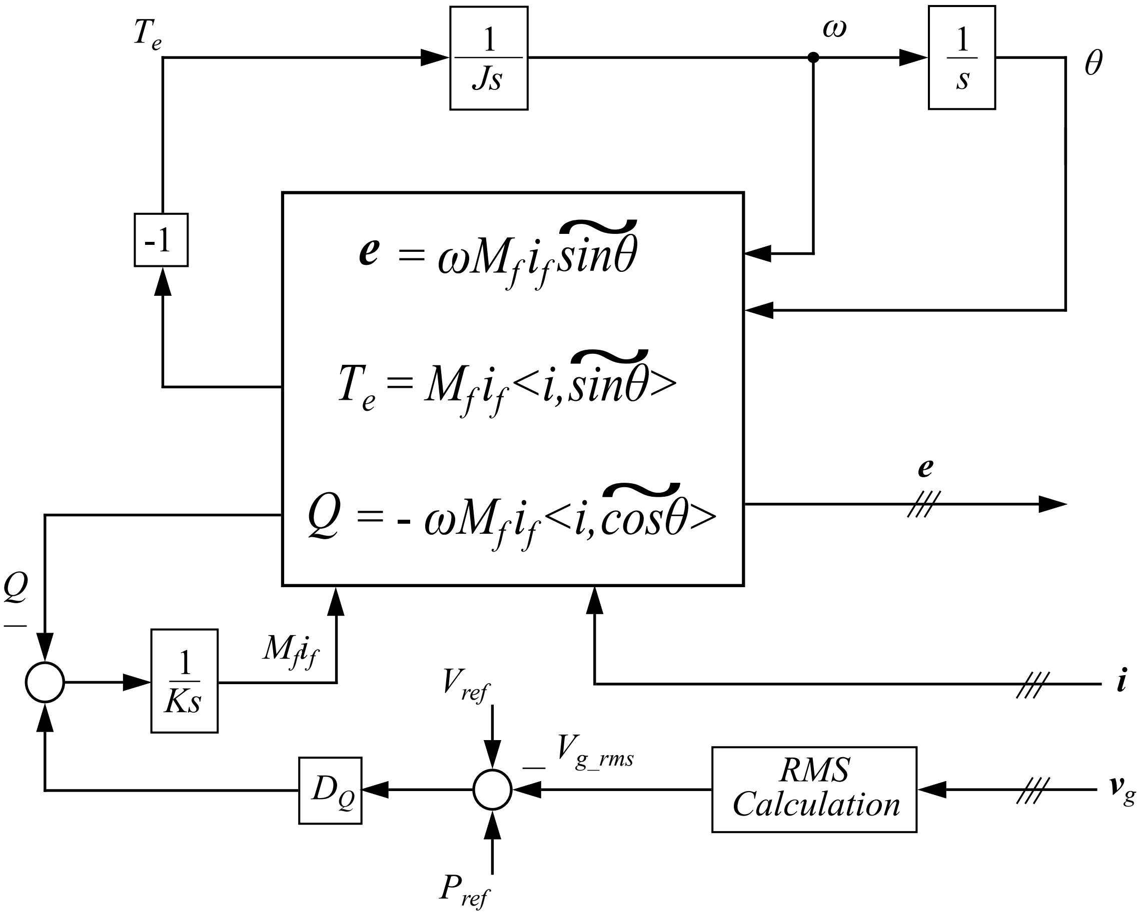

Figure 2.6: Non-generating synchronverter used in [4]

Later in 2018, Emmerik's PhD thesis [5] expanded on this concept. Firstly, a proportional gain was added in parallel with the virtual inertia integrator and a circuit equivalent to a PLL is found, allowing the use of a vast collection of techniques developed by the scientific community in tuning this type of circuit. Secondly, a small-signal model and tuning methodology was developed to damp synchronous frequency resonance (SFR) effects [45] that may occur when converters using virtual inertia emulation are connected to high $X/R$ grids. Also, thorough comparison was made between Emmerik's system and the one proposed in [3] and a noticeable shortcoming was found on the latter. By limiting the active power loop to one PI controller associating the change in DC bus voltage to the power angle, it was harder for the system in [3] (Figure 2.5) to achieve compromise between damping SFR effects that could lead to instability and keeping DC bus voltage oscillations withing acceptable levels. The improved synchronverter structure from [5] (Figure 2.7) demonstrated to be more flexible in this sense, therefore more suitable for connection in bulk transmission systems.

The control structures presented in this section contributed to grid power quality in the sense of providing voltage regulation at the PCC and frequency stability through inertial contribution. In the next section, some applications of synchronverter control focused on performance under unbalanced conditions or in grids with high harmonic content are presented.

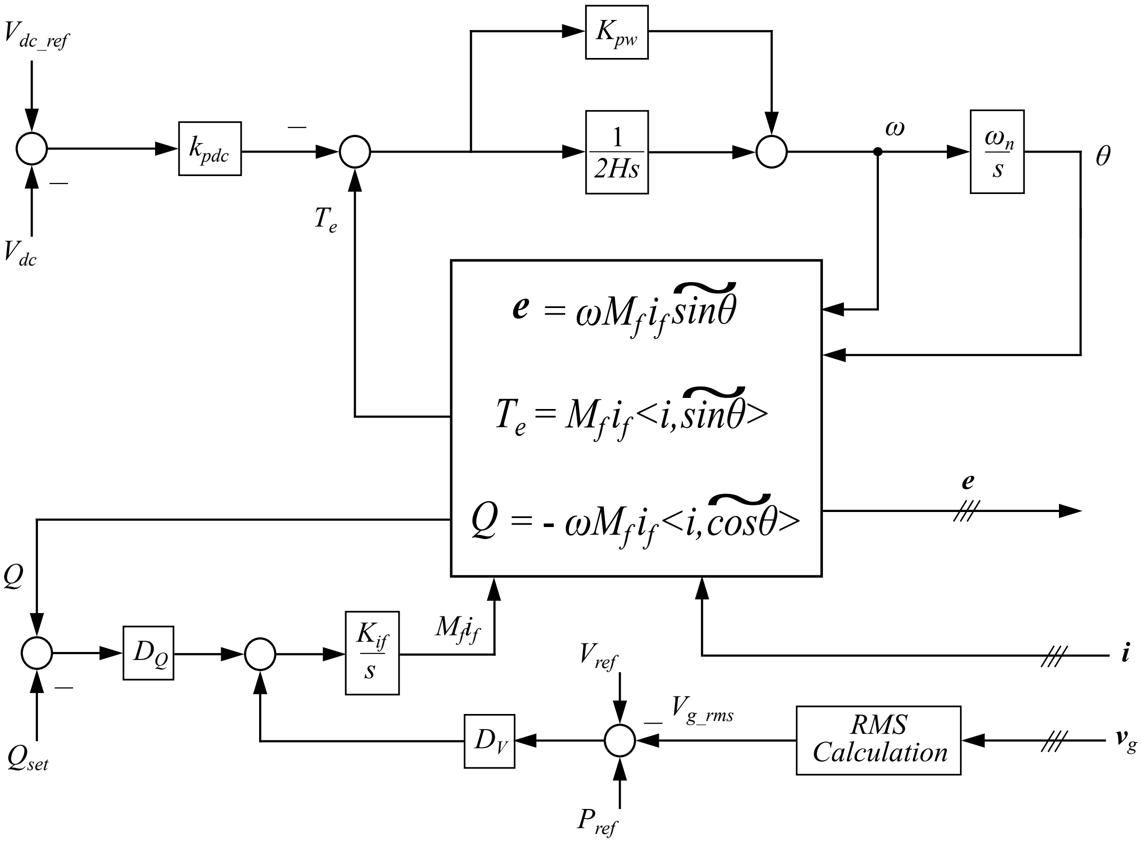

Figure 2.7: Improved non-gerenerating synchronverter from [5].

## 2.3 Power Quality Applications

At distribution level and microgrids, the increasing penetration of converter connected generators and loads makes power quality concerns an ever growing issue. Voltage regulation, imbalance, frequency stability and harmonic content are among the challenges scientists and engineers have to tackle to provide customers with reliable sources of electrical energy.

Concerning the synchronverter concept role on those issues, strategies presented in the previous sections already address voltage regulation and frequency stability, but do not perform analysis under unbalanced voltage conditions or grids with high harmonic contents. Two papers were found addressing such issues and will be presented here in this section.

The first is from Conrado *et al* [6], which aims to compensate voltage harmonics at the PCC. Figure 2.8 shows the control structure. It uses instantaneous power theory [55] to separate the harmonic content from the measured PCC currents and pass them through Proportional-Resonant (PR) controllers [56]. Their output is a voltage signal to be added to the back-EMF voltage generated by the main synchronverter control. The resonant component of the PR controller is actually the sum of several resonant components, each tuned to a specific harmonic frequency, allowing compensation of each one without interfering with the main controller. This is possible because of the PR controller characteristic of providing high gain at the resonance frequency and high attenuation out of it.

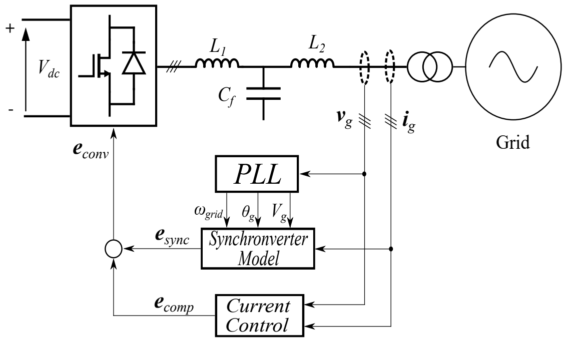

(a)

$$G_c(s) = k_p + \sum_{h=5,7,11} \frac{2k_I \xi \omega s}{s^2 + 2k_I \xi \omega s + \omega^2}$$

(b)

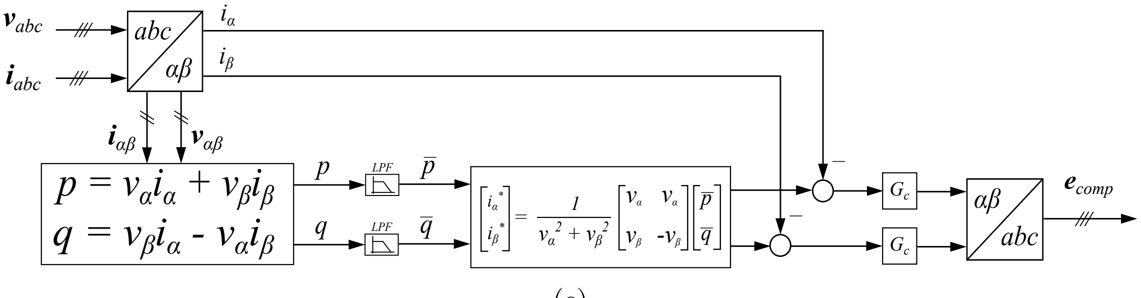

(c)

Figure 2.8: Synchronverter based control to compensate grid harmonics by Conrado *et al*[6]. (a) One-line diagram of the system showing control blocks; (c) Multi-frequency tuned PR controller transfer function; (b) Current controller for harmonic compensation.

The second paper is from Caicedo *et al* [7]. Its main objective is to study the synchronverter performance when connecting wind and PV generation to a weak grid with nonlinear and unbalanced loads. It was found through simulations that the synchronverter power output was compromised by harmonics in the PCC voltage, therefore, a resonant harmonic compensator was proposed to fix this issue. Fig 2.9 shows the control structure.

Both the pure resonant and the PR compensator from [6] share characteristics of modularity and lack of cross coupling when used with signals in stationary reference frame. Several controllers can be tuned to different resonant frequencies and their outputs can be added without significant influence on each other and the main control. This was a motivating factor in this thesis to use a synchronverter model in the stationary reference frame as in [7] and PR controllers for the voltage unbalance

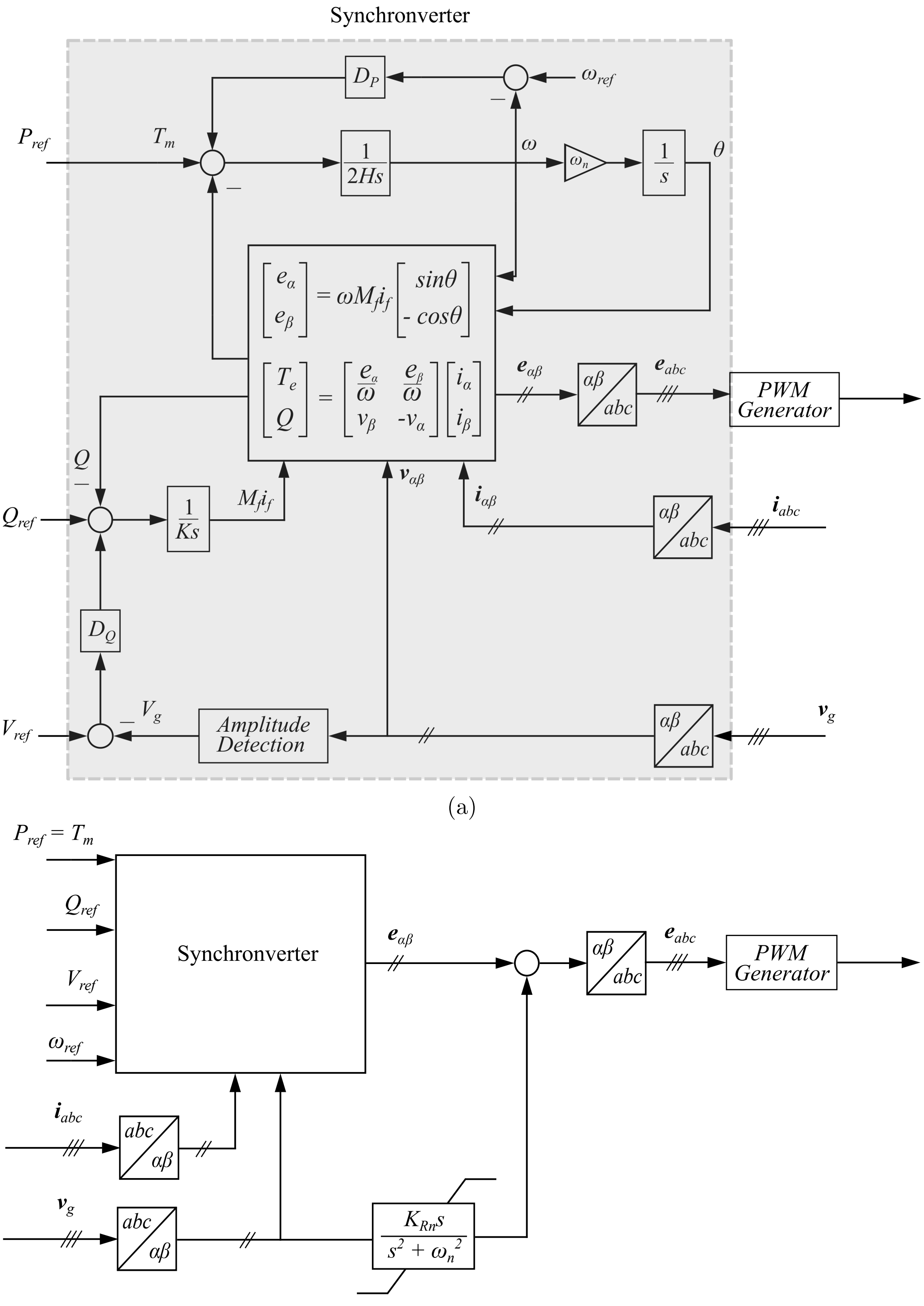

Figure 2.9: Synchronverter with resonant harmonic compensator proposed in [7]. (a) Detailed synchronverter control structure; (b) Synchronverter with resonant harmonic compensator

compensation functionalities.

## 2.4 Partial conclusions

Emulation of a synchronous machine as a control strategy for grid connected inverters is a growing trend. The VSG and Synchronverter are the most popular approaches to integrate renewable energy sources to the grid, due to its intrinsic inertial response feature that can mitigate energy availability and intermittence issues when properly designed and tuned. Both approaches have structural differences between them. The VSG based control strategies use only the frequency droop equations from a synchronous machine model and rely on accurate power measurements from the PCC, while the Synchronverter strategies use a more complete synchronous machine model, which calculates active and reactive power through the back-EMF generated by the rotor magnetic flux loop. Such characteristics make the VSG approach easier to design and implement, while the Synchronverter ones share a closer resemblance with real synchronous machines, which raises the question of which one is more grid-friendly regarding the existing hierarchical controls from the point of view of the power system operator.

As a consequence, the Synchronverter based control strategies are less researched then the VSG ones, which leaves room for improvement in design, tuning, implementation and applications. In this section, some of those topics were presented with focus on synchronverter power quality applications, on which only a few works addressed at the time of publication of this thesis.

Nevertheless, their contributions were significant and showed several synchronverter based controls, ranging from operation as an SVC to damp power system oscillations to operation as a STATCOM or active filter, providing reactive power, voltage support and harmonic compensation. To the author's knowledge, voltage imbalance compensation by a synchronverter based control strategy is a topic lacking research effort, which motivated the development of this work.

# Chapter 3

# Synchronous Generator model in the $\alpha\beta$ reference frame

In this chapter, a synchronous generator model is derived from the generalized symmetric AC machine model presented in [36], which is in space vector representation. The result is a synchronverter model in the stationary reference frame with a modified reactive power calculation.

## 3.1 General symmetric AC machine model in space vector representation

One of the applications of mathematical modeling by a vector representation of an AC Machine is for speed driving control, more precisely using the vector control throughout a power electronic converter, named as VSD (variable speed drive). Modeling of AC machines in this way incorporates most of its qualitative features for control purposes, with the benefit of not restricting its voltages and currents to be sinusoidal and balanced [36]. The synchronous generator (SG) model that will be used in this thesis will be derived from the general AC machine model developed in [36], which will be briefly explained here. For details on its development, see [36].

The general AC machine model is developed with the following considerations: it is a three-phase, two pole motor with round rotor, resulting in an uniform air gap between rotor and stator; all phases are symmetrically distributed along the rotor and stator volume; permeability of stator and rotor iron are assumed to be infinite; saturation and iron losses are ignored. To represent the machines' quantities in vector form, complex reference frames for stator and rotor are defined, which are perpendicular to the line that crosses the stator and rotor central turns, respectively, as shown in Figure 3.1. Angle $\theta(t) = \omega t$ represents the rotor position measured from the stator coordinates.

Secondly, stator and rotor flux linkages are defined in space vector representation as follows:

$$\underline{\mathbf{\Phi}}_S(t) = L_S\underline{\mathbf{i}}_S(t) + M_f[\underline{\mathbf{i}}_R(t)e^{j\theta(t)}], \tag{3.1}$$

$$\underline{\mathbf{\Phi}}_R(t) = L_R\underline{\mathbf{i}}_R(t) + M_f[\underline{\mathbf{i}}_S(t)e^{-j\theta(t)}]. \tag{3.2}$$

$L_S$, $L_R$, $R_S$ and $R_R$ are the self inductances and resistances of stator and rotor windings, respectively. $M_f$ is the maximum mutual inductance between stator and rotor windings. It should be noted that the flux linkage is a real value, as it represents a physical quantity. The complex flux vector represents the amplitude and angular position of the peak flux density in the air gap. Subscript S denotes that the quantities are related to the stator windings and also referenced to stator coordinates, while subscript R denotes that they are related to the rotor windings and referenced to rotor coordinates. Therefore, the term $e^{\pm j\theta(t)}$ indicates that the current vector $\mathbf{i}_R$ is rotated to the stator or rotor coordinates before its influence on the flux linkages can be calculated.

Next, stator and rotor phase voltages are calculated and presented in space vector form:

$$\underline{\mathbf{v}}_S(t) = R_S\underline{\mathbf{i}}_S + \frac{d\underline{\mathbf{\Phi}}_S}{dt}, \tag{3.3}$$

$$\underline{\mathbf{v}}_R(t) = R_R\underline{\mathbf{i}}_R + \frac{d\underline{\mathbf{\Phi}}_R}{dt}. \tag{3.4}$$

By substituting (3.1) and (3.2) in (3.3) and (3.4), they can be rewritten as:

$$\underline{\mathbf{v}}_S(t) = R_S\underline{\mathbf{i}}_S + L_S\frac{d\underline{\mathbf{i}}_S}{dt} + M_f\frac{d}{dt}[\underline{\mathbf{i}}_R e^{j\theta}], \tag{3.5}$$

$$\underline{\mathbf{v}}_R(t) = R_R\underline{\mathbf{i}}_R + L_R\frac{d\underline{\mathbf{i}}_R}{dt} + M_f\frac{d}{dt}[\underline{\mathbf{i}}_S e^{-j\theta}]. \tag{3.6}$$

As for the mechanical part, electrical torque is defined as

$$T_e(t) = \frac{2}{3}M_f\Im[\underline{\mathbf{i}}_S(\underline{\mathbf{i}}_R e^{j\theta})^*], \tag{3.7}$$

where the imaginary part is proportional to the cross product of the stator and rotor current vectors [36]. The swing equation is then given as

$$J\frac{d\omega}{dt} = T_e(t) - T_m(t) = \frac{2}{3}M_f\Im[\underline{\mathbf{i}}_S(\underline{\mathbf{i}}_R e^{j\theta})^*] - T_m(\theta,\omega,t). \tag{3.8}$$

Thus completing the general symmetric AC machine model, represented by the equations below:

$$\underline{\mathbf{v}}_S = R_S\underline{\mathbf{i}}_S + L_S\frac{d\underline{\mathbf{i}}_S}{dt} + M_f\frac{d}{dt}[\underline{\mathbf{i}}_R(t) e^{j\theta}], \tag{3.9}$$

$$\underline{\mathbf{v}}_R = R_R\underline{\mathbf{i}}_R + L_R\frac{d\underline{\mathbf{i}}_R}{dt} + M_f\frac{d}{dt}[\underline{\mathbf{i}}_S e^{-j\theta}], \tag{3.10}$$

$$J\frac{d\omega}{dt} = \frac{2}{3}M_f\Im[\underline{\mathbf{i}}_S(\underline{\mathbf{i}}_R e^{j\theta})^*] - T_m(\theta,\omega,t), \tag{3.11}$$

$$\frac{d\theta}{dt} = \omega. \tag{3.12}$$

Equations (3.9) and (3.10) can each be split into real and imaginary parts, resulting in a set of 6 scalar differential equations. They are valid for any current and voltage waveforms without zero sequence components, at varying load torque and speed. This model can be adjusted and simplified to analyze several non salient machines, as long as the initial assumptions remain valid.

## 3.2 Synchronous generator model

The synchronous generator model used in this thesis is derived from the generalized symmetrical AC machine model presented in [36]. Equations (3.9) through (3.12), which define the generalized model in space vector representation, are repeated below in per unit and generator convention. Subscript S denotes that the quantities are related to the stator windings and also referenced to stator coordinates, while subscript R denotes that they are related to the rotor windings and referenced to rotor coordinates, which are depicted in Figure 3.1.

$$\underline{\mathbf{v}}_S = -R_S\underline{\mathbf{i}}_S - L_S\frac{d\underline{\mathbf{i}}_S}{dt} - M_f\frac{d}{dt}[\underline{\mathbf{i}}_R e^{j\theta}], \tag{3.13}$$

$$\underline{\mathbf{v}}_R = -R_R\underline{\mathbf{i}}_R - L_R\frac{d\underline{\mathbf{i}}_R}{dt} - M_f\frac{d}{dt}[\underline{\mathbf{i}}_S e^{-j\theta}], \tag{3.14}$$

$$2H\frac{d\omega}{dt} = T_m(t) - T_e(t) = T_m(\theta,\omega,t) - \frac{2}{3}M_f\Im[\underline{\mathbf{i}}_S(\underline{\mathbf{i}}_R e^{j\theta})^*], \tag{3.15}$$

$$\frac{d\theta}{dt} = \omega\omega_n. \tag{3.16}$$

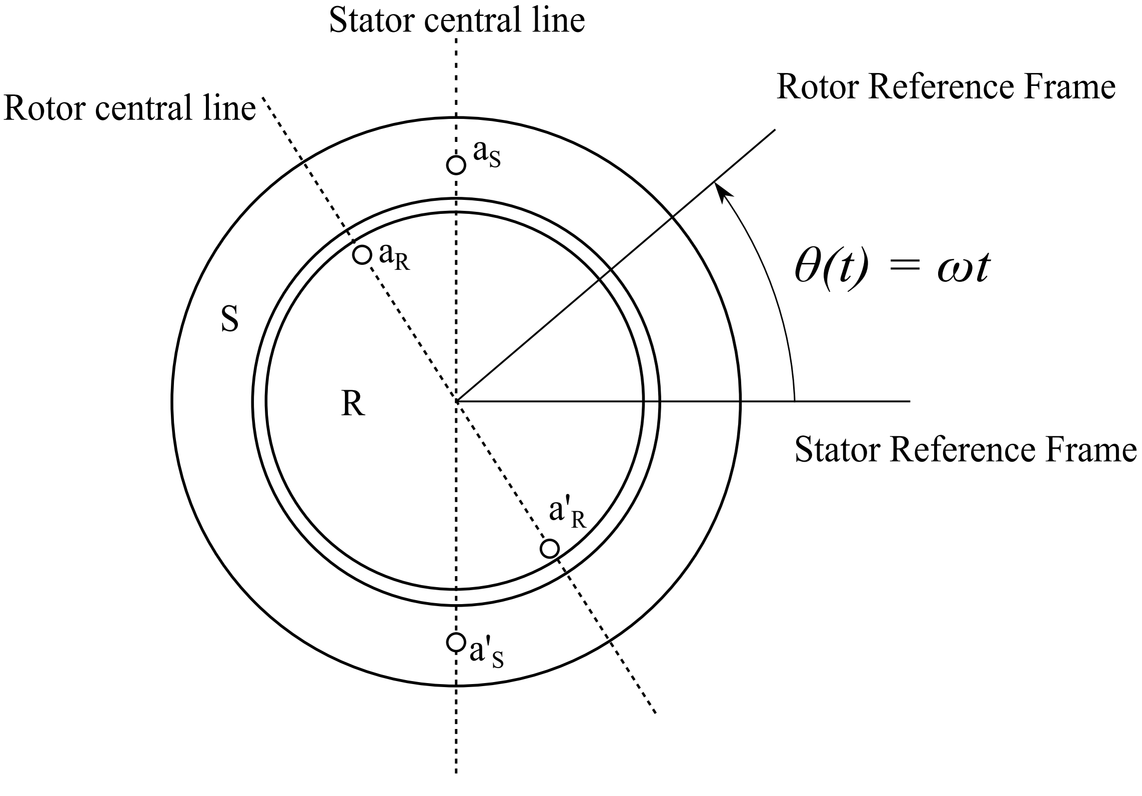

Figure 3.1: Symmetrical AC machine

By applying the conditions defined in [2] and presented in Section 2.1 for the synchronous generator model used in the original synchronverter, equation (3.14) describing rotor dynamics can be ignored, since the rotor current is considered a constant adjustable parameter. This constraint is similar to a permanent magnet synchronous machine, which is represented in [36] by a rotor circuit of the generalized model being fed by two constant DC current sources of magnitude $I_F/2$, as shown in Figure 3.2b. By considering the aforementioned constraint, an adaptation to the rotor circuit in Figure 3.2a is made to better represent this model's virtual rotor and it is shown in Figure 3.2b. The rotor current vector for this case is:

$$\underline{\mathbf{i}}_R = i_f - \frac{i_f}{2}e^{j2\pi/3} - \frac{i_f}{2}e^{j4\pi/3} = \frac{3}{2}i_f. \tag{3.17}$$

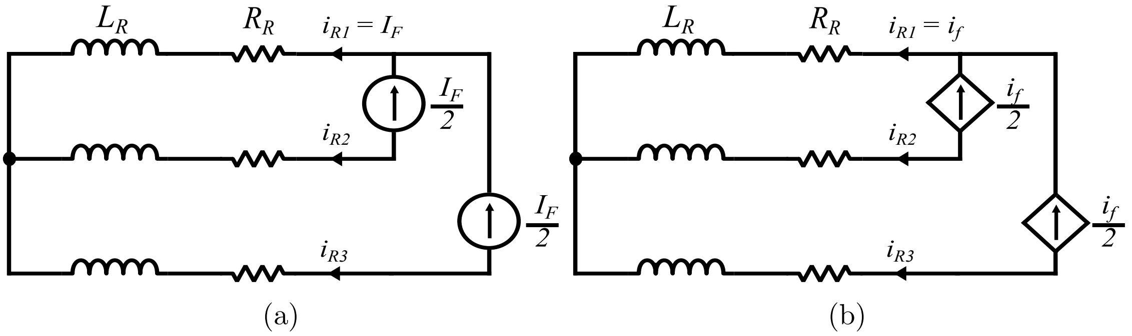

Figure 3.2: a) Equivalent rotor circuit for a Permanent Magnet Synchronous Motor; b) Adapted virtual rotor circuit for the synchronous generator model.

By substituting (3.17) in (3.13) and evaluating its last derivative, it leads to:

$$\underline{\mathbf{v}}_S = -R_S\underline{\mathbf{i}}_S - L_S\frac{d\underline{\mathbf{i}}_S}{dt} - j\omega\frac{3}{2}M_f i_f e^{j\theta}, \tag{3.18}$$

where the back-EMF or internal voltage $\underline{\mathbf{e}}$ is readily identifiable as the term $-j\frac{3}{2}\omega M_f i_f e^{j\theta}$ in space vector representation, and can be rewritten as

$$\begin{aligned}\underline{\mathbf{e}} &= -j\frac{3}{2}\omega M_f i_f e^{j\theta} \\ &= -j\frac{3}{2}\omega M_f i_f[\cos(\theta) + j\sin(\theta)] \\ &= \frac{3}{2}\omega M_f i_f[\sin(\theta) - j\cos(\theta)].\end{aligned} \tag{3.19}$$

Notice that (3.18) can be represented in stationary $\alpha\beta$ reference frame by Clarke's amplitude invariant transformation without any simplifications by applying the following relationship (see Appendix):

$$\underline{\mathbf{v}}_S = \frac{3}{2}\mathbf{v}_s, \tag{3.20}$$

where $\mathbf{v}_s$ is the complex vector composed of Clarke's amplitude invariant $\alpha$ and $\beta$ components. Complex vectors in this form will be represented in this section with the lowercase index of its equivalent space vector and no underline. Applying this logic to (3.18), it can be rewritten as:

$$\begin{aligned}\frac{3}{2}\mathbf{v}_s &= -\frac{3}{2}R_S\mathbf{i}_s - \frac{3}{2}L_S\frac{d\mathbf{i}_s}{dt} + \frac{3}{2}\omega M_f i_f[\sin(\theta) - j\cos(\theta)]\\ \mathbf{v}_s &= -R_S\mathbf{i}_s - L_S\frac{d\mathbf{i}_s}{dt} + e_\alpha + je_\beta \\ \mathbf{v}_s &= -R_S\mathbf{i}_s - L_S\frac{d\mathbf{i}_s}{dt} + \mathbf{e}.\end{aligned} \tag{3.21}$$

where $\mathbf{v}_s$, $\mathbf{i}_s$ and $\mathbf{e}$ are the Clarke's amplitude invariant complex vectors representing the virtual stator terminal voltage, current and back-EMF space vectors, respectively. Notice that the 3/2 factor cancels out, which means that the amplitude of those quantities in Clarke's amplitude invariant representation can be considered equal to the amplitude of their space vector representation. Therefore, power calculated at the machine terminals will represent the actual three-phase power as if they were calculated with quantities in the Clarke's power invariant representation. Evaluation of the electrical torque equation yields:

$$\begin{aligned}T_e(t) &= M_f i_f \Im[-\underline{\mathbf{i}}_S e^{-j\theta}]\\ &= \frac{3}{2}M_f i_f[i_{s\alpha}\sin(\theta) - i_{s\beta}\cos(\theta)],\\ &= \frac{e_\alpha i_{s\alpha}}{\omega} + \frac{e_\beta i_{s\beta}}{\omega}\end{aligned} \tag{3.22}$$

where $e_\alpha$, $e_\beta$, $i_{s\alpha}$, $i_{s\beta}$ are Clarke's amplitude invariant complex vector components that represent the back-EMF and virtual stator current space vectors, respectively. Since reactive power calculation is not embedded in the generalized AC machine model, it must be included in another way. An intuitive approach is to calculate it through the instantaneous power theory [55], which would lead to

$$q = e_\beta i_{s\alpha} - e_\alpha i_{s\beta}. \tag{3.23}$$

However, this would need a 3/2 scaling factor because both back-EMF and current stationary frame components are representing $\underline{\mathbf{e}}$ and $\underline{\mathbf{i}}_S$ space vectors (see Appendix). Besides, this approach considers reactive power calculation at the inverter terminals, which is not interesting in practice because of the voltage drop across the filter inductances and eventual coupling transformer would cause a significant difference between reactive power measured at the PCC. In comparison to a real SG, the voltage drop across the stator leakage reactance is significant since typical values may range from 10 to 20% in the generator's base power [40]. This also implies in significant difference in reactive power output calculated before and after the stator impedance. On the other hand, active power output is often considered the same (disregarding mechanical losses) when calculated before and after stator impedance, since the armature resistance is small enough to be neglected. The same happens for a synchronverter or VSG, maybe even worse concerning reactive power output difference between converter terminals and PCC due to the filter and coupling transformer impedances.

Therefore, calculation of reactive power $q$ is defined at the virtual stator terminals in a similar way to the instantaneous power theory [55], yielding

$$q = v_{s\beta} i_{s\alpha} - v_{s\alpha} i_{s\beta}, \tag{3.24}$$

where $v_{s\alpha} = V_s \cos(\theta_s)$ and $v_{s\beta} = V_s \sin(\theta_s)$ are the amplitude invariant, stationary reference frame components of $\mathbf{v}_s$. $V_s$ and $\theta_s$ are the virtual stator voltage amplitude and phase, respectively.

Finally, the damping coefficient $D_p$ is added to (3.15) representing the combined effect of mechanical friction losses and frequency drooping as in [2], thus completing the synchronous generator model in the stationary $\alpha\beta$ frame to be used in the S-STATCOM. Space vector equations of the model are repeated below and Figure 3.3 shows its block diagram of implementation without the controls. As in the conventional synchronverter, the control inputs are the virtual mechanical torque $T_m$ and virtual rotor magnetic flux $M_f i_f$.

$$\mathbf{v}_s(t) = -R_S \mathbf{i}_s - L_S \frac{d\mathbf{i}_s}{dt} + \mathbf{e}, \tag{3.25}$$

$$2H \frac{d\omega}{dt} = T_m(t) - T_e(t) - D_p(\omega - \omega^*), \tag{3.26}$$

$$\frac{d\theta}{dt} = \omega \omega_n. \tag{3.27}$$

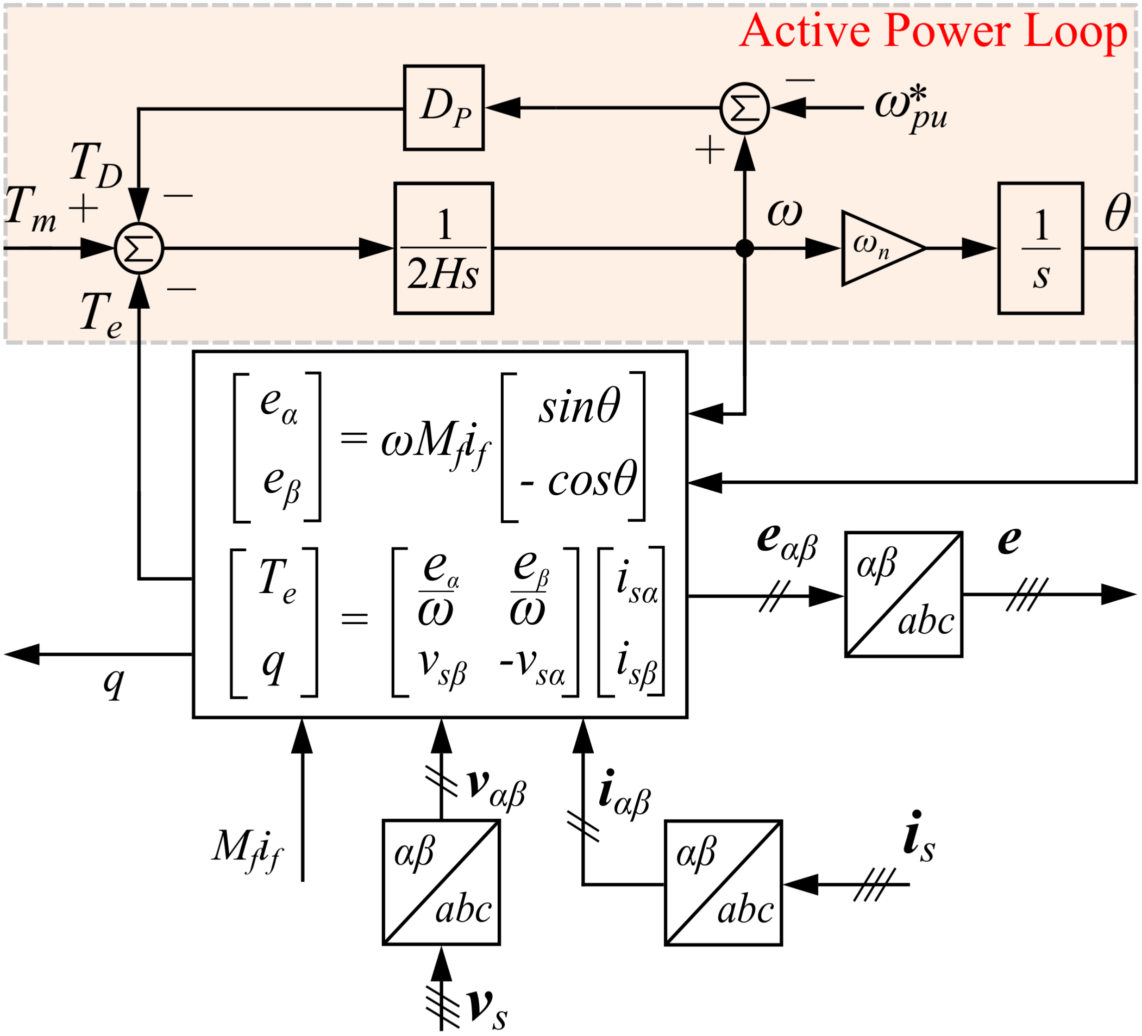

Figure 3.3: Synchronous generator in the stationary frame

# Chapter 4

# S-STATCOM Proposed Control Scheme

The S-STATCOM complete model is defined in this chapter. Details of its operation and control design are addressed. Building process of both simulations and prototype are also discussed.

In this chapter, the first section presents a quick overview of control strategies for grid connected converters to deal with voltage imbalance. The second section develops the complete model of the S-STATCOM and explains each of its 5 modes in detail: self-synchronization with the grid, reactive power exchange, PCC voltage regulation, reactive power/voltage drooping and the voltage imbalance compensation. The third section focuses on the creation of a small-signal model and derivation of its transfer functions, with the purpose of establishing design criteria for the DC bus voltage controller that achieves the best compromise between system stability and dynamics.

## 4.1 Control Strategies to Mitigate Voltage Imbalance

Balanced electrical power systems deliver energy through sets of three phase voltages that are sinusoidal, equal in magnitude and phases $120^o$ apart from each other. However, under abnormal operating conditions or certain grid characteristics, they might become unbalanced, i.e, present different magnitude and/or phase displacement from each other at the fundamental frequency.

For three-phase systems, this asymmetry is studied through the symmetrical components theory, which consists of transforming an unbalanced set of three-phase phasors into two sets of balanced three phase phasors and one set of three phase phasors with equal magnitudes and phase angles, called sequence components: positive, negative and zero, respectively. This is achieved by applying the Fortescue transform:

$$\begin{bmatrix} \mathbf{V^0} \\ \mathbf{V}^+ \\ \mathbf{V}^- \end{bmatrix} = [\mathbf{A}]^{-1} \begin{bmatrix} \mathbf{V_a} \\ \mathbf{V_b} \\ \mathbf{V_c} \end{bmatrix}, \tag{4.1}$$

where the $\mathbf{A}$ matrix is

$$\mathbf{A} = \begin{bmatrix} 1 & 1 & 1 \\ 1 & \mathbf{a}^2 & \mathbf{a} \\ 1 & \mathbf{a} & \mathbf{a}^2 \end{bmatrix}, \tag{4.2}$$

with $\mathbf{a} = \frac{1}{2} + j\frac{\sqrt{3}}{2}$ being the Fortescue operator. Then, a voltage asymmetry index is quantified as being the ratio between its negative and positive sequence components. This is called the Voltage Unbalance Factor (VUF), a common asymmetry index used in European and international engineering standards, as well as in the brazilian Operational Procedures for Distribution Grids (PRODIST) [57]. It is usually presented as a percentage:

$$\%VUF = \frac{\mathbf{V}^{-}}{\mathbf{V}^{+}} \times 100. \tag{4.3}$$

The causes for voltage imbalances are numerous: untransposed transmission lines, unbalanced three-phase loads, uneven distribution of single-phase loads, etc [14][58], as well as their adverse effects to the loads and grid itself. For instance, it generates a reverse torque in motors causing unwanted vibrations and overheating. In PWM driven converters, it causes DC voltage oscillations and the appearance of non characteristic harmonics in the AC current, increasing THD, heating of components and overall loss of equipment lifespan.

Recently, with increased adoption of single-phase, converter connected DGs [59] and charging of electric vehicles (EVs) [60], the voltage imbalance problem is a growing power quality concern, especially for distribution and microgrids. Their higher equivalent impedances and lower X/R ratios makes them more sensitive to voltage related problems. Several solutions are available to balance distribution grids, usually involving just one device (UPQC [20], SVC [61], active filter [62] or STATCOM [63]) with sufficient power rating to mitigate the imbalance problem. This is possible because distribution grids may have more space and substations available to connect such devices . Micrograms on the other hand, may not have this advantage. Therefore, the research effort is focused on hierarchical control of the converter connected DGs to share the unbalance compensation effort [21][22][23].

Other types of control strategies for converter connected DGs are just to improve their performance under unbalanced conditions. In [8], a wide variety of control strategies, especially in the stationary reference frame, are proposed to increase control reliability of grid connected converters during adverse voltage conditions. For grid synchronization purposes, the DSOGI-FLL shown in Figure 4.1 is an adaptive filter coupled with a frequency locked loop (FLL) that provides robust grid frequency locking and, when combined with the Positive-Negative Sequence Calculator (PNSC) block, provides positive/negative sequence detection even when the grid voltage is polluted with harmonics. As for grid imbalance immunity, compensation and ride-through control strategies, the double synchronous reference frame (DSRF) current control loop shown in Figure 4.2 is the most popular due to its compatibility with PLL circuits.

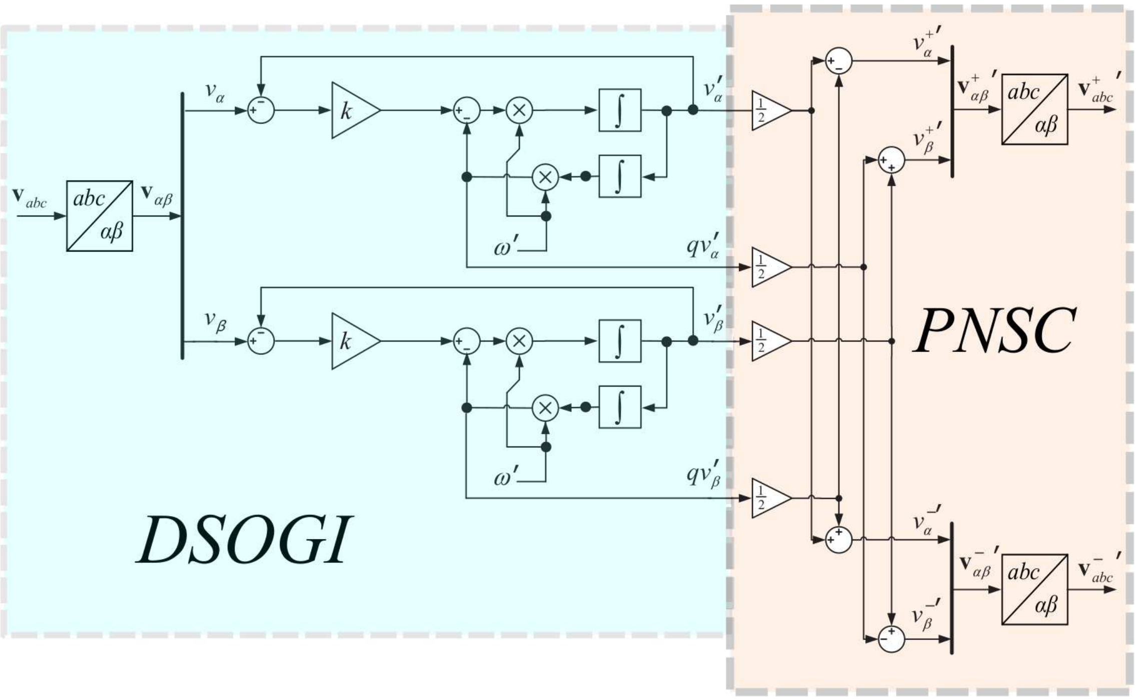

Figure 4.1: DSOGI+PNSC structure [8][9].

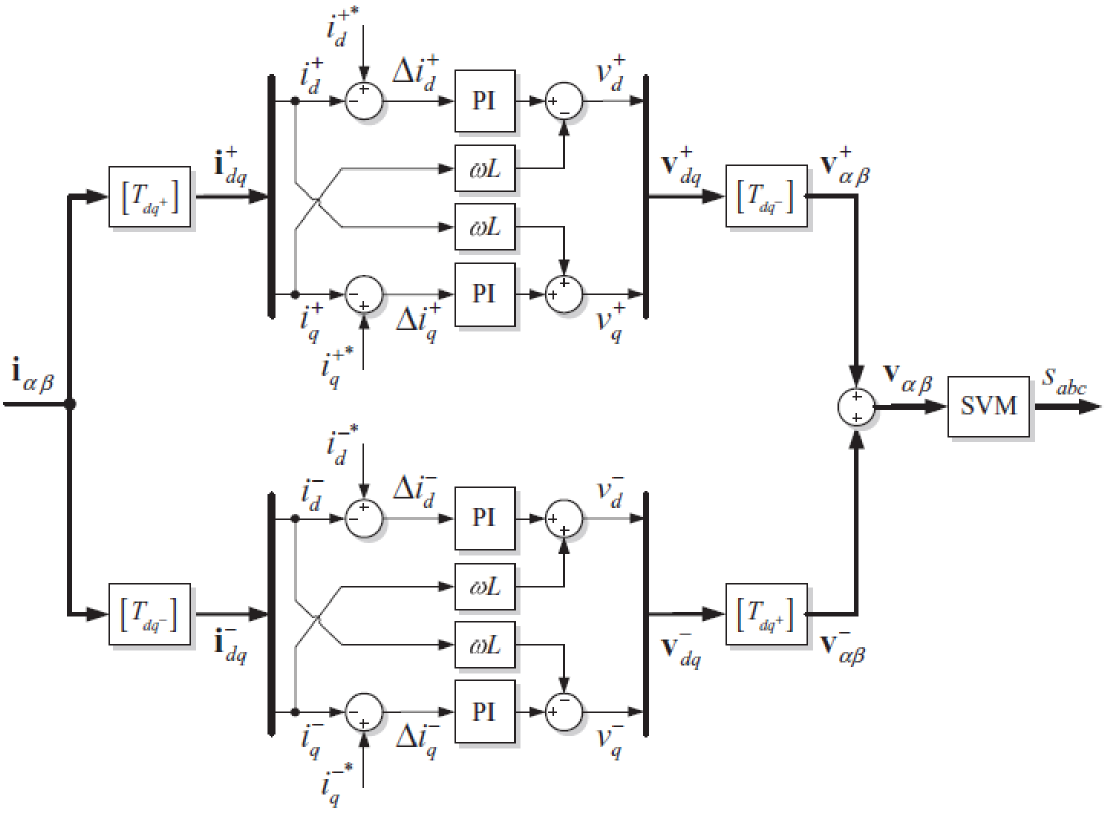

Figure 4.2: Double Synchronous Reference Frame Current Controller.

## 4.2 S-STATCOM Model

Creation of the S-STATCOM model is based on the previously defined SG model in space vector representation, shown in Figure 3.3. Its development in per unit notation and in stationary reference frame gives some advantages to the complete S-STATCOM model: 1) easier implementation of the equations; 2) lower computational burden for simulation tools and/or Digital Signal Processors (DSP) in charge of controlling an actual converter; 3) calculation of reactive power at the PCC using Clarke's amplitude invariant transformations without the need for 3/2 factor scaling; 4) increased compatibility with resonant controllers, which are the basis of the S-STATCOM voltage imbalance compensation capabilities.

Control loops are then added to the SG model in order to achieve the desired functionalities, which include self-synchronization with the grid, reactive power exchange and sharing, voltage regulation and imbalance compensation. Except for the latter, each feature was achieved with the following isolated work's contributions: 1) Synchronization algorithm proposed in [64] is employed to create clear and simple startup procedure, 2) A PI controller to regulate the DC bus capacitor voltage [65], 3) Decoupled reactive power exchange and PCC voltage regulation loops proposed in [3]. For the voltage imbalance compensation, a novel Voltage Imbalance Compensation Loop (VICL) is developed.

This completes the S-STATCOM model. Its structure is shown in Figure 4.3 with each Control Loop (CL) highlighted:

- CL 1a and 1b: both part of the Synchronization loop, responsible for achieving initial grid synchronization during the converter startup [64];
- CL 2: Active Power loop, responsible for maintaining grid synchronization by regulating the active power necessary to maintain the DC bus capacitor voltage at specified levels [65];
- CL 3: is the Decoupled Reactive Power and PCC Voltage Regulation loops [3];
- VICL is the Voltage Imbalance Control Loop, responsible for the compensation of voltage imbalance at the PCC.

Table 4.1 describes the possible modes of operation according to the switches' states. Switches $S_Q$ and $S_V$ allow three main modes of operation: direct control of reactive power (q-mode), PCC voltage regulation (V-mode) and reactive power sharing (Droop-Mode)[3]. Switches $S_P$ and $S_C$ are part of the initial synchronization algorithm, during the S-STATCOM startup. Switch $S_I$ enables voltage imbalance compensation (VIC), which works simultaneously with the main modes. Each control loop will be explained in detail, along with the modes associated with them in the following sections.

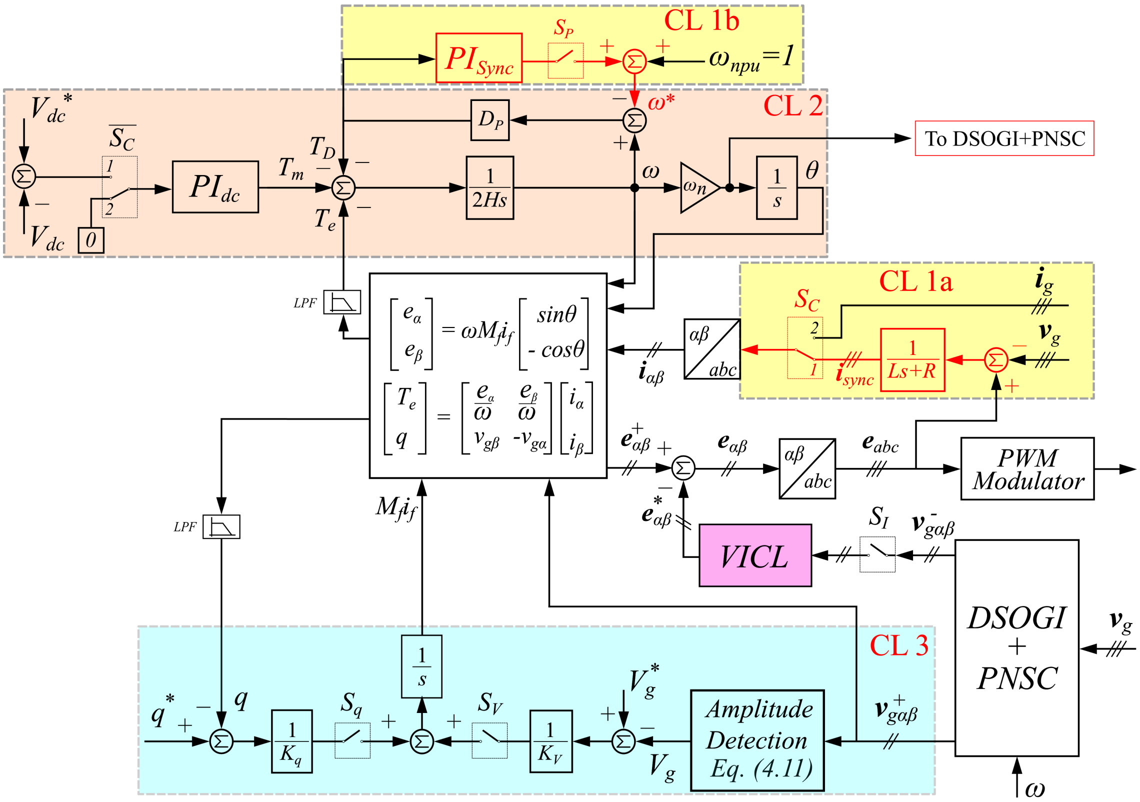

$$\begin{bmatrix} e_\alpha \\ e_\beta \end{bmatrix} = \omega M_f i_f \begin{bmatrix} \sin\theta \\ -\cos\theta \end{bmatrix}$$

$$\begin{bmatrix} T_e \\ q \end{bmatrix} = \begin{bmatrix} \frac{e_\alpha}{\omega} & \frac{e_\beta}{\omega} \\ v_{g\beta} & -v_{g\alpha} \end{bmatrix} \begin{bmatrix} i_\alpha \\ i_\beta \end{bmatrix}$$

Figure 4.3: Proposed S-STATCOM control strategy.

### 4.2.1 CL 1: Startup and Synchronization

The algorithm proposed in [64] is used for the initial S-STATCOM synchronization with the grid during its startup, being deactivated afterwards. It is represented by CL 1a and 1b in Figure 4.3. To understand how it works, consider the one-line diagram in Figure 4.4 showing a synchronverter connected to a grid represented by an infinite bus, which can also be extended to represent the S-STATCOM. The active and reactive power delivered by the synchronverter at the PCC is given by:

$$P = \frac{1}{Z_t}[EV_g \cos(\delta - \varphi) - V_g^2 \cos(\varphi)], \tag{4.4}$$

$$Q = \frac{1}{Z_t}[EV_g \sin(\varphi - \delta) - V_g^2 \sin(\varphi)], \tag{4.5}$$

where $E$ and $V_g$ are the internal and PCC voltage magnitudes in per unit, with $\theta$ and $\theta_g$ its respective phase angles. $Z_t$ and $\varphi$ are the transfer impedance in per unit and its angle, respectively. $\delta = \theta - \theta_g$ is the power angle of the synchronverter. If it is connected to a transmission line as in [5], then $\varphi \approx 90^o$ and the power equations

| Modes | | | | | | |
|---|---|---|---|---|---|---|
| $S_C$ | $\bar{S_C}$ | $S_P$ | $S_q$ | $S_V$ | $S_I$ | Description |
| 1 | 2 | ON | ON | OFF | OFF | Startup synchronization |
| 2 | 1 | OFF | ON | OFF | OFF | q-Mode |
| 2 | 1 | OFF | OFF | ON | OFF | V Mode |
| 2 | 1 | OFF | ON | ON | OFF | Voltage Droop Mode |
| 2 | 1 | OFF | ON | OFF | ON | q+VIC Mode |
| 2 | 1 | OFF | OFF | ON | ON | V+VIC Mode |
| 2 | 1 | OFF | ON | ON | ON | Voltage Droop+VIC Mode |

Table 4.1: S-STATCOM's Operation Modes.

can be simplified to

$$P = \frac{EV_g \sin(\delta)}{X_t}, \tag{4.6}$$

$$Q = \frac{EV_g \cos(\delta) - V_g^2}{X_t}, \tag{4.7}$$

where $X_t$ is the transfer reactance. Since the synchronverter has full control over its active and reactive power outputs, it can control them to be $P = Q = 0$. Such conditions imply that:

$$\begin{cases} E = V_g \\ \theta = \theta_g \end{cases}, \tag{4.8}$$

meaning that the synchronverter is fully synchronized with the grid. This is used in [64] to implement a synchronization procedure, which consists of creating a virtual current $i_{sync}$ from the difference $\mathbf{e}(t) - \mathbf{v}_g(t)$ by implementing a virtual impedance with $L >> R$, i.e., $\varphi \approx 90^o$. That current is fed to the synchronverter model equations and then to the power loops, which will converge to (4.8) and synchronize it with the grid. The $PI_{sync}$ controller in CL 1b is intended to speed up the process.

When the synchronization mode is activated on the S-STATCOM, $S_C$ is at position 1 allowing the virtual synchronizing current $i_{sync}$ to flow into the control and initialize the process. The DC bus voltage PI controller is disabled through $\bar{S_C}$ to satisfy the condition of $P = 0$. Switches $S_P$ and $S_q$ are on to enable $PI_{sync}$ and to force $q = 0$, respectively. During this mode, converter switching is disabled and only the control signals are being processed, to avoid high voltage surges caused by synchronization transients while it is reaching for the condition in (4.8). Converter switching is turned on when other modes of operation are enabled, along with the

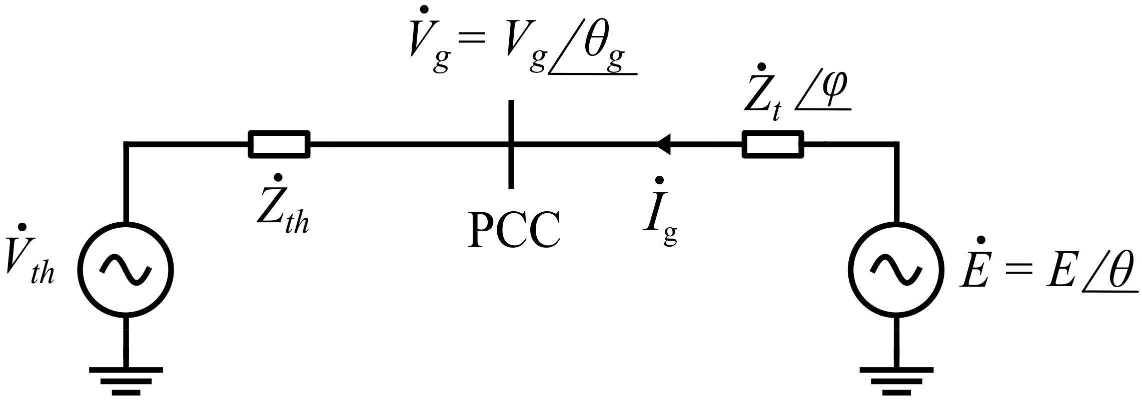

Figure 4.4: S-STATCOM one-line diagram

DC bus voltage control.

### 4.2.2 CL 2: Active power loop

For a non-generating synchronverter, the damping factor $D_p$ does not have the same meaning of frequency drooping compared to the original synchronverter since it does not exchange active power with the grid [5]. Compared to a real SG, it can be interpreted only as a mechanical friction coefficient in the small-signal model. From a control point of view, $D_p$ is essential for the active power loop stability and should not be removed unless utilizing the variant of [5]. Without it, the control path from $\Delta T_m$ to $\theta$ would become a double integrator, which may lead to instability. Although in [4] the damping coefficient is removed, this is possible only because the DC bus voltage is made constant, which is not true in a more realistic scenario, where this voltage is tied to some sort of energy storage and/or power availability at the energy source and varies accordingly with any changes in it. Therefore in [5], the virtual damping coefficient is kept and re-positioned in parallel with the inertia integrator, transforming the frequency droop loop first-order low-pass filter structure in a PI controller and, consequentially, the active power loop in an enhanced-PLL.

In the S-STATCOM model, virtual damping $D_p$ is also maintained but in its original position, forming a low-pass first order filter with time constant $\tau_f = 2H/D_p$. This is due to two reasons: 1) to take advantage of the self-synchronization algorithm in [64] and 2) to keep the significance of $H$ as an energy storage indicator for inertial response as in a standard SG model, unlike in [5] and [2] where it only represents a swing time and the actual system inertia is represented by external energy storage controls. The role of the active power loop then stays the same, which is to maintain grid synchronization by balancing $T_D$, $T_m$ and $T_e$.

For the S-STATCOM, $T_m$ will represent the amount of active power needed to cover converter losses and maintain the DC bus voltage regulated at a reference value. This is realized by a PI controller in CL 2 (Figure 4.3). The minus sign in its output indicates that the active power direction is from grid to S-STATCOM.

### 4.2.3 CL 3: Decoupled Reactive power and Voltage Regulation Loops

The synchronverter in [2] has the voltage droop loop inside the reactive power control loop that acts as the additional reference needed to execute the reactive power sharing. However, it is unable to regulate voltage at its terminals. The strategy proposed in [3] that makes the reactive power and voltage error signals to interact with the virtual flux $M_f i_f$ integrator independently, creates two independent control loops for reactive power exchange and terminal voltage regulation, called Q-mode and V-mode. In addition, the voltage drooping capability is maintained by adding both error signals to the $M_f i_f$ integrator, and it is called Droop-mode. This strategy is adopted in the S-STATCOM model and each mode is explained in detail in the next sections.

#### Direct reactive power exchange: q-mode

In this mode of operation, S-STATCOM controls the reactive power at its terminals to follow a specified reference value. Operating the S-STATCOM in this mode requires that the control switches conform to Table 4.1. In it, the virtual flux $M_f i_f$ is generated from the comparison $\Delta q = q^* - q$ given by

$$M_f i_f = \frac{1}{K_Q} \int \Delta q dt. \tag{4.9}$$

Since $M_f i_f$ is proportional to the amplitude $E$ of the internal voltage $\mathbf{e}$, a $\Delta q \neq 0$ produces a variation of $E$ which in turn varies $V_g$, which is the amplitude of the PCC voltage $\mathbf{v}_g$. Therefore, because of the integrator in the loop, $q$ will vary until it reaches $q^*$ with no steady state errors, provided that $q^*$ is constant.

#### PCC voltage regulation: V-mode

Variations in load on the grid cause fluctuations in voltage $\mathbf{v}_g$, especially if the grid is weak. This affects the power quality of the loads supplied by this connection point and may cause them to malfunction. This fluctuation also affects the stability of the grid as a whole, so one of the main functions of a STATCOM is the voltage control at its connection point. Operating the S-STATCOM in this mode requires that the control switches conform to Table 4.1. It works similarly to q-mode: from the comparison $\Delta V = V_g^* - V_g$, the change in virtual flux $M_f i_f$ generates a variation in $E$, which in turn varies $V_g$ until it reaches the reference value $V_g^*$. Change in $M_f i_f$ for this mode is given by

$$M_f i_f = \frac{1}{K_V} \int \Delta V dt. \tag{4.10}$$

For correct operation of this mode, it is necessary that a method of amplitude detection is implemented to detect the voltage amplitude $V_g$ to be regulated. Since the S-STATCOM model is in the $\alpha\beta$ reference frame, amplitude detection is realized simply by applying the relation:

$$V_g^+ = \sqrt{(v_{g\alpha}^+)^2 + (v_{g\beta}^+)^2}. \tag{4.11}$$

Unlike in [2], the S-STATCOM does not need a low-pass filter in a practical implementation of the amplitude detection block, because its input receives the filtered, positive sequence components of the DSOGI+PNSC block, which will be better explained in Section 4.2.4. For calculations of $T_e$ and $q$ however, low-pass filters tuned to damp $2\omega$ oscillations are necessary, because the currents involved in the calculations are expected to be unbalanced.

### Droop Mode

This mode is responsible for the reactive power load sharing with the grid and/or other devices equipped with droop control, which can be standard synchronous generators, grid-connected converters with emulating synchronous machines and so on. It does not need to be specifically between two or more S-STATCOMs. However, evaluation of these scenarios are out of the scope of this thesis.

In steady state, the integrator input that generates $M_f i_f$ for the S-STATCOM operating in Droop-mode is given by:

$$\frac{\Delta q}{K_q} + \frac{\Delta V}{K_v} = 0. \tag{4.12}$$

Therefore, the voltage droop $D_q = -\frac{\Delta q}{\Delta V}$ defined in [2] is of the form:

$$D_q = -\frac{\Delta q}{\Delta V} = \frac{K_q}{K_v}. \tag{4.13}$$

From this relation, the parameters $K_q$ and $K_V$ are adjusted according to [3]. The voltage droop $D_q$ is a S-STATCOM design parameter and is defined here so that the converter delivers its nominal reactive power to a variation of 10 % of its nominal operating voltage, i.e, in pu:

$$D_q = \frac{Q_n}{0.1 V_n} = \frac{1}{0.1} = 10\ pu, \tag{4.14}$$

where $Q_n$ is the nominal capacity and $V_n$ is the nominal amplitude of the phase-to-neutral voltage of the system. The time constant of the voltage control loop, according to [2] is:

$$\tau_v \approx \frac{K_v}{\omega_n} = K_v \Rightarrow \omega_n = 1\ pu. \tag{4.15}$$

The value of this time constant is chosen as one cycle of the grid voltage. Once defined, $K_q$ can be calculated from (4.13) as:

$$K_q = K_v D_q. \tag{4.16}$$

When connected to the grid without any devices with droop control to share the reactive power load with, the S-STATCOM behavior in Droop-mode is to output reactive power in a way that the new set point in relation to $q^*$ generates a change in voltage that, in relation to $V_g^*$, meets the droop definition of the model, that is:

$$D_q = -\frac{\Delta q}{\Delta V} = -\frac{q^* - q_{droop}}{V_g^* - V_{g-droop}} \tag{4.17}$$

### 4.2.4 Voltage Imbalance Compensation Loop

As mentioned before, one of the main concerns regarding power quality in distribution and micro-grids are the voltage imbalances that may occur due to many different types of loads and DG units connected to it. For instance, charging of cycles of electric vehicles can cause significant burden on one or two phases of the system, as well as simultaneity of single-phase solar generators or simple load disconnection. Therefore, this work's proposal with the S-STATCOM is to compensate voltage imbalances at the PCC, which is achieved through the Voltage Imbalance Control Loop (VICL) shown in Figure 4.5. It was developed to take advantage of the S-STATCOM main control structure in $\alpha\beta$ reference frame, as it uses a Decoupled Second-Order Generalized Integrator (DSOGI) along with a Positive/Negative Sequence Calculation block (PNSC)[8] to extract positive and negative sequence components of measured grid voltage. For the actual signal compensation, it uses Proportional-Resonant (PR) controllers tuned at the grid frequency.

Two features are worth noticing on this scheme: the resonant frequency of the DSOGI is tuned online by the active power/frequency droop loop and its positive sequence voltage output is used to feed the voltage control loop without the need of extra filters to attenuate $2\omega$ frequencies. The negative sequence estimation could be accomplished with standard notch filters tuned to $2\omega$, however, if the grid frequency is slightly different than nominal, i.e. on an isolated microgrid with no hierarchical control to bring its value back to nominal, the notch filter would distort the negative sequence component and feed the controller with it, degrading its overall performance. Since the DSOGI is an adaptive filter, this issue may not affect the

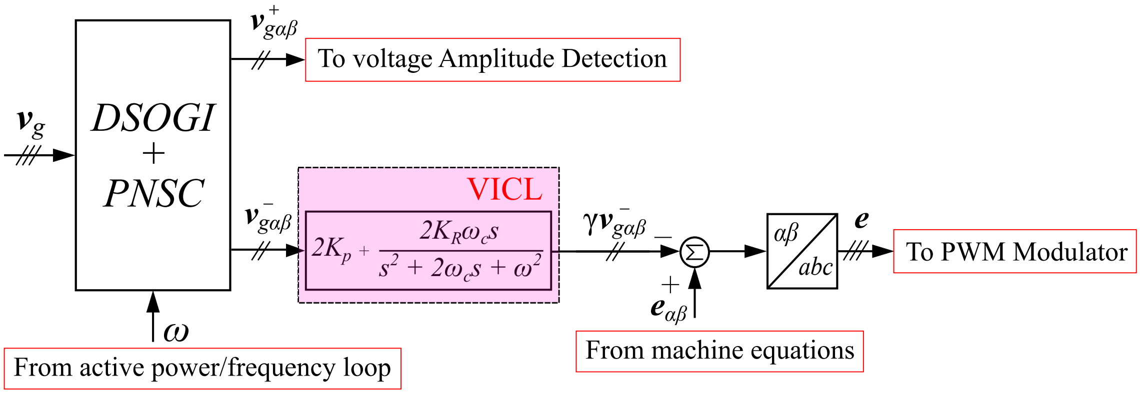

Figure 4.5: Grid unbalance control strategy

proposed controller. This evaluation will be left for future work.

The voltage imbalance compensation (VIC) works as follows: the negative sequence voltage components acquired by the DSOGI pass through a couple of PR controllers tuned at the grid frequency. The resulting signal is then *subtracted* from the back-EMF signal $\mathbf{e}_{\alpha\beta}$ provided by the main control structure, compensating the negative sequence voltage detected from the grid. To better understand the VICL's operating principle, take the system of Figure 4.4 as baseline, where it shows the S-STATCOM connected to the grid's Thévenin equivalent.

Consider that voltage $\dot{V}_g$ at the PCC is unbalanced and of the form $\dot{V}_g = V_g^+ + V_g^-$. Zero sequence components will be ignored for this analysis, since the proposed system is three-wire. With voltage unbalance control enabled, back-EMF voltage $\mathbf{e}$ will also have a negative sequence component generated by the controller, resulting in a signal of the form $\dot{E} = E^+ + E^-$. Positive and negative sequence impedance of $Z_t$ linking generator model and PCC will be considered equal. Therefore, $\dot{I}_g$ will be:

$$\dot{I}_g = \frac{\dot{E} - \dot{V}_g}{Z_t} = \frac{E^+ - V_g^+}{Z_t^+} + \frac{E^- - V_g^-}{Z_t^-}, \tag{4.18}$$

when VIC is activated, $E^-$ assumes the value of $E^- = -\gamma V_g^-$ with $\gamma \geq 1$. This happens because the controller also needs to compensate the negative sequence voltage drop on $Z_{th}$ through the power/current $\mathbf{i}_g$ injected, hence its value must be higher than the one measured from the grid. The $\gamma$ factor can be an indicator of grid strength, meaning how much more negative sequence voltage (i.e. voltage and power) must be injected to bring the unbalance factor at the PCC below the desired 2% limit set by international standards [14][58]. The effect on the current is given by (4.19):

$$\dot{I}_g = \frac{E^+ - V_g^+}{Z_t^+} + \frac{-V_g^-(\gamma + 1)}{Z_t^-}, \tag{4.19}$$

which will deliver a voltage drop across the transfer impedance that compensates the negative sequence voltage at the PCC.

## 4.3 Small-signal model

To better understand the stability and dynamics of the S-STATCOM and design the $PI_{dc}$ controller regulating the DC bus voltage, a small-signal model is derived based on [47] and [5]. Consider the one-line diagram in Figure 4.4 representing the S-STATCOM connected to the grid, where $\dot{E}$ is the S-STATCOM internal voltage and $Z_t$ is the impedance between it and the PCC.

The power transferred between S-STATCOM and grid at the PCC is given by (4.4) and (4.5), which are repeated below for convenience:

$$P = \frac{1}{Z_t}[EV_g \cos(\delta - \varphi) - V_g^2 \cos(\varphi)], \tag{4.20}$$

$$Q = \frac{1}{Z_t}[EV_g \sin(\varphi - \delta) - V_g^2 \sin(\varphi)], \tag{4.21}$$

where $\varphi$ is the angle of $Z_t$ and $\delta$ is the S-STATCOM power angle. Notice that, unlike in [5], there is no need to consider system frequency resonance in this model since the S-STATCOM is targeted to distribution sized networks or smaller, which have a higher resistance, making this effect negligible.

Linearizing (4.20) and (4.21) at the operation point $P_o(E_o, \delta_o)$, change in power transferred can be written as:

$$\begin{cases} \Delta P = A\Delta\delta + B\Delta e \\ \Delta Q = C\Delta\delta + D\Delta e \end{cases}, \tag{4.22}$$

where

$$A = \frac{\Delta P}{\Delta \delta} = \frac{E_o V_{go}}{Z_t}\sin(\varphi - \delta_o), \qquad C = \frac{\Delta Q}{\Delta \delta} = -\frac{E_o V_{go}}{Z_t}\cos(\varphi - \delta_o),$$

$$B = \frac{\Delta P}{\Delta e} = \frac{V_{go}}{Z_t}\cos(\varphi - \delta_o), \qquad D = \frac{\Delta Q}{\Delta e} = \frac{V_{go}}{Z_t}\sin(\varphi - \delta_o).$$

When connected to the grid, $E_o$, $V_{go}$ and $\delta_o$ will suffer small variations. Therefore, A, B, C and D can be considered constant values, indicating a linear relationship between variation of active and reactive power with load angle and internal voltage, respectively. From here, a small-signal model of the S-STATCOM without DC bus voltage controller can be constructed as in Figure 4.6, that is valid for the main operation modes q, V and Droop.

By using the Mason's Gain formula [66], the following transfer functions are obtained:

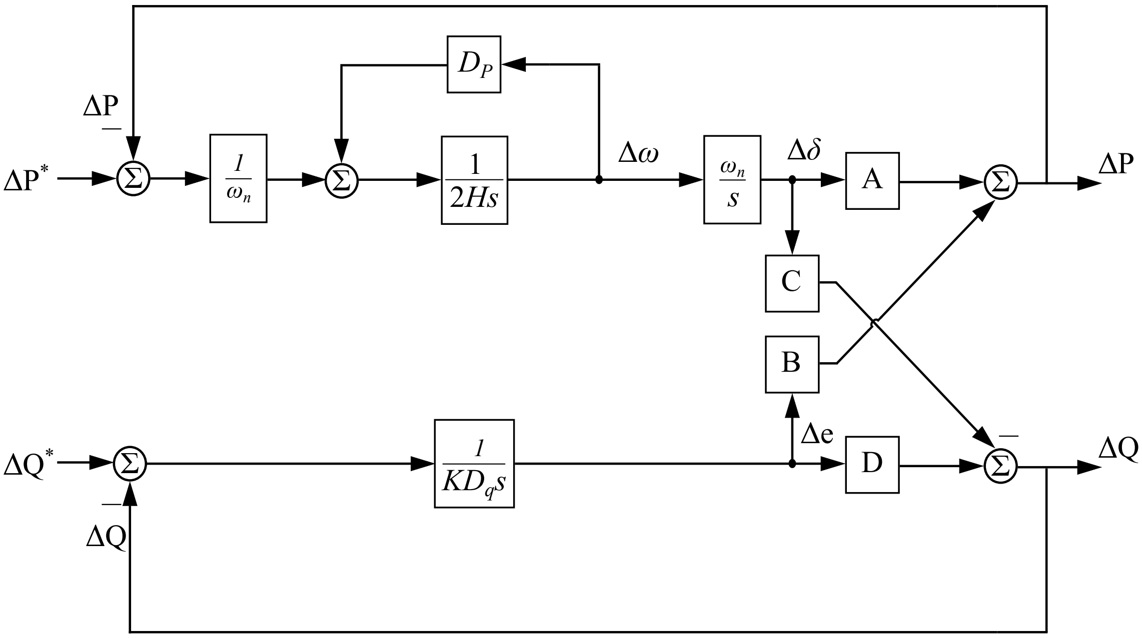

Figure 4.6: Small-signal model of S-STATCOM without DC bus voltage PI controller.

$$\frac{\Delta P}{\Delta P^*} = \frac{AKD_q s + AD}{D(s)}, \tag{4.23}$$

$$\frac{\Delta P}{\Delta Q^*} = \frac{2HBs^2 + BD_P s}{D(s)}, \tag{4.24}$$

$$\frac{\Delta Q}{\Delta Q^*} = \frac{2HDs^2 + DD_P s + AD}{D(s)}, \tag{4.25}$$

$$\frac{\Delta Q}{\Delta P^*} = \frac{-CKD_q s}{D(s)}, \tag{4.26}$$

where the eigen equation $D(s)$ is given by

$$D(s) = 2HKD_q s^3 + (2HD + KD_q D_P)s^2 + (AKD_q + DD_p)s + (BC + AD).$$

From which the stability can be evaluated. Parameters A to D are defined mainly by grid characteristics, whilst the S-STATCOM parameters $H$, $D_p$, $D_q$ and $K$ can be tuned to meet desired performance requirements. Some authors in [67] and [43] relied on adding virtual impedance to their controls and this would affect parameters A to D in this analysis, however, this is out of the scope of this work. The approach taken for tuning the aforementioned parameters is as follows:

1. The per unit inertia $H$ is fixed at its maximum value, calculated from the energy stored within the DC bus capacitor;

2. Typical synchronous generator droop parameters are chosen as a starting point;
3. Stability analysis is performed around typical variations of those parameters.

For a typical synchronverter control, it can be shown that the system is stable for a wide range of these parameters [37]. However, this may not be the case when a PI controller is added to the active power main control path, due to the addition of a free integrator. Therefore, system stability must be re-evaluated. To do so, the DC voltage PI controller is added to the active power loop as shown in Figure 4.7.

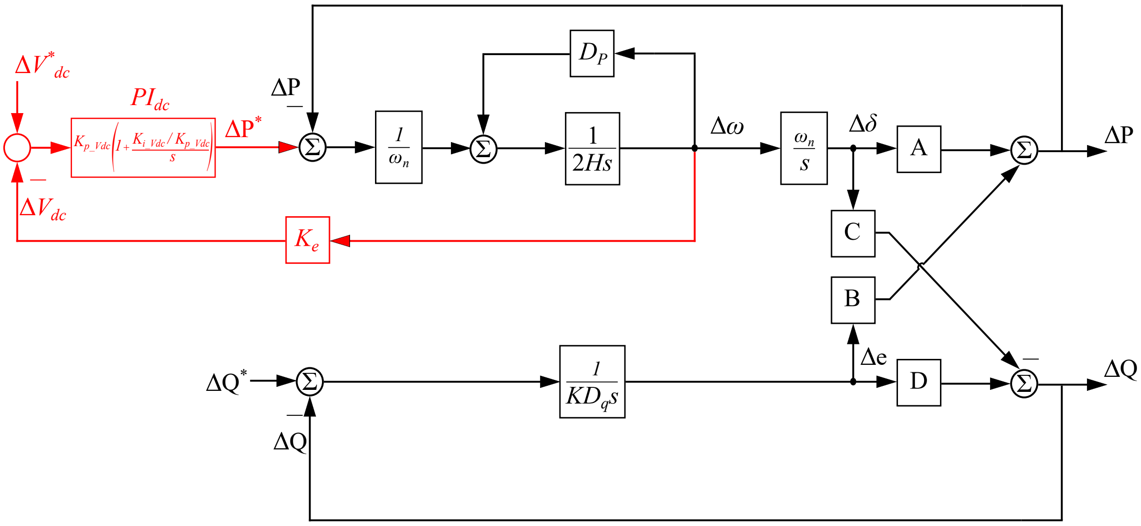

Figure 4.7: Block diagram of S-STATCOM small-signal model with PI controller

A controller in this position can be interpreted as a secondary frequency controller [5][68], which in this case, besides correcting deviations from the grid frequency, maintains the DC bus voltage at desired levels. Gain $K_e$ represents the relationship between S-STATCOM frequency and DC bus voltage, which can be related through the energy stored in the capacitor and the kinetic energy accumulated in the virtual rotor of the S-STATCOM. Those values should be equal in steady-state, therefore a maximum moment of inertia is calculated:

$$E_c = E_k, \tag{4.27}$$

$$\frac{CV_{dc}^2}{2} = \frac{J\omega_n^2}{2}, \tag{4.28}$$

$$J_{max} = \frac{CV_{dc}^2}{\omega_n^2}. \tag{4.29}$$

Then, gain $K_e$ is obtained by linearizing the same energy expressions at their respective operation points, which are the nominal frequency and DC bus voltage.

By substituting (4.29) in (4.32), the expression for $K_e$ is found

$$\Delta E_c = \Delta E_k, \tag{4.30}$$

$$CV_{dco}\Delta V_dc = J\omega_o\Delta\omega, \tag{4.31}$$

$$\frac{\Delta\omega}{\Delta V_{dc}} = \frac{CV_{dco}}{J_{max}\omega_o}, \tag{4.32}$$

$$\frac{\Delta\omega}{\Delta V_{dc}} = \frac{\omega_n^2 V_{dco}}{V_{dc}^2\omega_o}, \tag{4.33}$$

$$\frac{\Delta\omega}{\Delta V_{dc}} = \frac{\omega_n}{V_{dc}} = K_e. \tag{4.34}$$

Showing that the relationship between S-STATCOM frequency and DC bus voltage is linear. Once the nature of this relationship is established, the process of applying the Mason's Gain formula is repeated for the block diagram showed in Figure 4.7. That way, the controller's influence can be observed through all I/Os. Figures 4.8a through 4.8d show the Bode diagrams for all transfer functions with varying position of the zero introduced by the $PI_{dc}$ controller.

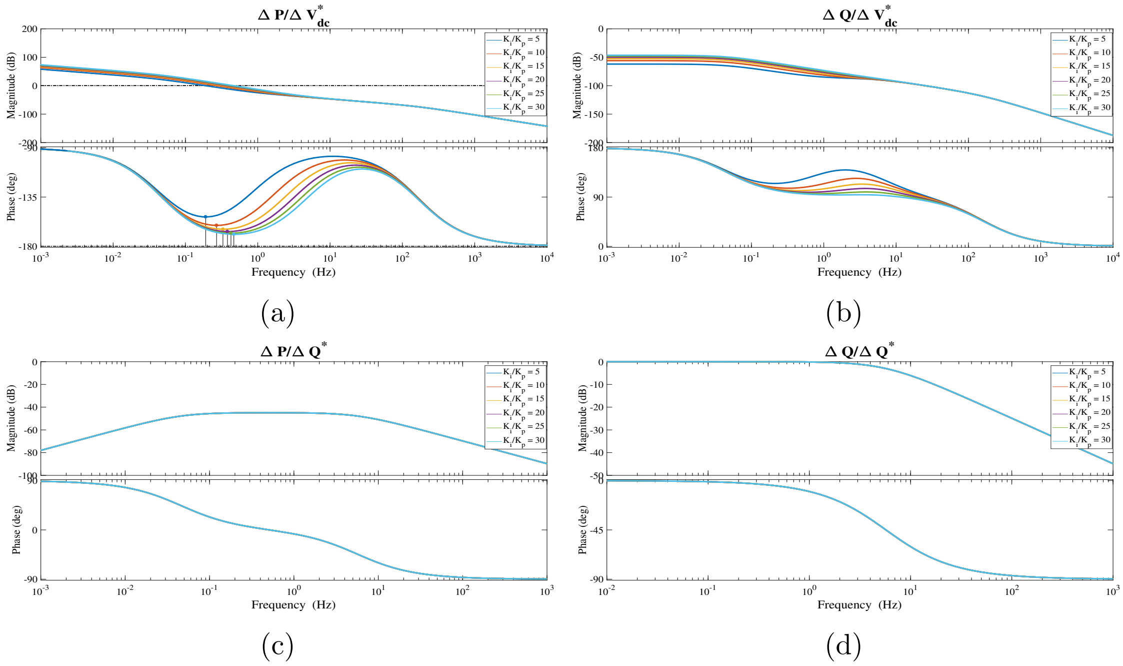

(a) (b)

(c) (d)

Figure 4.8: Bode plots of each S-STATCOM transfer function

Notice that transfer functions $\Delta P/\Delta Q^*$ and $\Delta Q/\Delta Q^*$ in Figures 4.8c and 4.8d are not affected by the controller, which is expected since it is not in their forward control path. In Figures 4.8a and 4.8b, the controller's influence is clear in $\Delta Q/\Delta V_{dc}^*$ and $\Delta P/\Delta V_{dc}^*$ transfer functions. Also, stability margins for the later are shown for different values of $K_{i_V dc}/K_{p_V dc}$. Phase margins decrease as the value of $K_{i_V dc}/K_{p_V dc}$ increases as shown in Figure 4.9, meaning that PI controller time constant $1/K_{i_V dc}$ is approaching the value of $2H$. If it gets smaller, i.e., $K_{i_V dc} > 1/2H$, the system

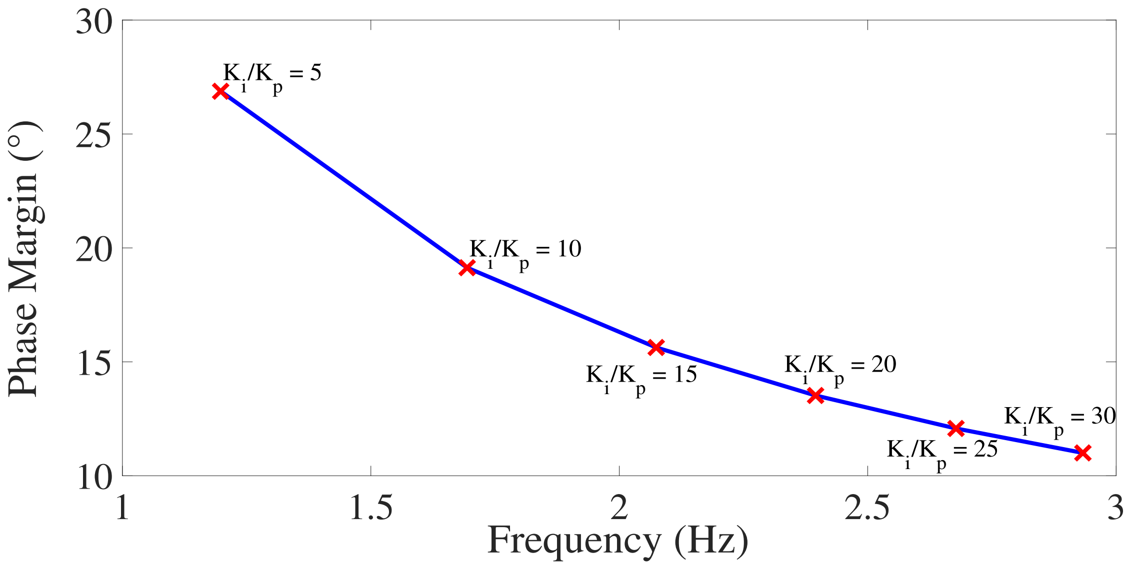

Figure 4.9: Phase Margin of $\Delta P/\Delta V_{dc}^{*}$ for different $K_i/K_p$ values.

will experience unwanted oscillations due to the controller responding faster than its inner loops and it may lose stability.

Therefore, in addition to this constraint, the performance requirements adopted in this work to tune the PI controller for the DC bus capacitor voltage are: 1) Damp oscillations that may appear in the DC bus voltage due to resonance with the filter and/or grid; 2) Minimize settling time and overshoot for the DC bus voltage. From there, the following guidelines are developed:

- $1 \leq K_{i_V dc}/K_{p_V dc} \leq 100\times$ dominant pole of $D(s)$ to ensure $K_{i_V dc} < 1/2H$;
- $0.5 \leq K_{p_V dc} \leq 1$ so that the dominant poles of $\Delta P/\Delta V_{dc}^{*}$ are the ones introduced by the PI controller.

Figure 4.10 shows the root locus of $\Delta P/\Delta V_{dc}^{*}$ zoomed in at the design region for multiple values of $K_{i_V dc}/K_{p_V dc}$. These guidelines are not set in stone. Oscillations that appear for $K_p \geq 1$ may be damped enough depending on the value of $K_{i_V dc}/K_{p_V dc}$. Values of $K_{p_V dc}$ below 0.5 result in a slower, more damped response that can be a better fit depending of the overall system performance criteria.

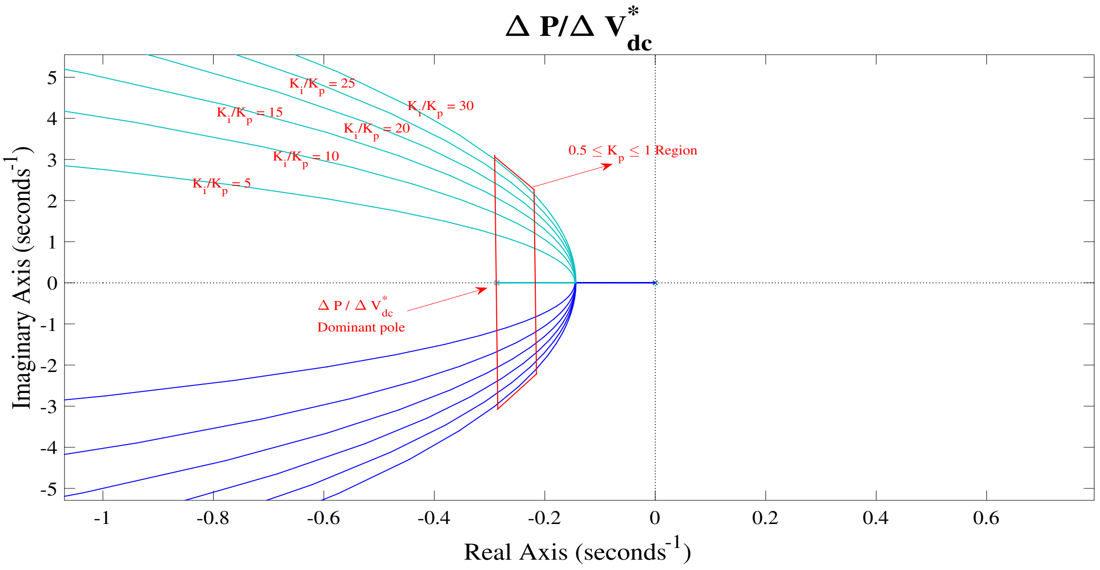

Figure 4.10: Root loci of $\Delta P/\Delta V_{dc}^*$ for different $K_{i_V dc}/K_{p_V dc}$ values, with focus on the design region.

# Chapter 5

# Evaluation of the Proposed Control

This chapter focuses on evaluating the proposed control strategy. It provides details of the workflow adopted in this thesis, which goes from building detailed simulations to assembly of a small-scale experimental prototype. Both simulation and experimental results are provided to assess the performance of the proposed control strategy.

Evaluation of the S-STATCOM control strategy begins in the first section by defining the procedures to do so, which includes guidelines for building detailed and accurate simulation environments, that are used for proof of concept and preparation for assembling the small-scale prototype.

Two simulation environments were built and its results are shown in the second and third sections, respectively. The first scenario consists of a medium voltage distribution grid Thévenin equivalent, represented as radial feeder. The S-STATCOM is connected at the feeder's end to mitigate voltage imbalance issues. The second scenario is a detailed simulation of the small-scale experimental prototype in the conditions it is expected to run, which is directly connected to the low voltage distribution grid, also represented as a Thévenin equivalent.

In the fourth section, details of the small-scale prototype assembly process are discussed, along with its results. The last section concludes the chapter with a discussion about the overall results.

## 5.1 The Implementation Process

This section aims to show the workflow in this thesis to evaluate the proposed control strategy. It provides practical guidelines for building detailed simulations and comments on the discretization process for the S-STATCOM model.

The workflow proceeded as follows:

1) Building of detailed large-scale simulation for proof of concept;
2) Building of detailed simulation for control validation in the small-scale prototype;
3) Model discretization for programming in a Digital Signal Processor (DSP);
4) Assembly of small-scale prototype.

Modeling and simulation of power systems depends on what phenomena and situation needs to be analyzed. This is especially true when power electronic converters are involved, because their operation actually changes the grid structure at each switching state [69]. This introduces several problems for offline and real-time simulations, such as numerical oscillations and DC bias in AC quantities [70]. Offline simulators such as PSCAD and MATLAB Simulink apply solutions based on switching between integration methods and variable step size to mitigate some of those issues [71].

The simulations built in this thesis are mainly to observe the behavior of a single power converter with the S-STATCOM control in its several modes of operation.

Details of switching and harmonic analysis are not the focus, but a detailed converter model is chosen anyway to evaluate the overall system performance and make sure such issues are not interfering with control stability. Therefore, the following steps are taken to ensure construction of a proper simulation environment: choosing simulation time-step, model discretization and simulation fine tuning.

### 5.1.1 Simulation time-step

Proper selection of simulation time step is required to properly observe the desired simulated system dynamics. In [72], algorithms for estimating the optimal step size and simulation time are discussed, to achieve the best compromise between model accuracy and computational time in EMTP-based simulators. The simplest one is to determine them by the following equations:

$$\Delta t = \frac{min(\mathbf{T})}{100}, \tag{5.1}$$

$$t_{max} = 5 \times max(\mathbf{T}), \tag{5.2}$$

where $\Delta t$ is the simulation time-step, $t_{max}$ is the maximum simulation time and $\mathbf{T}$ is a vector of all possible time constants of the model. Since simulations in this thesis have only one PWM driven power converter and a simple grid equivalent, it is reasonable to assume that the smallest time constant of the model is the PWM switching frequency. Therefore, $\Delta t$ is chosen as in (5.1) and the simulation time chosen will be larger than in (5.2) to show the dynamics of all S-STATCOM modes, as will be explained in the next chapter.

As for numeric integration methods, trapezoidal and backward-Euler have the best compromise between accuracy and numerical stability [71]. Both are used in PSCAD with numerical oscillation damping algorithms, while MATLAB Simulink has a variety of other methods for fixed and variable time-step simulations. In this thesis, the simulation tool chosen is Simulink with fixed time-step simulations, Tustin/Backward-Euler solver and fully discretized model components, which is similar to PSCAD simulation environment.

### 5.1.2 Model Discretization

Since the control is intended to be programmed into the DSP that will drive the experimental prototype, it must be transformed in a discrete time domain model that is stable and matches the original created in continuous time domain. For simulations in this thesis, the Simulink Model Library has discretized model components that are used in the discrete-time simulations, which makes this process easier. For the DSP however, each model equation is manually discretized and programmed in

C language into the DSP through its dedicated software. This section is intended to explain the discretization method adopted and how it is applied to the S-STATCOM simulation environment.

There are several ways to approach the system discretization problem [66]. The one used in this work is based on approximating a continuous data system in the $s$-domain into a transfer function in the $z$-domain of discrete data systems, by applying a transformation that maps the stable region of the $s$-plane into the $z$-plane. This transformation consists of substituting the variable $s$ for an expression in $z$, which is obtained by applying the $z$-transform to a time-domain expression of an integrator, represented in one of the following methods: Euler, Backward-Euler or Tustin/Trapezoidal. Each method of integration generates a different $s$ to $z$ domain transformation with its own set of advantages and disadvantages.

In this thesis, the main concern with discretizing the S-STATCOM control model is to retain its continuous time characteristics, especially its stability. Therefore, the Tustin based transformation is selected for discretizing the S-STATCOM control model, due to its main feature of mapping the stable region of the $s$-domain into the stable region of the $z$-domain. The remainder of this section is dedicated to explain the process to obtain this transformation and how it is applied in the S-STATCOM control discretization.

Consider a simple, continuous-time integrator:

$$H(s) = \frac{U(s)}{E(s)} = \frac{1}{s} \qquad \Leftrightarrow \qquad \dot{u} = e(t) \qquad \Leftrightarrow \qquad u(t) = \int_0^t e(\tau)d\tau$$

Its output given by the Tustin/Trapezoidal rule is:

$$u(kT_s) = u((k-1)T_s) + T_s\frac{e(kT_s) + e((k-1)T_s)}{2},$$

where $t = kT_s$, $k$ is the time-step index and $T_s$ is the sampling time. By taking the $z$-transform, the discrete equivalent of $H(s)$ is obtained:

$$\begin{aligned} U(z) &= z^{-1}U(z) + \frac{T_s}{2}(E(z) + z^{-1}E(z)) \\ (1 - z^{-1})U(z) &= \frac{T_s}{2}(1 + z^{-1})E(z) \\ \frac{2}{T_s}\frac{z-1}{z+1}U(z) &= E(z). \end{aligned}$$

Meaning that to discretize a continuous-time transfer function, the following substitution should by applied:

$$s \leftarrow \frac{2}{T_s}\frac{z-1}{z+1}. \tag{5.3}$$

Since this transformation maps the entire left-hand side of the $s$-plane into the unit circle of the $z$-plane, the overall frequency response characteristics of the continuous time system are maintained but with a shift at resonant frequencies, which is called frequency warping. This can be compensated by applying a frequency prewarping technique, which consists of modifying (5.3) to:

$$s \leftarrow \frac{\omega_0}{tan(\frac{\omega_0 T_s}{2})} \frac{z-1}{z+1}, \tag{5.4}$$

where $\omega_0$ is the frequency of interest that the designer wants the digital system response to match the continuous one. This is especially important for discretization of the PR controllers of the S-STATCOM that compose the VICL, which are designed by following the guidelines on [56]. The DSOGI due to its resonant nature should also be discretized with the Tustin based transformation, as it better preserves stability and frequency response of the continuous-time system, hence preventing aliasing in the output [73]. Figure 5.1 shows a comparison of different discretization methods and the effect both warped and pre-warped Tustin based transformations.

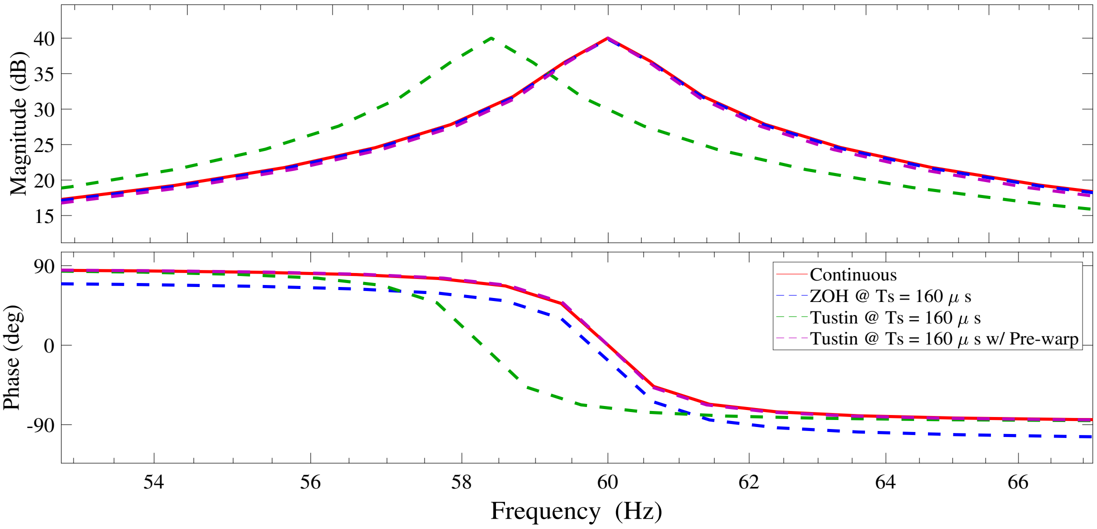

Figure 5.1: Bode-diagram of PR-controller for comparison of discretization methods. $T_s = 160\ \mu s$, $K_p = 0.1$, $K_r = 100$, $\omega_c = 3.77\ rad/s$

As stated before, the Simulink environment has discrete-type component blocks available in its library, such as PI controllers, integrators and discrete transfer functions. Those blocks allow the user to choose which integration method should be used to discretize the selected component, that can be Euler, Backward-Euler and Tustin/Trapezoidal. The discrete transfer function block allows the direct implementation of a discrete system transfer function after applying (5.3) or (5.4) to a continuous time system transfer function. Therefore, discretization of the S-

STATCOM control model in Simulink's simulation environment is achieved by using such discrete-type component blocks. In particular, the PR controllers of the VICL are implemented with the discrete transfer function blocks, which receive their resonant transfer functions discretized with the pre-warped Tustin based transformation.

### 5.1.3 Simulation fine-tuning

This step may be performed during or after the simulation assembly and it is important to close the gap between simulated and experimental results. Most actions taken here are optional for the offline simulation and it would work anyway, but are paramount for real-time implementation as will be discussed next.

When simulating controller and power system in the same environment, it is advantageous to work with two time-steps: the main smaller one for the power system and an integer multiple of it for control discretization. This is because a digital controller driving a real converter is receiving and processing information at a different speed compared to what is happening in the continuous real life system, which naturally involves the delays of measurement systems, data acquisition and processing. Therefore, these delays should be considered in the simulation.

To represent the measurement systems, a first order low pass filter with time constant representing the phase difference between input and output can be implemented. As for the data acquisition rate, a zero-order hold block can be implemented in the measured signals at a sampling time that represents the frequency which the controller process data.

A good practice to speed up the simulation is to introduce a unit step delay between systems discretized at different sampling rates, which is the case for a reference signal entering a PWM generator block. This represents the actual behavior of a digitally implemented PWM modulator, where the value stored at the comparator register only takes effect after the current PWM cycle, i.e. with a one period delay. It also allows the simulator prioritize calculation of the faster block and is useful to break unwanted algebraic loops, such as the one formed by CL 1b in Figure 4.3.

Additional measures should be taken concerning integrator blocks and PI controllers in the model, mainly to prevent numerical overflow and outputs outside critical values that can potentially damage the controlled quantity, such as the PI controller for the DC bus voltage. Those actions are: output saturation, accumulator reset and anti-windup.

Saturation means enforcing upper and lower limits to the integrator output, preventing unwanted behavior of the control. However, if its output stays for too long at a limit, the accumulator may reach very large values, i.e it winds-up. When the input changes signs and starts unloading the accumulator, it will take some time before it returns to the linear region. For a PI controller, this means a slower, oscillatory response that is undesired. To solve his problem, there are anti-windup techniques that prevents the accumulator to load beyond the saturation limits. Here, this technique is implemented through a logic that stops the integration action if the PI controller output is greater than a saturation limit and the signs of its input and output signals are the same. The pseudo-code is:

```
IF PI_Output((k-1)Ts) >= UpperLimit AND PI_Output((k-1)Ts) > 0 AND...
PI_Input(kTs) > 0 THEN
PI_Output = UpperLimit
ELSE IF PI_Output((k-1)Ts) <= LowerLimit AND PI_Output((k-1)Ts) < 0 AND...
PI_Input(kTs) < 0 THEN
PI_Output = LowerLimit
ELSE
Resume integration
```

A particular case of integrator that is expected to suffer numerical overflow if not dealt accordingly is the one that generates the phase angle in CL 2 (Figure 4.3). Its output increases linearly from 0 to $2\pi$ and back again to zero at the specified frequency, generating the internal voltage phase angle. In the offline simulation, this resetting action for the phase angle can be easily implemented by a MOD function with integrator output as numerator and $2\pi$ as denominator. However, the integrator is still increasing its value, demanding more memory, processing time and closer to reaching numerical overflow. This can not happen in real-time implementation, therefore the reset action should also assign the new integrator output to the accumulator variable. The pseudo-code for this action is:

```
IF u(kTs) >= 2*pi THEN
u(kTs) = u(kTs)-2*pi
u((k-1)Ts) = u(kTs)
```

## 5.2 Simulation Results - Scenario 1: 25 kV Distribution Feeder setup

Distribution feeders are more prone to power quality issues, such as voltage imbalances and harmonics, due to their proximity of non-linear loads such as electric vehicles, single-phase DG units and uneven load distribution throughout its phases. These conditions are favorable to the implementation of equipment such as the D-STATCOM [16], to mitigate or eliminate power quality issues. For this reason, the system model chosen to test the S-STATCOM is based on [10], which is a 25 kV three-wire distribution feeder represented by an equivalent network and the D-STATCOM connected to one of its buses, as shown in Figure 5.2.

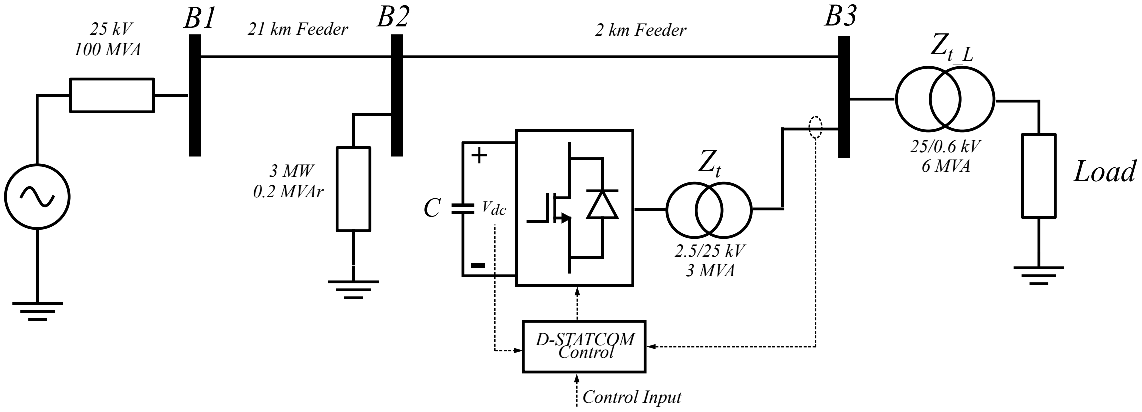

Figure 5.2: Grid used for analysis of D-STATCOM in [10]

Grid parameters of the model remained mostly the same and are shown in Table 5.1. A 25 kV distribution network is represented by a Thévenin equivalent at bus 1. Then, a 21 km feeder modeled as a pi-equivalent circuit connects bus 1 to bus 2 and a 3 MW load. A 2 km feeder modeled as a simple inductive impedance connects bus 2 to bus 3, followed by a load connected through a 25/0.6 kV transformer. The D-STATCOM is connected in parallel with the whole system through three $1.25/[25/\sqrt{3}]$ kV transformers in $\Delta - Y_g$ configuration.

Table 5.1: Scenario 1 Grid parameters.

| *Parameter* | *Value* | *Parameter* | *Value* |
|---|---|---|---|
| $S_{short-circuit}$ | 100 $MVA$ | $C^0_{feeders}$ | 5.338 nF/km |
| $V_n$ | 25 kV | $f_n$ | 60 Hz |
| Grid $X/R$ | 10 | $S_{t-L}$ | 6 MVA |
| $R^+_{feeders}$ | 0.1153 $\Omega/km$ | $X_{t-load}$ | 0.05 pu |
| $R^0_{feeders}$ | 0.3963 $\Omega/km$ | $X_{t-L}/R_{t-L}$ | 60 |
| $L^+_{feeders}$ | $1.048 \times 10^{-3}$ $H/km$ | Load transformer ratio | 25/0.6 kV $\Delta - Y_n$ |
| $L^0_{feeders}$ | $2.730 \times 10^{-3}$ $H/km$ | | |
| $C^+_{feeders}$ | 11.33 nF/km | | |

Since both S-STATCOM and the D-STATCOM from this model are PWM-based, its converter components and structure are also maintained. It consists of a voltage-source PWM inverter with two IGBT three-phase bridges in a twin configuration, a 10000 $\mu$F capacitor as a dc source and an LC filter bank to attenuate voltage and current harmonics, as shown in Figure 5.4. This inverter configuration behaves as three single-phase, full-bridge inverters with unipolar voltage switching PWM. The main three-phase bridge receives the PWM control signal and the other receives the same signal displaced by 180°, producing voltages with its fundamental components also displaced by 180°. When they sum up at the output to form each phase voltage, the resulting waveform has harmonics that appear only at double the switching frequency when its modulation index is even, as opposed to an odd value in regular bipolar switching scheme [74]. This allows converter operation at lower switching frequencies and utilization of smaller filters to suppress voltage harmonics. In addition, the IGBTs for each bridge can be rated at half the desired output voltage of the system, since the line voltages are distributed across four switches instead of two. Each three-phase IGBT bridge is represented by a single block in Simulink, that considers each of the six IGBTs as an ideal switch in series with an on-state internal resistance $R_{on}$ and a forward threshold DC voltage source $V_f$. Also, in parallel with each IGBT model, there is a series $R_{sb}$-$C_{sb}$ snubber circuit and an antiparallel diode, modeled as a forward DC voltage source $V_{fd}$ when conducting. Figure 5.3 shows the described bridge model in detail. All converter parameters are shown in Table 5.2 and are the default values from the system in [10].

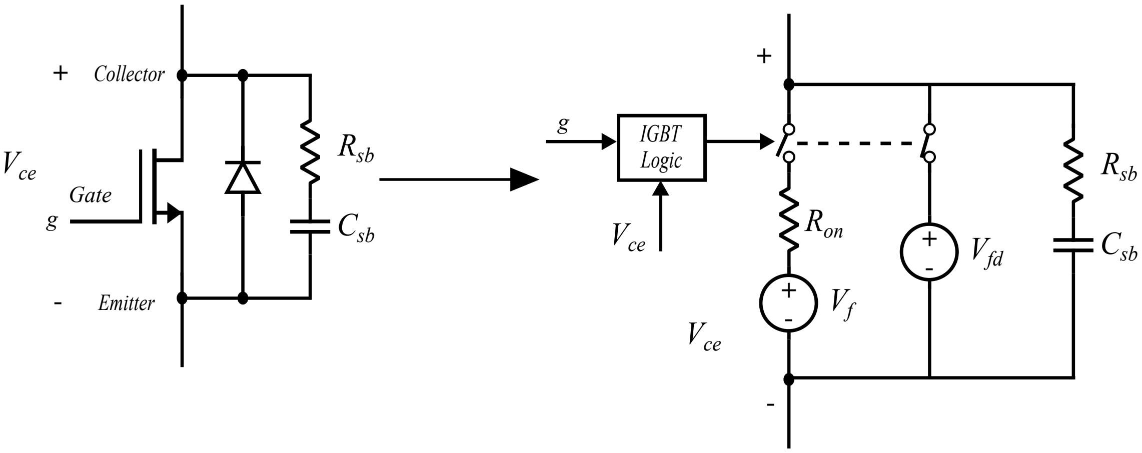

Figure 5.3: IGBT model used in the three-phase bridge model in Simulink.

Table 5.2: Scenario 1 Converter parameters.

| *Parameter* | *Value* | *Parameter* | *Value* |
|---|---|---|---|
| $S_{n/base}$ | $3\ MVA$ | $C_d$ | $10000\mu F$ |
| $V_{n/base}$ | 25 kV | DC bus voltage | 2400 V |
| Coupling transformers $X/R$ | 30 | Switching Frequency | 1680 Hz |
| $S_t$ | 1 MVA ×3 | $R_{sb}$ | 1 kΩ |
| $X_t$ (at transformer base) | 0.03 pu | $C_{sb}$ | 10 $\mu$F |
| Coupling transformers ratio | $1.25/25/\sqrt{3}$ kV | $R_{on}$ | 0.001 Ω |
| $L_f$ | $800\mu H$ | $V_f$ | 2 V |
| $C_f$ | $100\mu F$ | $V_{fd}$ | 0.8 V |
| $R_f$ | $0.6631\Omega$ | | |

In this scenario, the S-STATCOM control replaces the D-STATCOM's and two

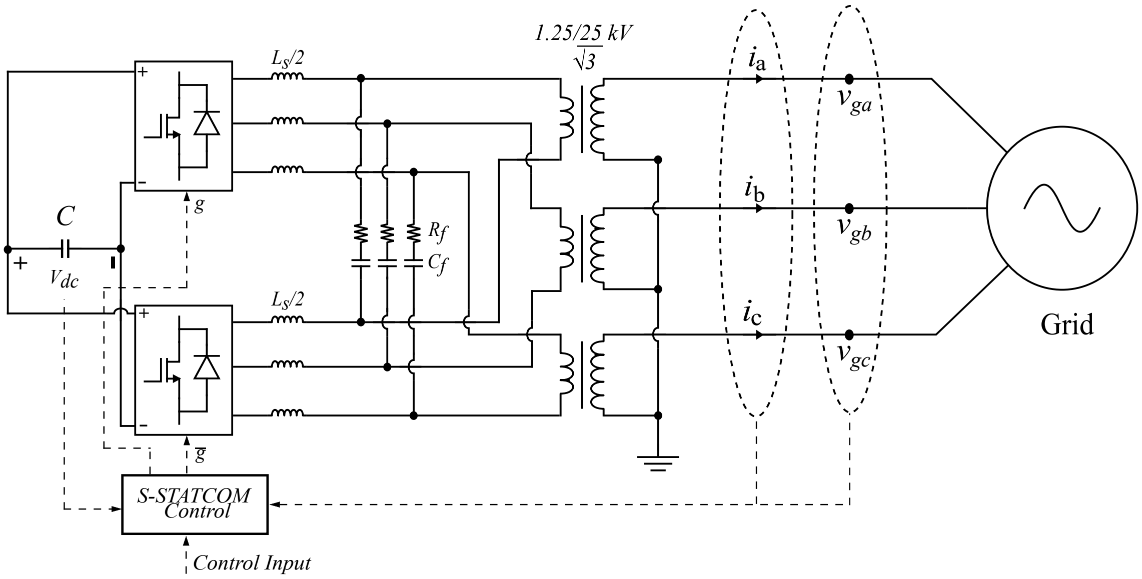

Figure 5.4: 3-ph diagram of S-STATCOM converter structure for Scenario 1 simulations

different cases are simulated. Case 1 evaluates the S-STATCOM's main functionalities: grid synchronization (Sync-mode), reactive power delivery (Q-mode), voltage regulation at the PCC (V-mode) and reactive power sharing (Droop mode). Case 2 focus on the voltage imbalance compensation capabilities and how it interacts with the main modes. Details on voltage and current dynamics, control performance and accuracy are provided throughout the simulation's events on both tests.

### 5.2.1 Case 1: S-STATCOM Main modes

This simulation will be carried on MATLAB/Simulink environment. The model is fully discretized using the bilinear method. Inverter switching frequency is $f_s = 1.68\ kHz$ and simulation time-step is set to 5 $\mu$s (120 times smaller than the switching period $\tau_s$), providing enough resolution to represent harmonics and system dynamics [72]. Control inputs and outputs are sampled at 32 times the simulation time-step, which is 160 $\mu$s, using zero-order hold blocks. The load connected to bus 3 will be a balanced three-phase 5 MVA load with 0.8 inductive power factor as shown in Figure 5.5. No imbalances will be inserted in the simulation at this time.

Control parameters of the S-STATCOM are calculated according to Chapter 4 and presented in Table 5.3. The model is initialized with $\omega_{init} = 1.0\ pu$ as initial condition for the inertia integrator, otherwise it will incur in a singularity when calculating $T_e$.

Table 5.3: Scenario 1 Control parameters.

| *Parameter* | *Value* | *Parameter* | *Value* |
|---|---|---|---|
| H | 9.6 ms | $L_{sync}$ | $5 \times 10^{-4}$ pu |
| $D_P$ | 20 | $K_{p-Vdc}$ | 0.5 |
| $D_Q$ | 10 | $K_{i-Vdc}/K_{p-Vdc}$ | 10 |
| $K_Q$ | 0.16 | $K_{p-VICL}$ | 0.1 |
| $K_V$ | 0.016 | $K_{R-VICL}$ | 100 |
| $K_{p-Sync}$ | 0.5/377 | $\omega_c$ | 3.77 rad/s |
| $K_{i-Sync}$ | 20/377 | $k_{DSOGI}$ | $\sqrt{2}$ |
| $R_{sync}$ | 0.01 pu | | |

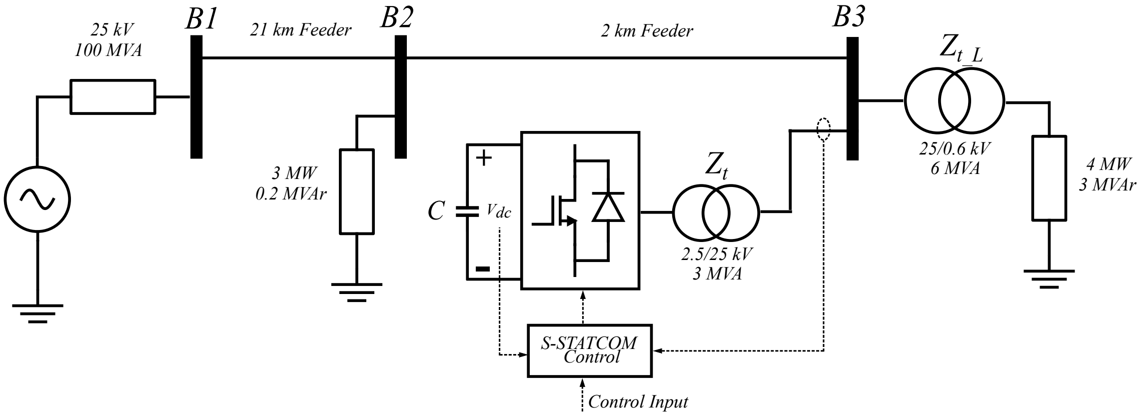

Figure 5.5: One-line diagram of the Case 1 system

### Startup and synchronization

Simulation starts at $t = 0s$ with the S-STATCOM's switches turned off and the DC bus capacitor being charged up through the diodes. Voltage at the PCC is 0.97 pu due to the heavy load. At $t = 0.5s$, the control is turned on in Sync-mode and it starts synchronizing with the grid, which takes less than 0.2s according to Figure 5.6. Grid frequency is successfully tracked, voltage difference between $\mathbf{e}$ and $\mathbf{v}_g$ stays constant and around 2%. Also, voltage amplitudes and phase difference, shown in Figures 5.6b and 5.6a respectively, meet the conditions defined in (4.8), meaning the synchronization algorithm ensures the converter stays synchronized until an order to switch modes is deployed and the the converter switches are turned on.

### S-STATCOM main modes

At $t = 1.0s$, the S-STATCOM enters in q-mode, simultaneously activating the IGBT bridges, DC bus capacitor voltage control and deactivating the grid synchronization algorithm. The initial harsh transient is due to the DC bus voltage control following a step in its reference value. This behavior is expected and it is not a problem in a simulation environment, but must be taken care of in any real-time

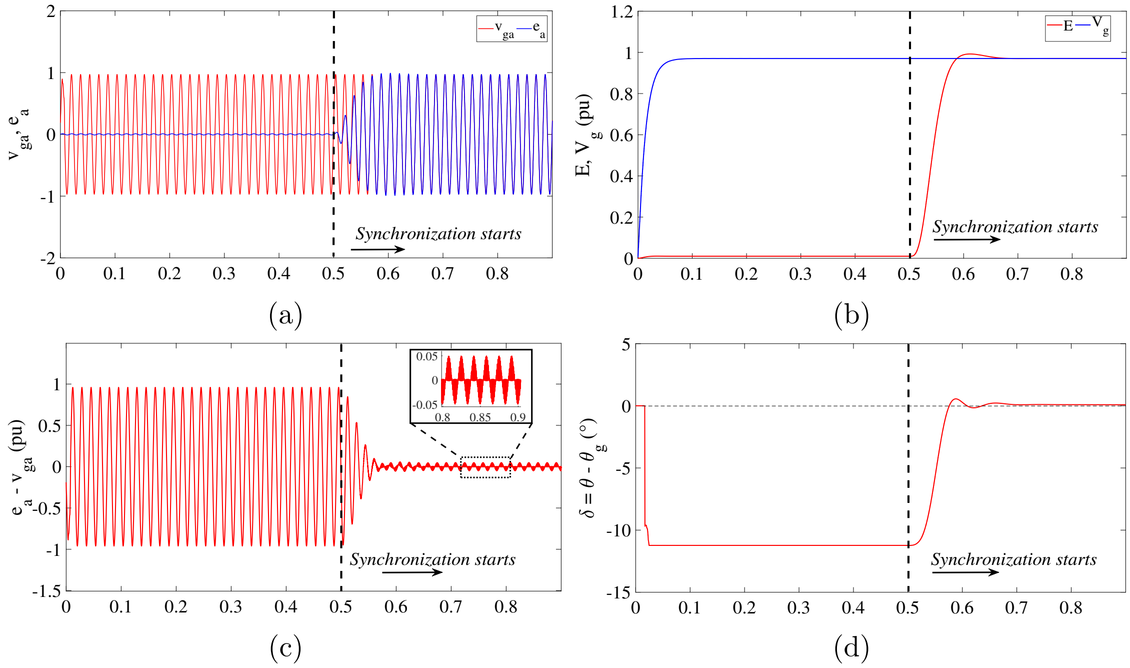

(a) (b) (c) (d)

Figure 5.6: S-STATCOM Synchronization Process: a) Phase A Voltages, b) back-EMF and Grid Voltage Amplitudes, c) Phase A voltage difference, d) Power angle

implementation of the system, as observed later in Section 5.4. It stabilizes after 0.2s and it is ready to operate its main modes, as shown in Figure 5.7. After initial grid synchronization, S-STATCOM is ready to receive further commands. Simulation events designed to evaluate its modes take place as follows:

1) Reactive power order of $q^* = -1\ pu$ at $t = 2.0s$;

2) Switch to V-mode with $V_g^* = 1.0\ pu$ at $t = 4.0s$;

3) Switch to Droop-mode at $t = 6.0s$;

4) Simulation ends at $t = 8.0s$.

Figure 5.7 shows the dynamics of several quantities during the events. Grid synchronization is kept throughout all simulation. On the first event, at $t = 2.0s$, the S-STATCOM is given a $q^* = -1\ pu$ control order and accurately reaches its target in 0.16s with no overshoot, as shown in Figure 5.7e. As a consequence, the PCC voltage $V_g$ decreases to 0.895 pu. Active power consumed over time is shown in Figure 5.7d and accounts for the VSI, filter and coupling transformer losses, in addition to maintaining DC bus voltage. During operation at nominal capacity, the maximum average consumed power is approximately 0.0136 pu (41 kW).

When switching to V-mode at $t = 4.0s$, reactive power goes from -1 pu (3 MVAr inductive) to 0.52 pu (1.56 MVAr capacitive) in 0.25s without overshoots,

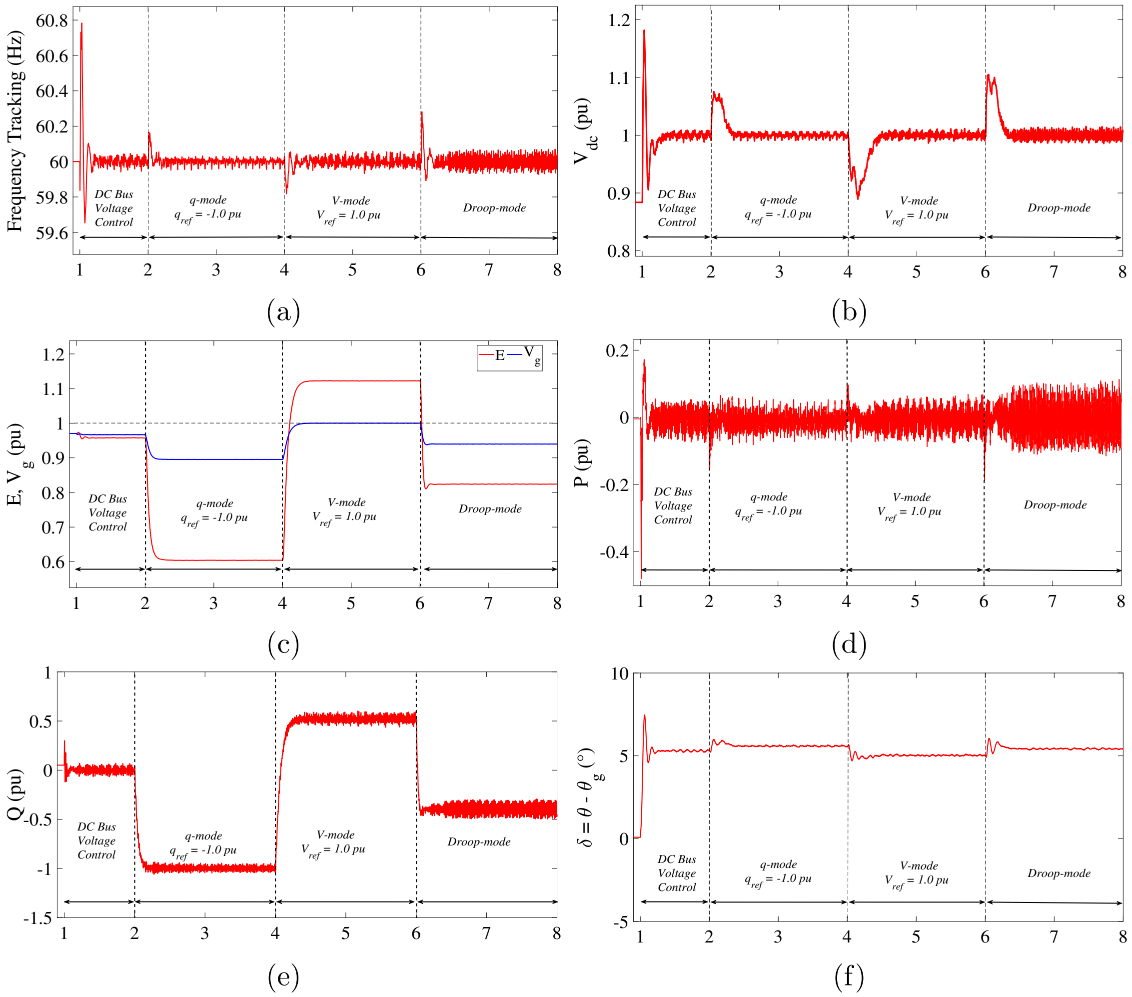

(a) (b) (c) (d) (e) (f)

Figure 5.7: S-STATCOM Main Modes: a) Frequency tracking by CL1a, b) DC bus voltage transients, c) Grid and back-EMF voltage amplitudes, d) Active Power, e) Reactive Power, f) Power angle $\delta$

successfully regulating $V_g$ at 1.000 pu, as shown in Figure 5.7c. The change from inductive to capacitive power factor was due to $V_g$ being previously below 1 pu.

The last event is the S-STATCOM switching to Droop-mode at $t = 6.0s$, sharing the reactive power load with the grid. It takes 0.15s to reach steady state, with $V_g = 0.94\ pu$ and $Q = -0.40pu$ (1.2 MVAr inductive). Therefore, the difference between reactive power states achieved by the S-STATCOM in q-mode and Droop-mode is $\Delta Q = Q_{0-Q} - Q_{0-Droop} = -1.00 - (-0.40) = -0.6\ pu$. Similarly, the difference between $V_g$ at V-mode and Droop-mode is $\Delta v_g = V_{g-V} - V_{g-Droop} = 1.00 - 0.94 = 0.06\ pu$. Substituting those values in (2.12), it gives:

$$D_q = -\frac{\Delta Q}{\Delta v} = -\frac{-0.6}{0.06} = 10. \tag{5.5}$$

Showing that the Droop-mode is also working as intended. Notice that droop control in general works to improve voltage at the PCC by sharing the reactive power load among generators and power quality devices, and in this case the PCC voltage when Droop Mode is active is worse than prior to the S-STATCOM's connection to the grid. This is due because Droop Mode takes into account the PCC voltage at q-Mode instead of its state prior to the S-STATCOM's connection to the grid, meaning that the voltage improvement in the simulation events showed above are relative to the PCC voltage when the S-STATCOM is in q-Mode with $q^* = -1$ $pu$. To obtain a PCC voltage improvement in Droop-Mode relative to its state prior to the S-STATCOM's connection to the grid, $q^*$ should be set to 0 at all times. This concludes the evaluation of the S-STATCOM main modes.

### 5.2.2 Case 2: Voltage Imbalance Compensation

The voltage imbalance compensation capabilities of the S-STATCOM will be analyzed. Simulation parameters remain the same, except for the following. To create voltage imbalance, a 200m feeder is added in between the 5 MVA load and the 25/0.6 kV transformer, along with a single-phase breaker in its phase B, which will open at a specified time to emulate an open-circuit fault and cause the voltage unbalance. Also, a 4 MW, 25 kV three-phase load L1 is added before the 25/0.6 kV transformer at bus 3, to be analyzed under the unbalanced conditions and how the S-STATCOM can mitigate them. Figure 5.8 shows the new grid setup.

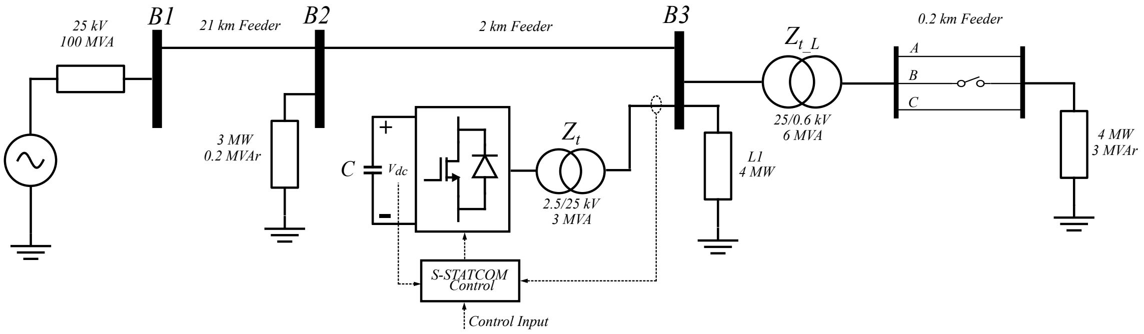

Figure 5.8: One-line diagram of the Case 2 system

As for the control structure of the S-STATCOM's voltage imbalance compensator (VIC), DSOGI and PR controllers are fully discretized with the bilinear method at 160 $\mu$s. Its parameters are calculated according to Section 5.1.2 and shown in Table 5.3

Since the synchronization process is the same in both cases, the analysis will focus on events after grid connection, which occur as follows:

1) Reactive power order of $Q_{ref} = -1$ $pu$ at $t = 1.0s$;

2) Trigger voltage unbalance by opening the 5 MVA load phase B breaker, at $t = 2.0s$;

3) Activate VIC at $t = 3.0s$;

4) Switch to V-mode with $V_{ref} = 1.0\ pu$ at $t = 4.0s$;

5) Switch to Droop-mode at $t = 6.0s$;

6) Simulation ends at $t = 8.0s$.

As in case 1, Figure 5.9 shows the dynamics of several quantities of interest for this analysis. Notice that the dynamics before the voltage imbalance is triggered are exactly the same as in case 1 (Figure 5.7). At $t = 2.0s$ when phase B of the 5 MVA load is opened, voltage at bus 3 reaches a 2.24 % VUF as shown in Figure 5.11, which is slightly higher than the recommended 2 % [14][58]. The effect on L1 active power signal can be seen on Figure 5.10, which shows a $2\omega$ oscillation with 0.05 pu amplitude (150 kW). As for the S-STATCOM, its losses are compared in three situations when operating at $q^* = -1\ pu$: VIC on, VIC off with imbalance and VIC off without imbalance. The results in Table 5.4 show that the VIC in this case contributed to the losses in 0.07%. Also, the increased $2\omega$ oscillations in active and reactive power after VIC is enabled are expected, since the S-STATCOM is now supplying all oscillating power to the load.

Table 5.4: Converter losses comparison for case 2, Scenario 1.

| *Case* | *Losses* |
|---|---|
| VIC OFF, w/o imbalance | 48.1 kW (0.0160 pu) |
| VIC OFF, w/ imbalance | 48.2 kW (0.0161 pu) |
| VIC ON | 50.1 kW (0.0167 pu) |

When the VIC is activated at $t = 3.0s$, VUF at the PCC drops to 0.06% in about 0.05s and stays at this level throughout the simulation, as shown in Figure 5.11b. Notice the power oscillation in L1 vanishes and the VIC control did not interfere significantly in the dynamics of the following events. At $t = 4.0s$, PCC voltage $V_g$ is regulated to 1.00 pu taking the same 0.25s to change its reactive power output and fulfill the control order.

To verify the Droop-mode, average reactive power is calculated for each mode when VIC is activated, since it can not be done visually because of the oscillations. Verification through (2.12) resulted in $D_q = 10.03\ pu$. This is due to the slightly higher reactive power output to supply the unbalanced grid.

When VIC is activated, it is expected that the current supplied by the S-STATCOM becomes more unbalanced to account for the oscillating power that it is supplying to compensate the imbalance in voltage, as shown in Figure 5.12. VIC is activated in the most extreme steady state case of this analysis, where $q_{ref} = -1pu$ in q-mode. Current in the affected phase $i_b$ is 28% higher then in the previous event,

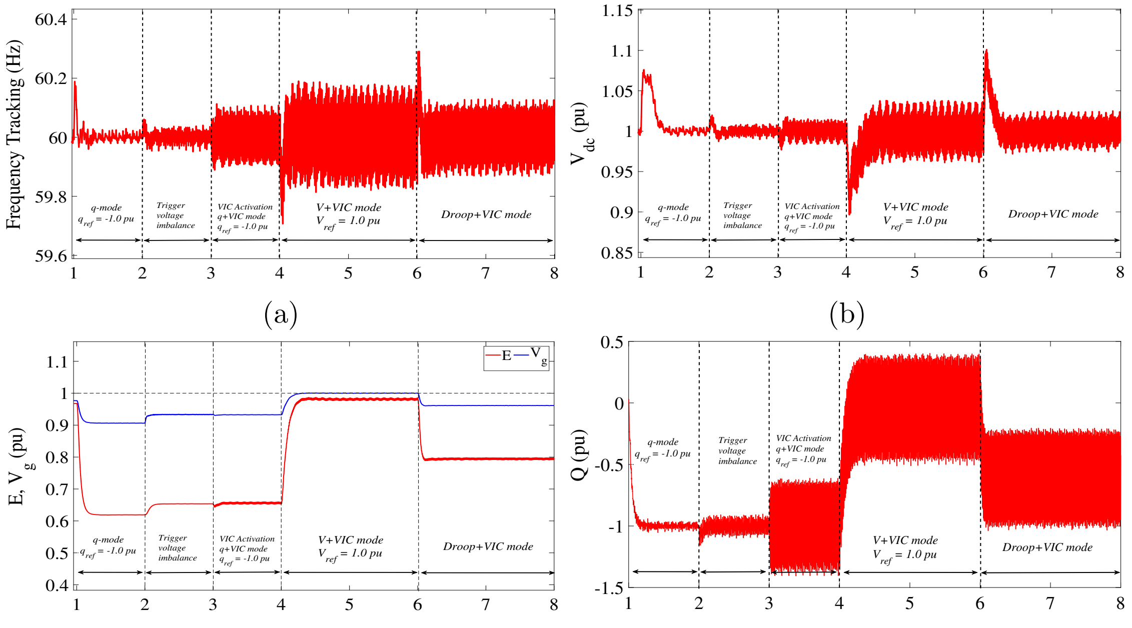

(a) (b)

(c) (d)

Figure 5.9: Results for Scenario 1 modes when VIC is on. a) Frequency tracking by CL1a; b) DC bus voltage; c) Internal and grid voltage amplitudes; d) Reactive power

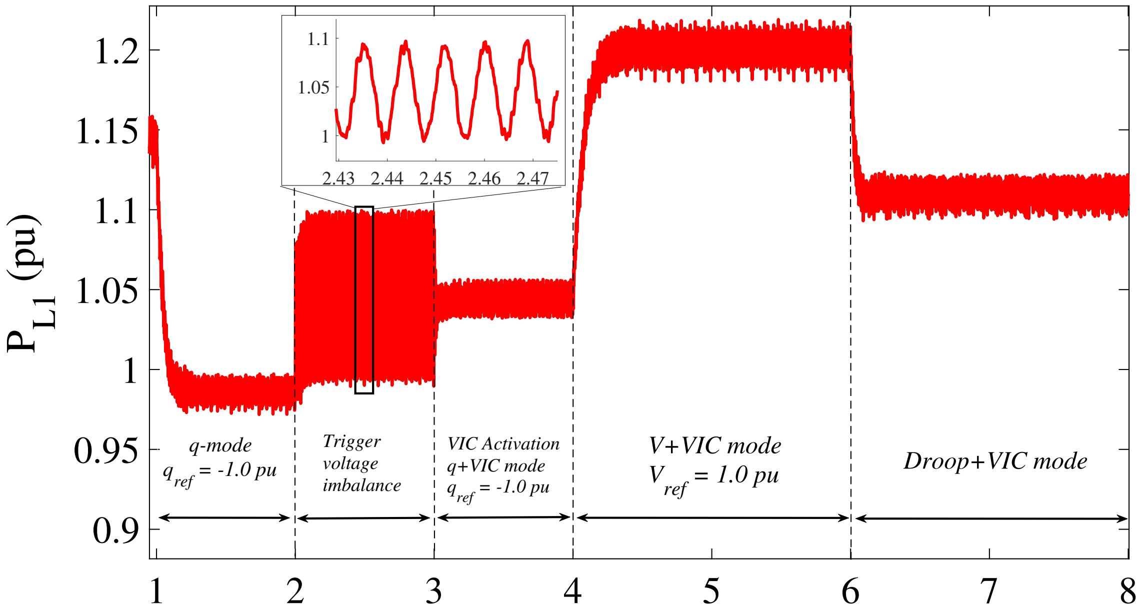

Figure 5.10: Effect of the voltage imbalance on load L1 and subsequent activation of S-STATCOM's VIC mode.

where VIC was still off, reaching 1.41 pu compared to the previous amplitude value of 1.13 pu, which would probably trigger overcurrent protections. However, in the other operating modes, which are more common to a STATCOM operation [16], the currents stayed within limits.

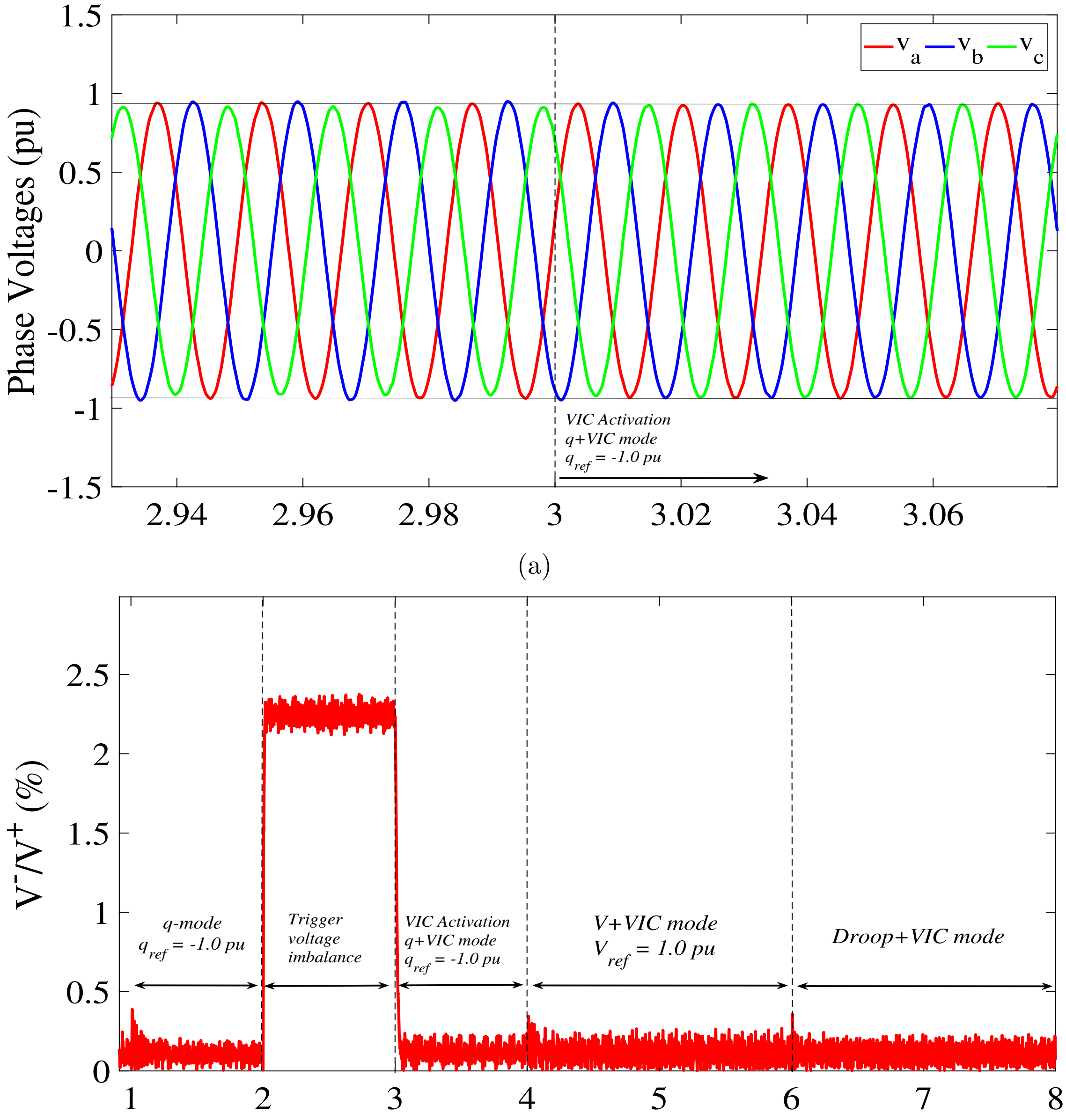

(a)

(b)

Figure 5.11: VIC performance of the S-STATCOM in Scenario 1. a) Phase voltages before and after VIC activation. b VUF throughout the simulation

## 5.3 Simulation Results - Scenario 2: Small-scale, grid connected setup

To validate the control strategy, the system showed in Figure 5.13 is simulated in the MATLAB/Simulink environment. The parameters used in the simulation are shown in Tables 5.5 and 5.6, which represent the actual ratings of the experimental prototype setup. All parameters are calculated according to the concepts and procedures shown in the previous sections. Since this setup is significantly smaller than the one in the first scenario, the PI controller gains for the DC bus voltage had

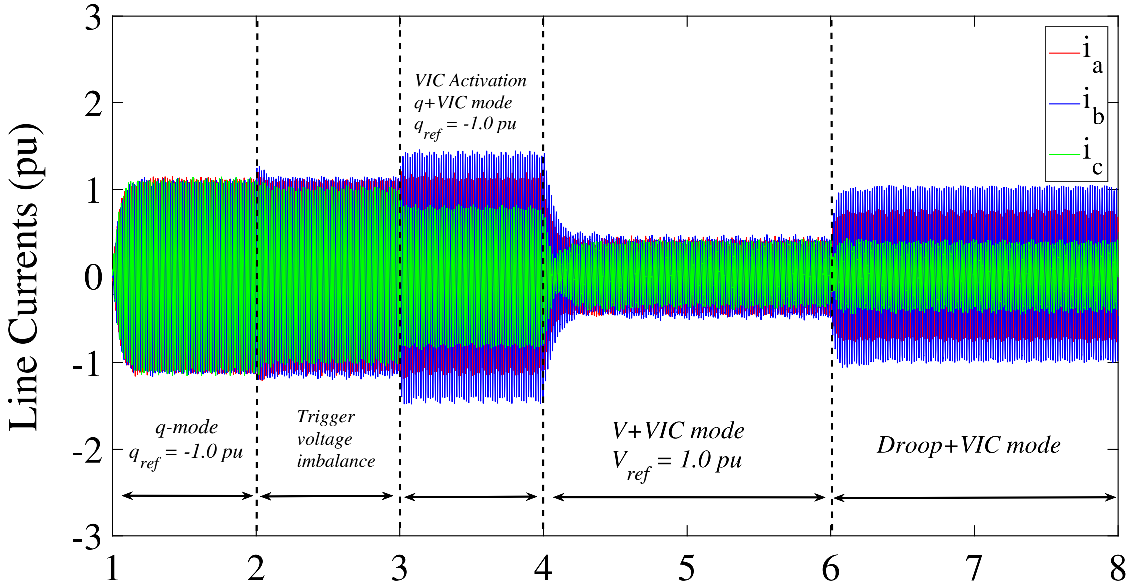

Figure 5.12: S-STATCOM line currents when VIC is activated.

to be recalculated in order to achieve better performance with the larger grid and filter impedances.

In addition, since this scenario is a preliminary step for real-time implementation, a protective measure expected in the experimental setup is implemented in the simulation, which is the addition of pre-charge resistors $R_C$ to limit the current surge in the system startup. Grid voltage is adjusted to 1.03 pu to simulate the conditions which the experimental prototype will be submitted.

Simulation was conducted with zero-order hold blocks connected to the measurements at 15 kHz switching frequency, to match the PWM-synchronized data acquisition from the small-scale prototype. Simulation time step is $T_s = 6.667 \times 10^{-7}\ s$.

Table 5.5: Scenario 2 converter parameters.

| *Parameter* | *Value* | *Parameter* | *Value* |
|---|---|---|---|
| $S_{n/base}$ | $80\ VA$ | $L_s$ | 2.2 mH |
| $V_{n/base}$ | $16.2\sqrt{\frac{2}{3}}$ V | $R_s$ | $0.14\Omega$ |
| DC Voltage | 30 V | $C_f$ | $10\mu F$ |
| $S_t$ | 150 VA | $R_c$ | $5\Omega$ |
| Transformer ratio | 16.2/220 V | $C_d$ | $7.16mF$ |
| $R_g$ | $0.05\Omega$ | $f_n$ | 60 Hz |
| $L_g$ | $570\mu H$ | Switching frequency | 15 kHz |

### 5.3.1 Startup and grid connection

Simulation starts at $t = 0\ s$ in conditions described in Section 4.2.1. The circuit startup follows the sequence of events that are described in Section 5.4.2 and are

Table 5.6: Scenario 2 Control parameters.

| *Parameter* | *Value* | *Parameter* | *Value* |
|---|---|---|---|
| $H$ | $40.3ms$ | $L_{sync}$ | $10\mu H$ |
| $D_P$ | 20 | $K_{p-Vdc}$ | 1.15 |
| $D_Q$ | 10 | $K_{i-Vdc}/K_{p-Vdc}$ | 2 |
| $K_Q$ | 0.16 | $K_{p-VICL}$ | 0.1 |
| $K_V$ | 0.016 | $K_{R-VICL}$ | 100 |
| $K_{p-Sync}$ | 0.5/377 | $\omega_c$ | 3.77 rad/s |
| $K_{i-Sync}$ | 20/377 | $k_{DSOGI}$ | $\sqrt{2}$ |
| $R_{sync}$ | $0.05\Omega$ | | |

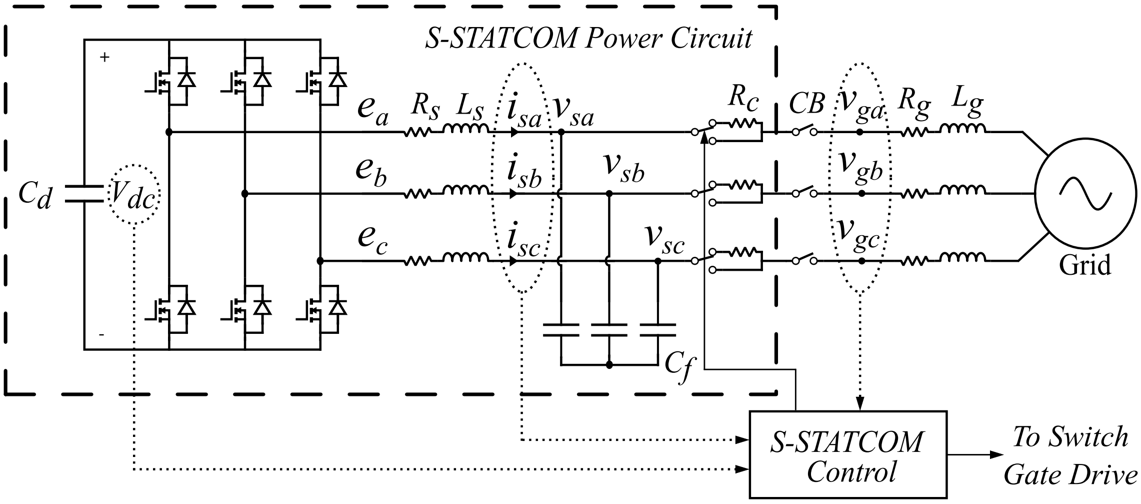

Figure 5.13: S-STATCOM power circuit

intended to mitigate the high initialization currents. Figure 5.14 shows the startup sequence results. The CB is already on and DC bus capacitor pre-charge sequence starts with the line currents barely reaching 0.5 pu, configuring a safe startup as shown in Figures 5.14a and 5.14b. Grid synchronization is reached at $t = 0.3\ s$ with smooth frequency tracking and less than 2 % error between $\mathbf{e}$ and $\mathbf{v}_g$, as shown in Figures 5.14c, 5.14d and 5.14f. At $t = 1.0\ s$, the transient from steps 4) and 5) of the startup procedure defined in Section 5.4.2 are observed in Figure 5.14, when the S-STATCOM control is switched to q-mode with $q^* = 0$ and the DC bus voltage is regulated to its reference value of 30V. The system stabilizes around $t = 0.8\ s$.

### 5.3.2 S-STATCOM Operation Modes

With the system stabilized and properly connected to the grid, the operating modes will be tested. The simulation events are:

1) Reactive power order of $q^* = -1\ pu$ at $t = 2.0s$;

2) Switch to V-mode with $V_g^* = 1.0\ pu$ at $t = 4.0s$;

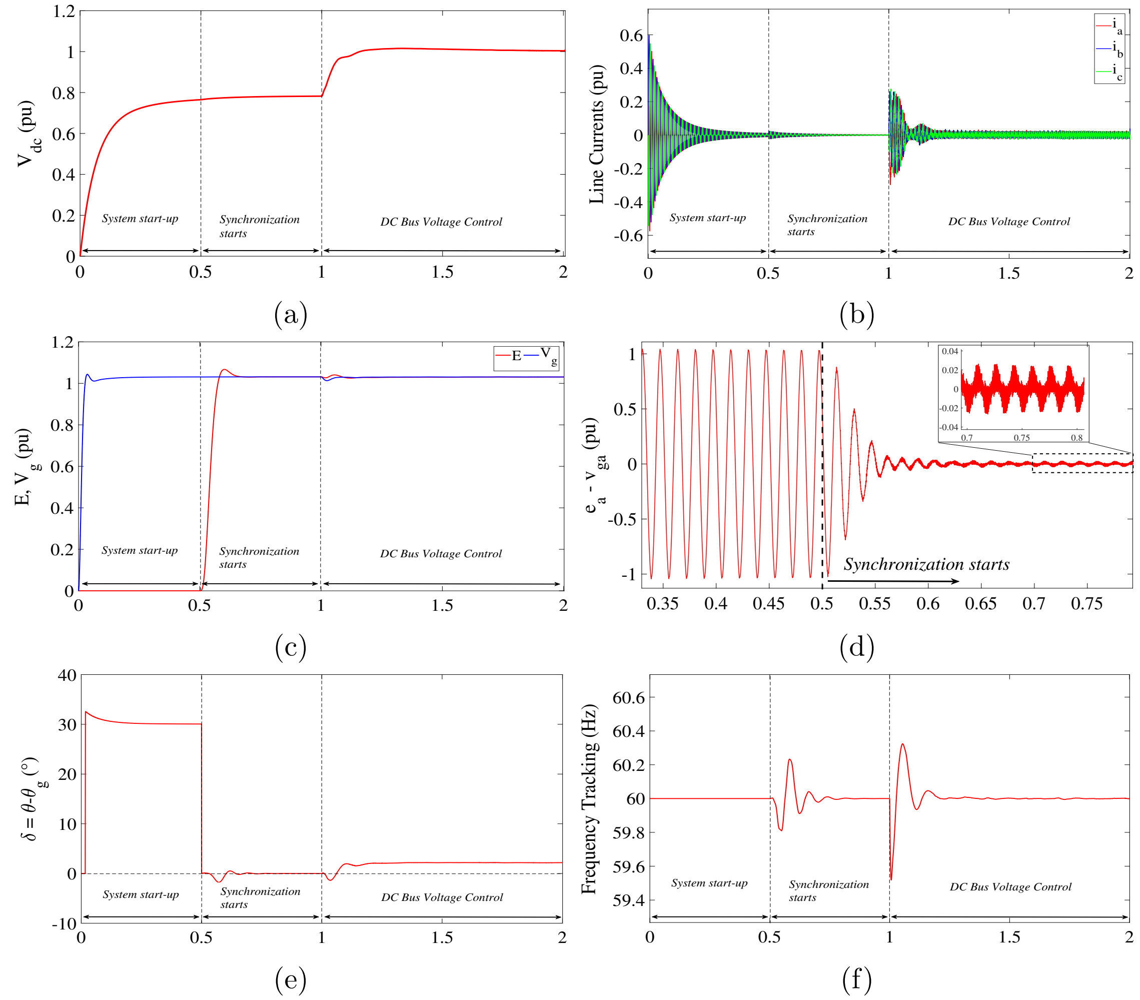

(a) (b) (c) (d) (e) (f)

Figure 5.14: Simulation results for Synchronism mode in Scenario 2. (a) DC Voltage at the capacitor, (b) Three-phase line currents, (c) Internal voltage $E$ (red) and Grid voltage $V_g$ (blue) amplitudes (d) Voltage difference $e_a - v_{ga}$, (e) Power angle, (f) Grid Frequency tracking.

3) Switch to Droop-mode at $t = 6.0s$;

4) Simulation ends at $t = 8.0s$.

Figure 5.15 shows the simulation results. DC-bus voltage was maintained in its reference of 30 V during all simulation time, showing very small dynamics in the occurrence of the events, according to Figure 5.15a. Active power also remained close to zero, enough to account for converter losses and DC bus regulation (Figure 5.15b). The S-STATCOM was able to accurately track the grid frequency at all times and showed smooth transitions between operating modes (Figure 5.15e). At $t = 1$ $s$, the reactive power order was achieved quickly and accurately by the control (Figure 5.15c). By absorbing 1 pu of reactive power (80 VAr), the voltage $V_g$ fell to 0.93 pu. On switching to V-mode at $t = 2$ $s$, S-STATCOM quickly adjusted the voltage at the PCC to 1 pu by absorbing approximately 0.32 pu of reactive power

(25.6 VAr) (Figures 5.15d and 5.15c).

After switching to Droop mode at $t = 4\ s$, the reactive power generation went to -0.67 pu, causing the voltage $V_g$ to stabilize at 0.967 pu. The change in reactive power with respect to the initial order of -1 pu and the change in voltage $V_g$ with respect to the nominal voltage are in accordance with the droop definition:

$$\frac{\Delta Q}{\Delta V} = \frac{(1 - 0.67)}{(1 - 0.967)V_n} = \frac{0.33}{0.033V_n} = 10 = D_q \tag{5.6}$$

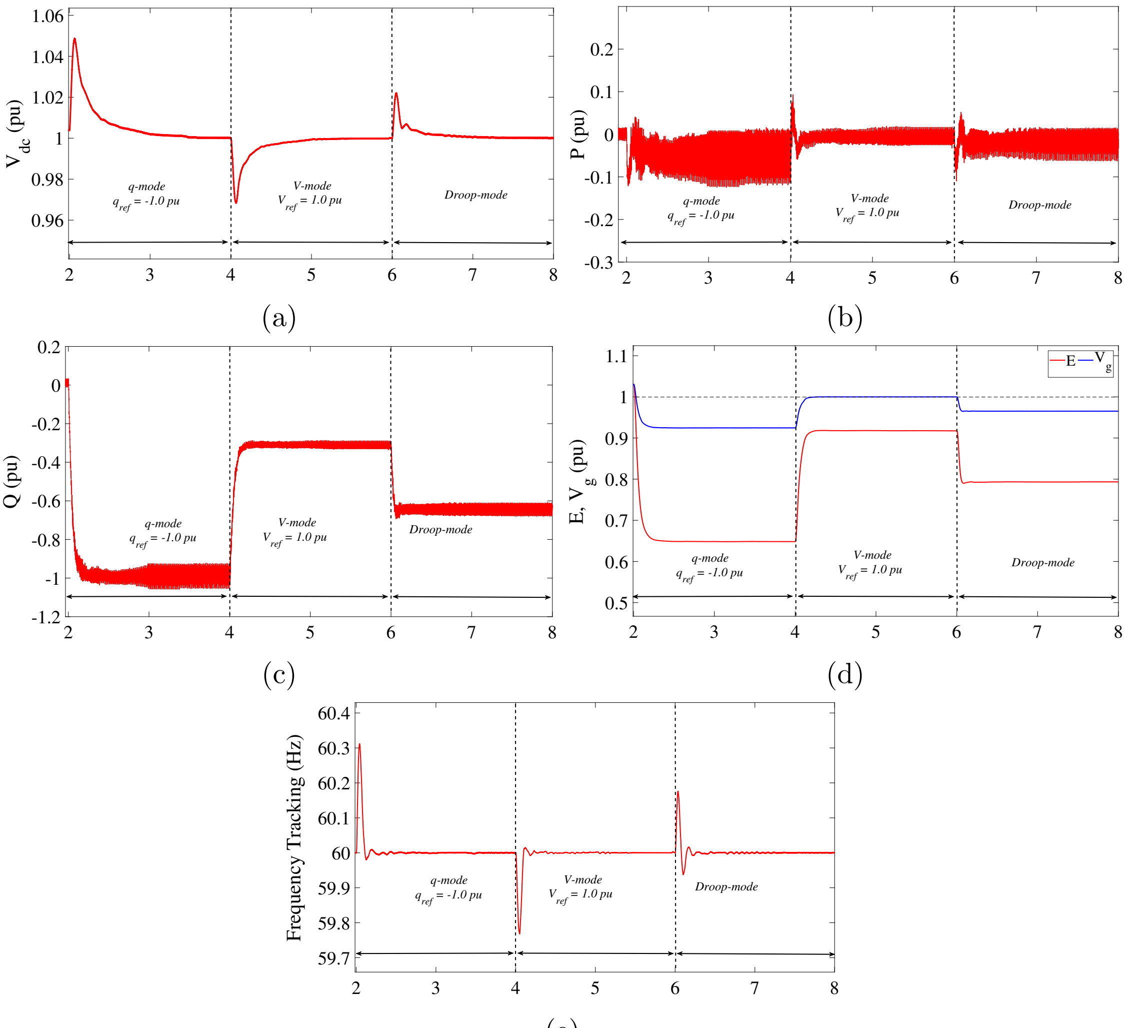

(a)

(b)

(c)

(d)

(e)

Figure 5.15: Simulation results for the remaining operation modes of Scenario 2. (a) DC bus capacitor voltage. (b) Active Power (c) Reactive power. (d) Grid (blue) and internal (red) voltage amplitudes. (e) Grid frequency tracking.

### 5.3.3 Voltage Imbalance Compensation

To test the proposed control functionalities, a grid imbalance is emulated by adding an inductive impedance of $R_U = 0.2\Omega$ and $L_U = 2.7mH$ in series to phase C of the S-STATCOM power circuit in Figure 5.13, as shown in Figure 5.16. The analysis will be simpler than in the first scenario and will focus on the effectiveness of the VIC when the S-STATCOM is operating at nominal capacity, which is when the voltage imbalance is more prominent. Synchronization process is omitted and simulation events are now as follows:

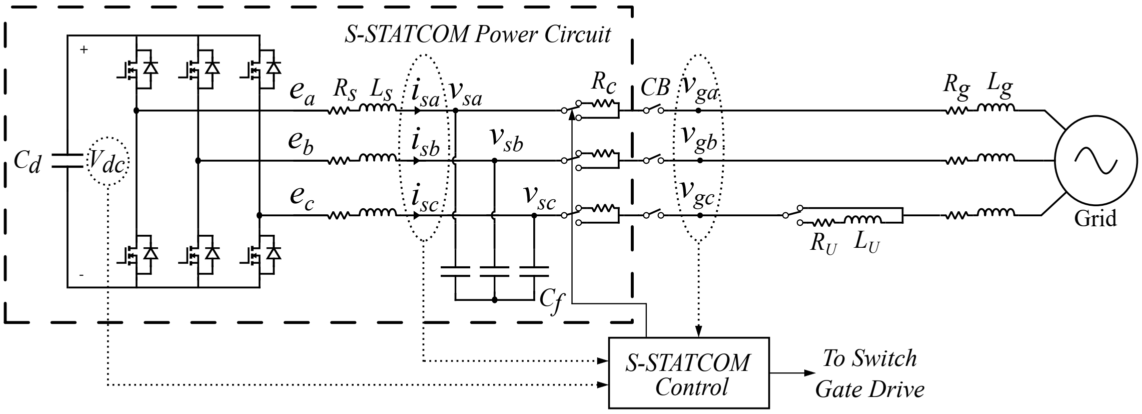

Figure 5.16: S-STATCOM power circuit with $Z_U$ added to phase C to create voltage imbalance

1) Reactive power order of $q^* = -1\ pu$ at $t = 1.0s$

2) Trigger voltage unbalance by adding $Z_U$ in series with phase C, at $t = 2.0s$

3) Activate VIC at $t = 3.0s$

4) Switch to V-mode with $V_g^* = 1.0\ pu$ at $t = 4.0s$

5) Switch to Droop-mode at $t = 6.0s$

6) Simulation ends at $t = 8.0s$

The PR controller gains for VICL are $K_p = 0.1$, $K_R = 100$ and $\omega_c = 0.01\omega_n = 3.77\ rad/s$. Figure 5.17 shows the effect of VIC activation on the grid voltages.

Before VIC activation, the voltage unbalance factor was around 8.2%, as shown in Figure 5.17b which is four times larger than the maximum 2% allowed [14, 58]. At $t = 1.5\ s$, VIC is activated and quickly reduced the unbalance factor to less than 0.1 %.

Figure 5.18 shows other quantities of interest during the events. After $t = 2.0s$, $2\omega$ oscillations can be seen clearly appearing in the DC bus voltage (Figure 5.18b), when the voltage imbalance is added, which is expected. They also appear in the frequency tracking signal (Figure 5.18a) and measured reactive power at the PCC (Figure 5.18d), however, it did not interfere significantly with the other modes of operation at any point. V-mode tracked the 1.0 pu voltage order as expected (Figure

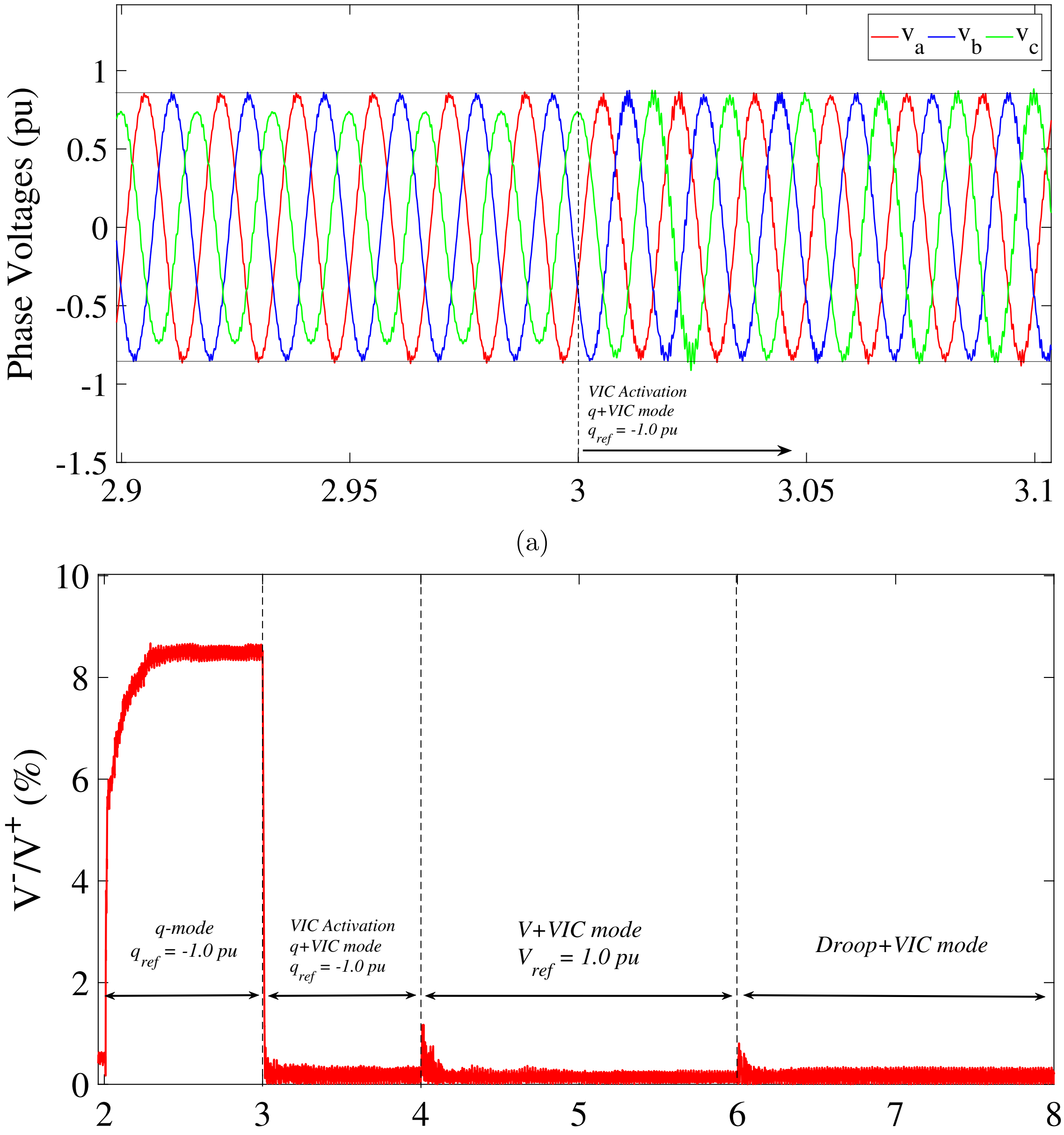

(a)

(b)

Figure 5.17: Simulation results for VIC-mode in Scenario 2. (a) Three-phase grid voltages (b) Voltage Unbalance Factor $V^-/V^+$ throughout the simulation.

5.18c) and droop verification with (2.12) resulted in $D_q = 10.07$, which is due to the slightly higher reactive power needed to supply the unbalanced grid.

Figure 5.19 shows the effect on the line currents when VIC is on. As in the previous large-scale scenario, current in the affected phase $i_c$ experienced the largest variation of 33% compared to its previous amplitude value when VIC was off. Current $i_b$ reached the largest amplitude value of 1.59 pu, but its previous condition of 1.41 pu would already trigger an overcurrent protection in such an extreme unbalanced condition. Nevertheless, the currents stayed within limits in all other modes of operation with VIC on.

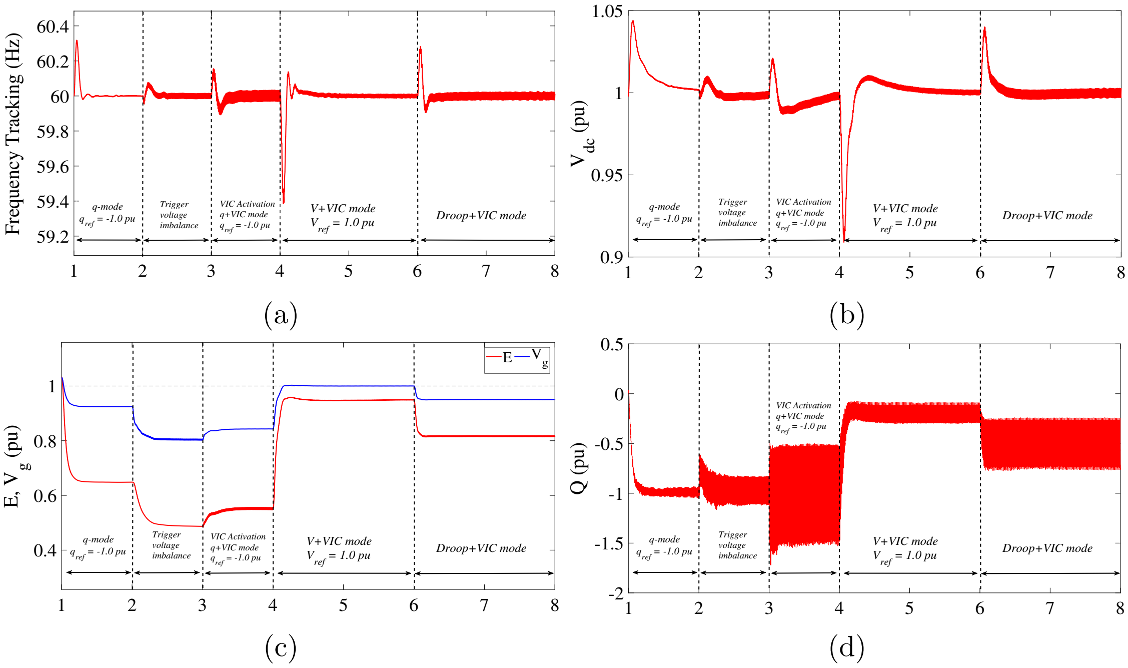

(a) (b)

(c) (d)

Figure 5.18: Results for Scenario 2 modes when VIC is on. a) Frequency tracking by CL1a; b) DC bus voltage; c) Internal and grid voltage amplitudes; d) Reactive power

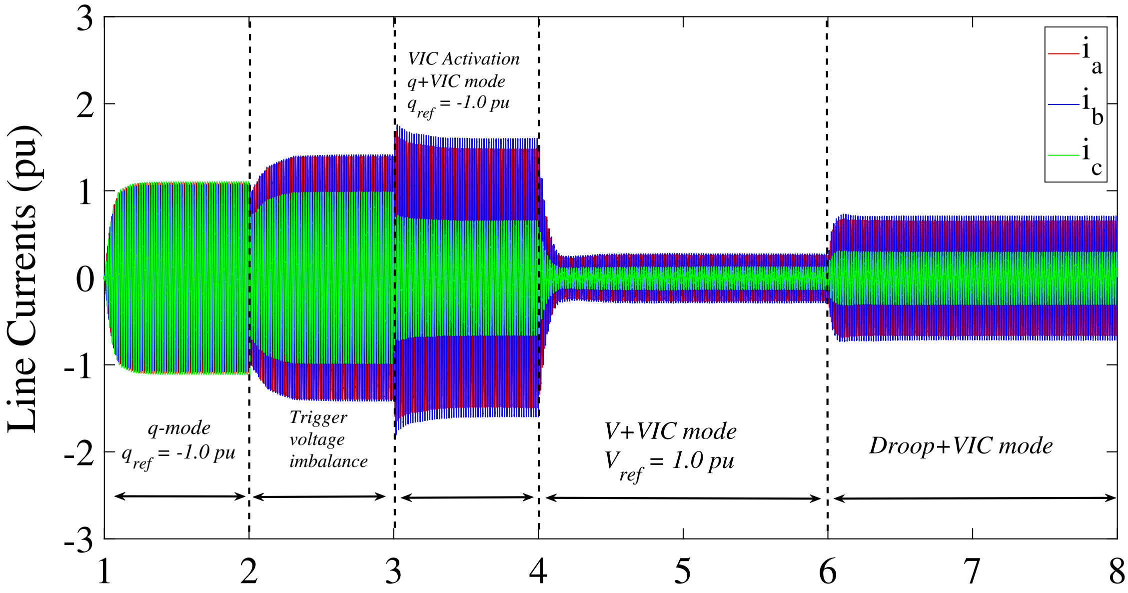

Figure 5.19: S-STATCOM line currents when VIC is activated

## 5.4 S-STATCOM Small-Scale Experimental Setup

To validate the simulation results and effectiveness of the control strategy, a small-scale prototype is built based on Figure 5.13. In addition to the depicted components, it also needs voltage and current sensors, gate drivers and a DSP with an I/O interface, which will host all controls necessary for the prototype to work properly.

Two reasonable priced Texas Instruments devices were used in this project. First one is a development kit called *LaunchPad* model LaunchXL-F28377S with an embedded C2000 series DSP TMS320F28377S (Figure 5.20). It has a 200 MHz internal frequency, 1 Mb Flash memory, 164 kb of RAM, 24 ADC channels to collect external data and 24 PWM channels for implementation of gate switching logic. The *LaunchPad* has an USB interface for communication with the PC and exposed pins for easy access to most of the DSP's terminals, which are also fully compatible with the next device.

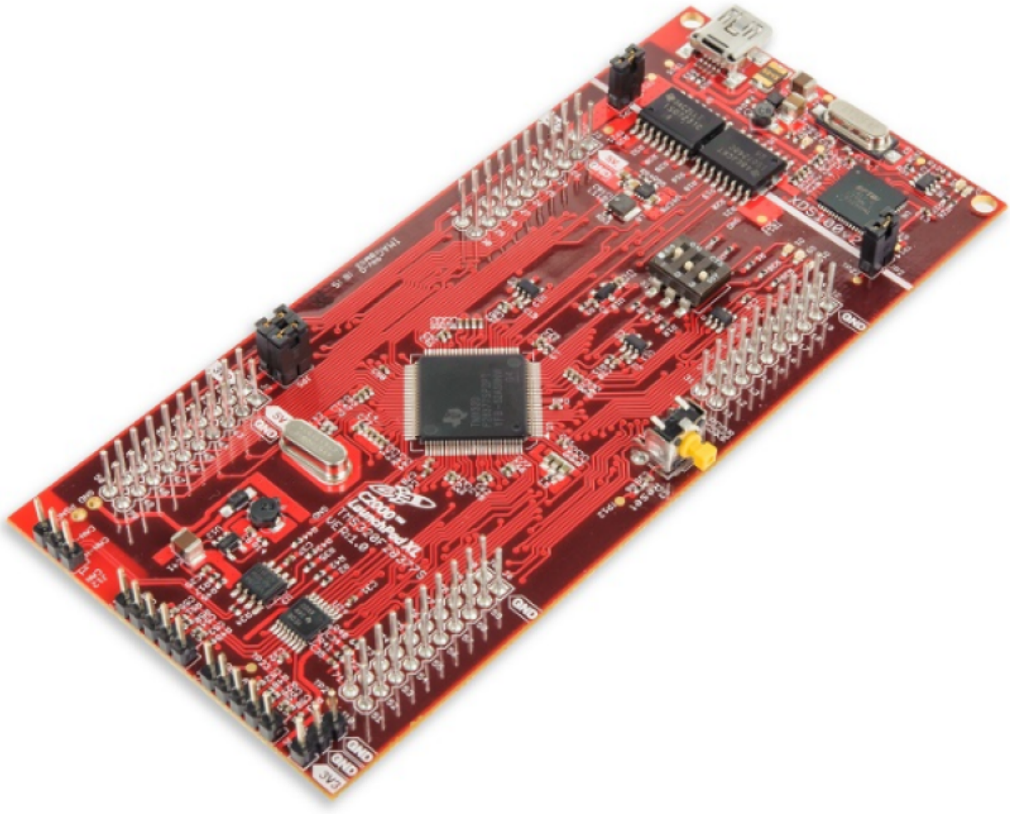

Figure 5.20: Texas Instruments development kit LaunchXL-F28377S, now discontinued

Second one is the BOOSTXL-DRV8305EVM BoosterPack add-on (Figure 5.21), which is a three-phase inverter aimed for driving brushless DC motors that is fully compatible with the LaunchXL-F28377S. It is made of three half-bridges with 2 MOSFETS each, with a maximum switching frequency of 200 kHz. It has current and voltage sensors for the three phases and one for the DC side, each with a range of 15 A RMS and 45V respectively. In addition, it has several embedded protections on its drive stage, e.g short circuit and thermal. Its small and compact structure fits over the upper portion of the LaunchPad and connects to it through the pins, where all control signals are sent and received to ensure proper operation. Both devices cover the converter part, control logic, communication with PC and sensor data processing.

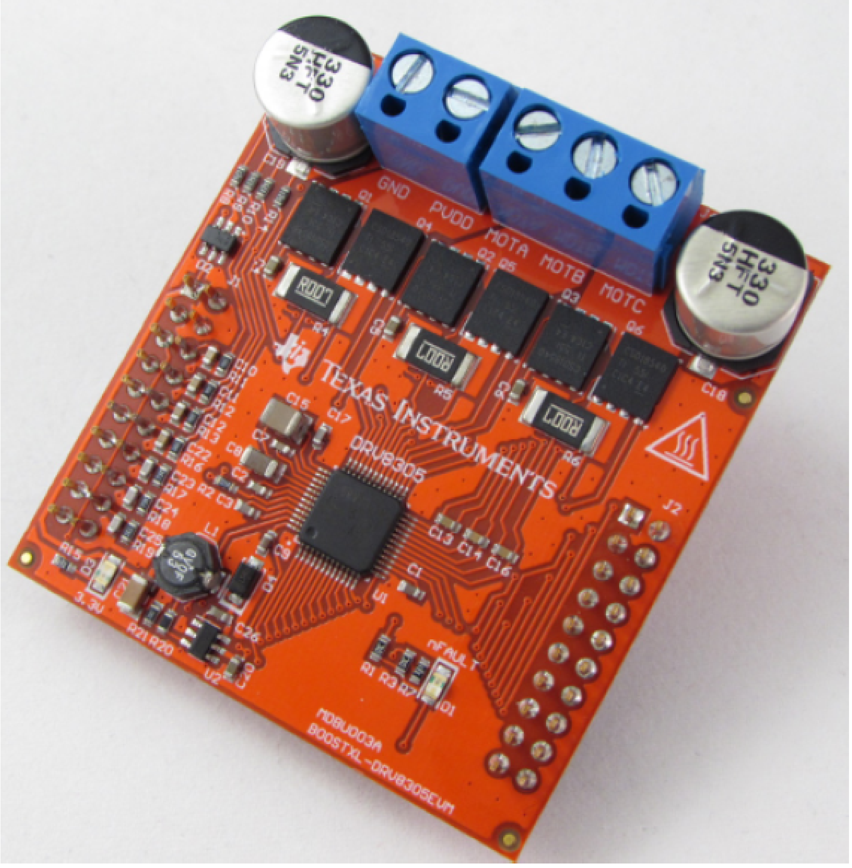

Figure 5.21: BoosterPack BOOSTXL-DRV8305EVM add-on for the LauchPad

Extra devices needed for the prototype are an external sensor to measure voltage at the PCC and a startup circuit to disconnect the pre-charge resistors on command. Figure (5.22) shows the complete system.

In it one can view all the peripherals connected, forming the complete experimental setup. The LC filter for each phase in the center of the figure connects the DSP + BoosterPack assembly to the startup circuit. This in turn connects to the step-up transformer and the voltage measurement circuit through a circuit breaker and a second set of inductors representing $Z_g'$, which were used to emulate a weak

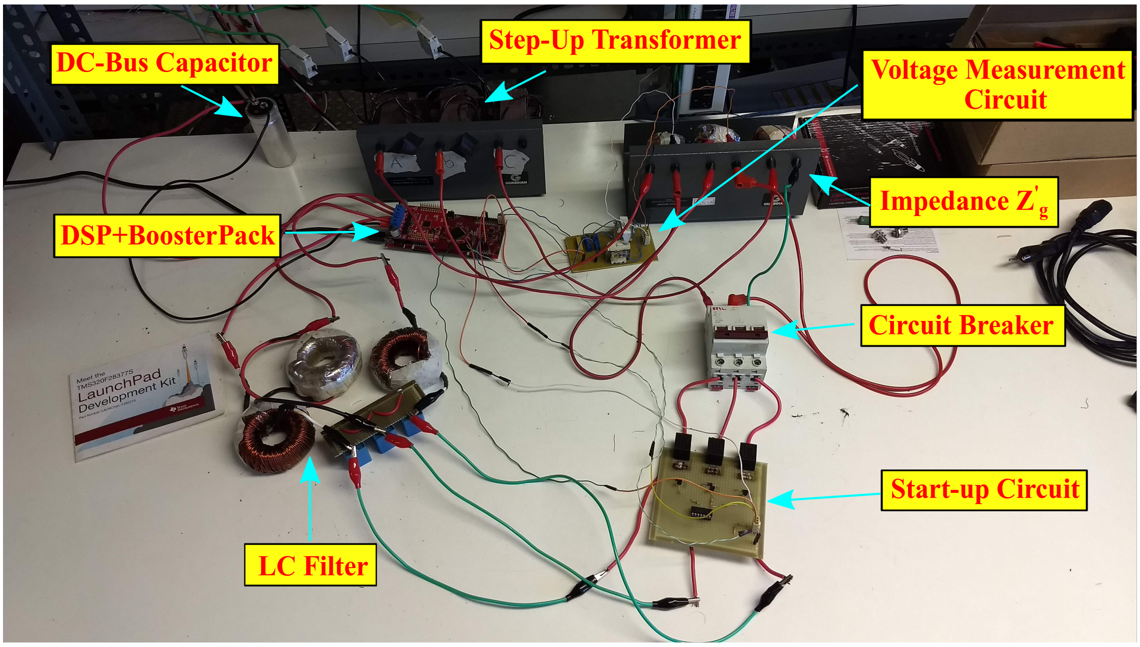

Figure 5.22: S-STATCOM experimental prototype

grid at that point of connection, providing a more inductive characteristic to a network that is predominantly resistive. Therefore, the point of connection with the grid should be understood as the terminals of these inductors from now on. To the left of the transformer, is the 6.5 $mF$ capacitor connected to the BoosterPack, which has two capacitors of 0.33 $mF$ connected in parallel on its DC bus, summing up to 7.16 $mF$.

The steps involved in the realization of the small-scale prototype, in addition to the simulation, are: construction of the external voltage sensor, system boot circuit construction and operation, C code creation for the DSP and sensor calibration. Aside from the first one, each of those steps are well explained in [75] and will be briefly reproduced here to outline the main characteristics of this project.

### 5.4.1 Voltage measuring circuit

The voltage measuring circuit is designed to condition the read signal to the limits of the DSP analog-to-digital converter (ADC), which only recognizes voltage levels from 0 to 3V. It consists of two 15:1 single-phase, open-delta connected transformers on both the high and low side. On the low side, the common point of the open delta connection was connected to the tap of a variable resistor of the type trimpot, which in turn was connected between the 3.3 V level and the ground of the DSP, forming a voltage divider, as shown in Figure 5.23.

This scheme adds a DC offset to the sinusoids, placing them within the range of positive voltage values required by the ADC. Another two trimpots were used to adjust the amplitude of the resulting sinusoids so that they did not exceed the read

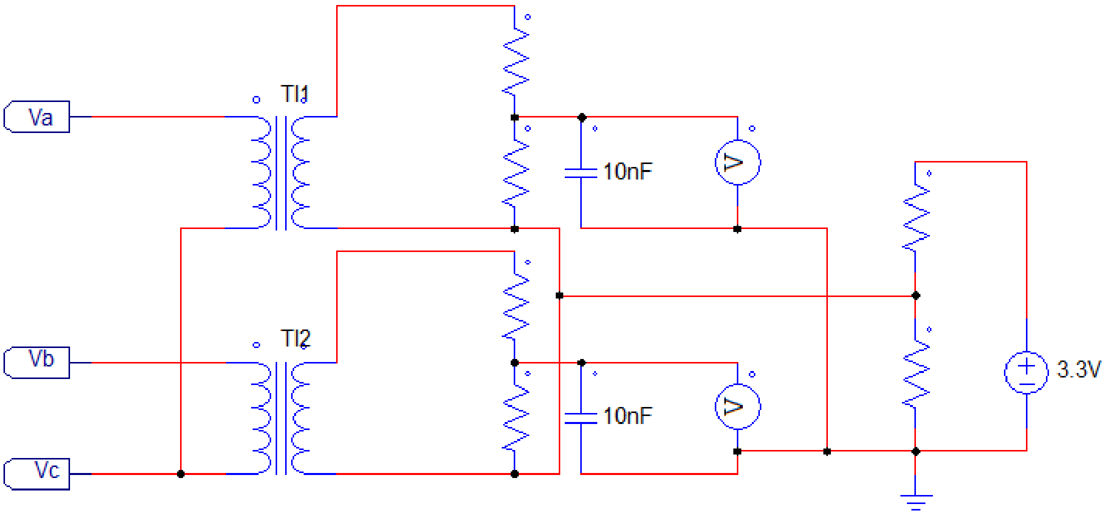

Figure 5.23: Voltage sensor used in the experimental small-scale prototype

limit values of the ADC. The conditioned signals in Figure 5.23 represent two line voltages of the network, $v_{bc}$ and $v_{ac}$. However, the control requires measurements of the three phase voltages to function correctly. Therefore, a mathematical manipulation is made to extract the three phase voltages from these two line voltage values by assuming that there is no zero sequence component circulating in the converter, which is reasonable since the whole system is 3-wire. From such conditions, it can be stated that

$$v_a + v_b + v_c = 0, \tag{5.7}$$

$$v_{ab} + v_{bc} + v_{ca} = 0. \tag{5.8}$$

Next, a relationship between phase voltage $v_c$ and the measured line voltages can be drawn, since it is a common voltage for both measurements. This yields

$$v_{bc} + v_{ac} = v_a + v_b - 2v_c. \tag{5.9}$$

From (5.7), $v_c = -(v_a + v_b)$ and then (5.9) becomes

$$v_c = -\frac{1}{3}(v_{bc} + v_{ac}). \tag{5.10}$$

By manipulating (5.7), (5.8) and (5.10), the following set of equations describing the system phase voltages is obtained

$$\begin{cases} v_a = \frac{1}{3}(2v_{ac} - v_{bc}), \\ v_b = \frac{1}{3}(2v_{bc} - v_{ac}), \\ v_c = -\frac{1}{3}(v_{ac} + v_{bc}). \end{cases} \tag{5.11}$$

### 5.4.2 Startup Sequence

For the S-STATCOM implementation on a small-scale experimental setup, a complete startup sequence is developed to safely initialize the system. Consider the S-STATCOM power circuit shown in Figure 5.13, where $R_C$ are the pre-charge resistors connected through relay controlled switches, $\mathbf{v}_g$ is the grid voltage, $\mathbf{v}_s$ is the S-STATCOM terminal voltages and $C_d$ is the DC bus capacitor. The S-STATCOM is powered down, i.e., $V_{dc} = 0$, the three-phase bridge's switches are off and the pre-charge resistors are connected. The startup sequence then goes as follows:

1) The CB is manually closed and $C_d$ is pre-charged through $R_C$ to avoid high current surges. In a practical implementation, this would also power up the sensors and control circuits, if they are not fed through an external source.

2) S-STATCOM control initializes the synchronization algorithm [64].

3) Once synchronization is achieved, i.e. when (4.8) is satisfied, the S-STATCOM is ready to enter in one of its modes of operation.

4) When activating one of the modes, four actions occur simultaneously: activation of the converter switches, bypass of pre-charge resistors, activation of the DC bus voltage control and deactivation of the synchronization algorithm

5) After the DC voltage regulation transient, the S-STATCOM will be fully operational in the chosen mode.

In the initialization circuit, two resistors of 10 Ω in parallel per phase were used to represent $R_C$ to limit the startup currents. Details of its construction and operation are well developed in [75].

### 5.4.3 DSP code implementation

The code was written in the *Code Composer* software from the *MonoMtrServo_-377s_v1* sample project available in the *Control Suite* extension. This approach allows one to take advantage of the boot and protection routines of the DSP and BoosterPack that are already set up. All control code was discretized as explained in Section 5.1.2. To implement the discrete transfer functions in C code, required for programming the DSP, they should be rearranged in the form:

$$H(z) = \frac{U(z)}{E(z)} = \frac{b_0 + b_1 z^{-1} + \dots + b_{m-1} z^{m-1} + b_m z^m}{1 + a_1 z^{-1} + \dots + a_{n-1} z^{n-1} + a_n z^n}, \tag{5.12}$$

and then apply the time delay theorem [66], which means that:

$$U(z)z^{-1} = u[(k-1)T_s]. \tag{5.13}$$

Therefore, the resulting equation is:

$$\begin{split} u(kT_s) = b_0 e(kT_s) + b_1 e[(k-1)T_s] + \dots + b_{m-1} e[(k-(m-1))T_s] + b_m e[(k-m)T_s] + \\ \dots - a_1 u[(k-1)T_s] - \dots - a_{n-1} u[(k-(n-1))T_s] - a_n u[(k-n)T_s], \end{split} \tag{5.14}$$

which represents the transfer function output at the current time step in function of the input and output values in previous time steps. This can be implemented in C code with vectors to store the values of previous time steps. Other project details such as sensor calibration are well developed in [75].

### 5.4.4 Experimental Results

Experiments with the small-scale prototype are carried out the same way simulations do, as shown in the previous section. Results were collected with a RIGOL DS1064B oscilloscope with phase voltage and line current measurements at the PCC. The startup sequence is started as described in Section 5.4.2, with the DC bus capacitor pre-charge. Figure 5.24 shows the three-phase currents during the instant of turning on the circuit-breaker that connects the system to the grid.

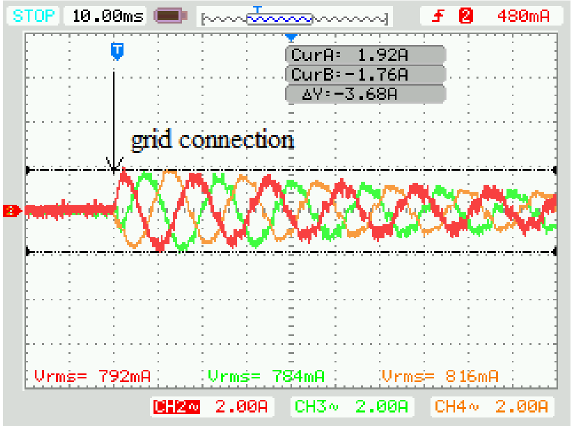

Figure 5.24: Three-phase currents at system startup i.e. DC bus capacitor pre-charge.

Note that the current amplitude does not exceed 2 A, which is less than 0.5 pu, resulting in a safe system start-up. Once initialized and synchronized, the S-STATCOM is then switched to q-mode with $q_{ref} = 0$. Although simulations indicate that transients from step 4) of the startup defined in Section 5.4.2 are safe, the DC bus voltage control was implemented with a ramp of 1.5 s in its reference value as an extra precaution, which is shown in Figure 5.25.

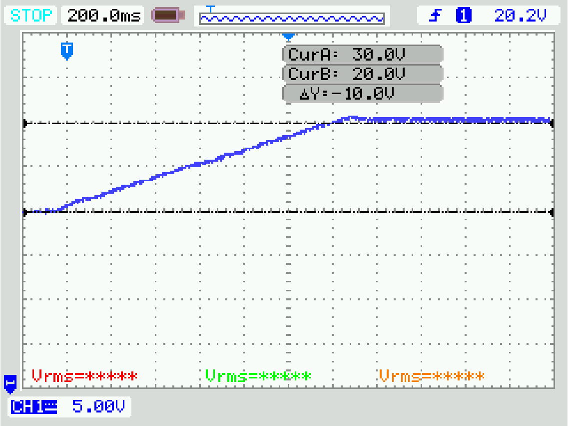

Figure 5.25: Step-up ramp on the DC bus voltage reference.

Once the DC bus reference voltage has been reached, the system is stable only by absorbing active power to maintain it and is in Q-mode ready to receive a reactive power command. Figure 5.26 shows the DC bus voltage and line current transients after a -1 pu reactive power order. The command is answered quickly by the prototype and the DC bus voltage transients closely follow the simulations.

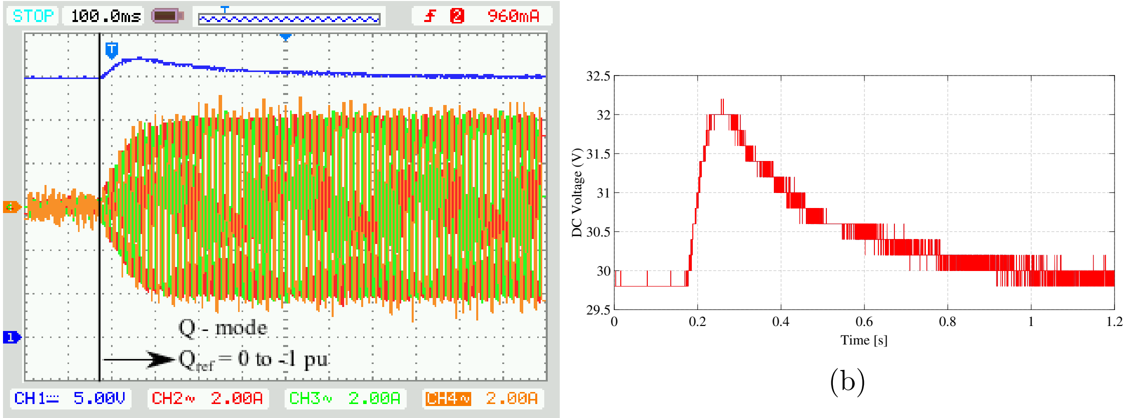

(b)

(a)

Figure 5.26: DC Voltage and line current transients for a -1 pu Reactive power order. (a) $V_{dc}$ (blue) and $i_{abc}$ on the oscilloscope screen. (b) $V_{dc}$ signal acquired from the oscilloscope.

Since the whole system is 3-wire, verification of the reactive power is done with measurements of two phase voltages and two line currents acquired from the oscilloscope, as shown in Figure 5.27a. The three-phase reactive power is then calculated by the mean value of the signal resulting from (5.15). The obtained value was -79.82 VAr.

$$Q = \frac{1}{\sqrt{3}}((v_b - v_c)i_a + (v_c - v_a)i_b + (v_a - v_b)i_c) \tag{5.15}$$

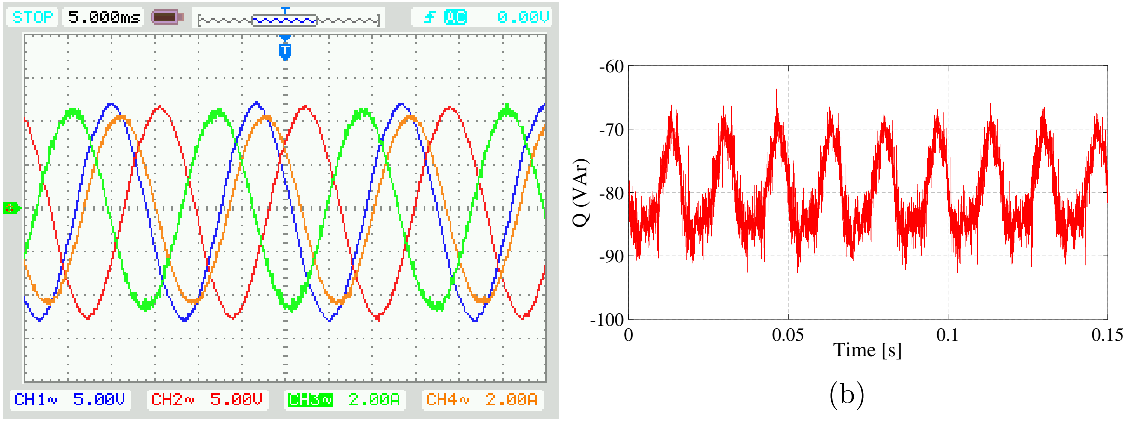

(b)

(a)

Figure 5.27: (a) Phase voltages A and B (blue and red) and line currents A and B (green and orange) for the S-STATCOM experimental setup in q-mode @ $q_{ref} = -1pu$; (b) Calculated reactive power signal in q-mode with an average value of -79.82 VAr

The next event is switching to V-mode. Figure 5.28a shows the dynamics of the DC bus voltage and line currents after the transition from Q-mode with $Q_{ref} = -1\ pu$ to V-mode with $V_{ref} = 1.0\ pu$. Since voltage at the PCC was higher than 1.0 pu before the S-STATCOM's connection, it kept absorbing reactive power just enough to fulfill the control setpoint, as predicted by simulations. Figure 5.28b shows the regulated three-phase voltages with an amplitude of 13.17 V, approximately 0.996 pu.

On switching to Droop mode, the system is expected to reach a setpoint that agrees with (5.6), where $\Delta Q$ is the change in reactive power between modes Q and Droop and $\Delta V$ is the change in the PCC voltage between modes V and Droop. Figure 5.29 shows the results for the Droop mode on the small scale prototype. The DC bus voltage and current dynamics are in accordance with the simulation. Reactive power and voltage amplitude at the PCC are -48.69 var and 12.67 V respectively, resulting in a droop coefficient of 10.38.

Some results show a slight imbalance due to a mismatch between the Zg' inductors, which is also perceived in the calculation of power waveforms. However, it was not enough to disrupt the control at any point during its evaluation, even in initial the synchronization with grid, as it can be seen in the results above. This characteristic of the setup was even one of the motivating factors for pursing an imbalance compensator add-on to the basic synchronverter control.

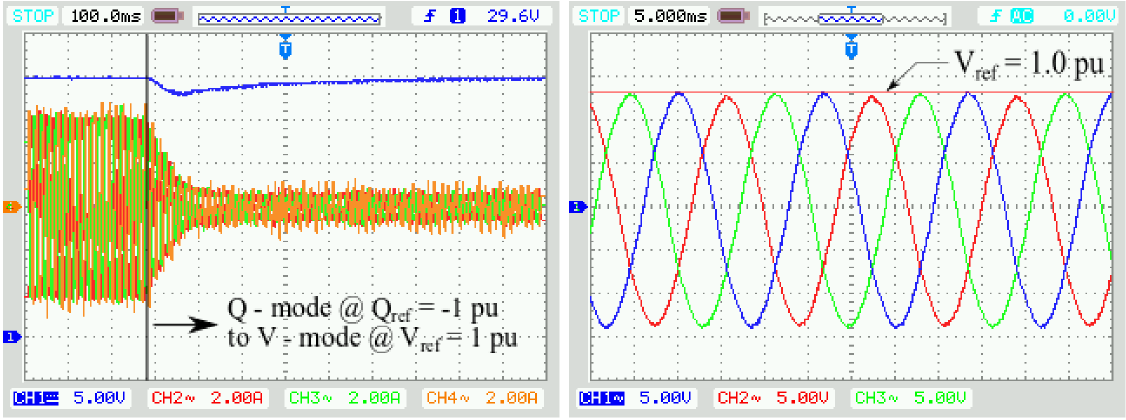

(a) (b)

Figure 5.28: V-mode measurements data, with $V_{ref} = 1.0pu$. (a) $V_{dc}$ and $i_{abc}$ transients when switching from Q to V-mode. (b) Three-phase voltages at V-mode on steady-state.

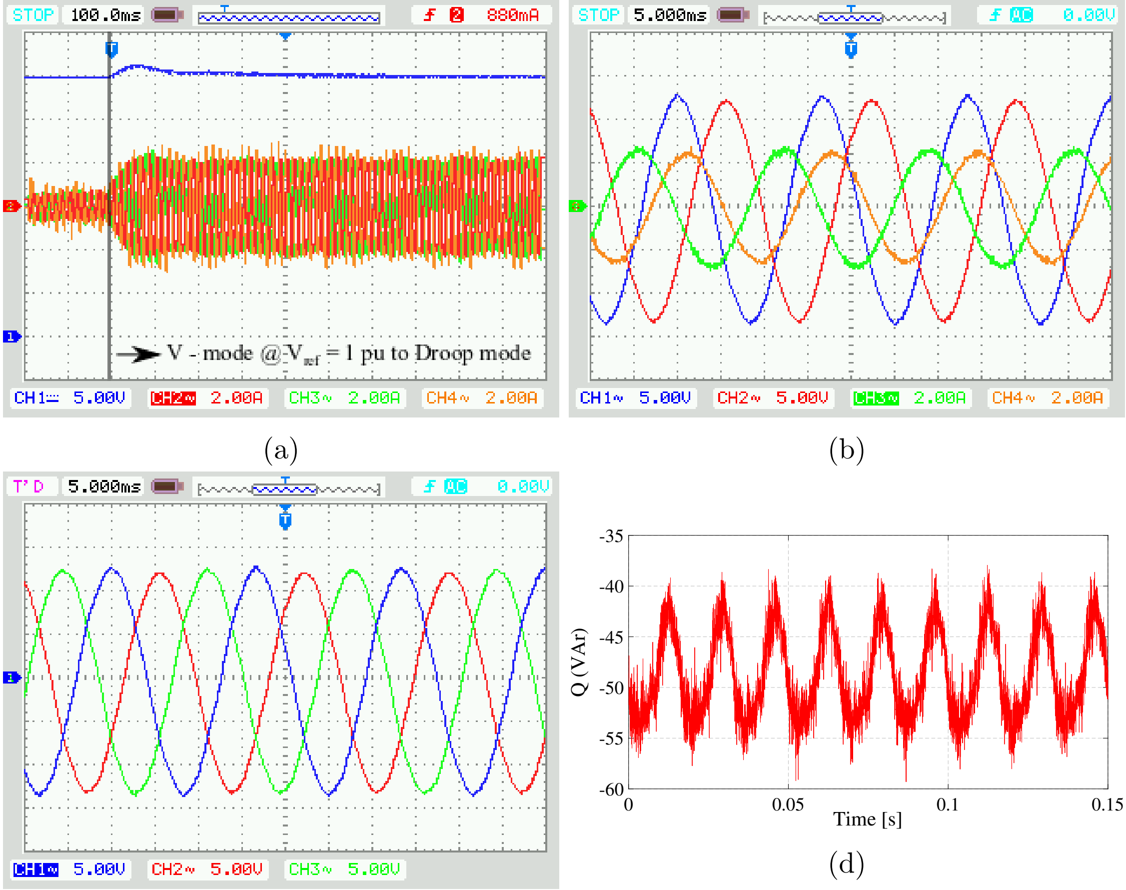

(a) (b)

(c) (d)

Figure 5.29: Droop-mode measurements. (a) $V_{dc}$ and $I_{abc}$ transients when switching from V to Droop-mode. (b) Phase voltages A and B (blue and red) and line currents A and B (green and orange). (c) Three-phase voltages at Droop-mode on steady-state. (d) Calculated reactive power signal in Droop-mode with an average value of -48.69 VAr

### 5.4.5 Voltage Imbalance Compensation

At the small-scale prototype, the creation of an unbalanced grid was done the same way as in the simulations, by adding an inductive impedance of $R_U = 0.2\Omega$ and $L_U = 2.7mH$ in series with $Z_g$ on phase C. Moreover, the PR controller gains on VICL are the same as in the simulations. The controller was analyzed with the S-STATCOM on Q-mode and a reactive power order of -0.8 pu to emulate the worst possible unbalanced conditions. The reactive power order could not be higher due to a limitation of the BoosterPack current sensors.

The initial condition of the system's voltages and currents in this scenario are shown in Figure 5.30, which agrees with the simulations (Figures 5.17a and 5.19). The calculated voltage unbalance factor is 10.33%.

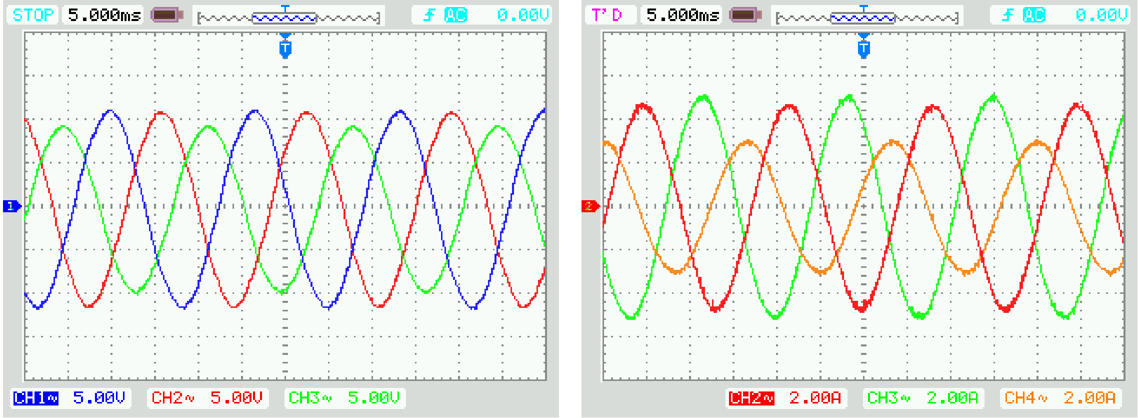

Figure 5.30: Initial unbalanced grid conditions. (a) Three-phase (phase-neutral) voltages: A in blue, B in red and C in green. (b) Three-phase (line) currents: A in red, B in green and C in orange.

Figure 5.31 shows the results of VIC activation on grid voltages. Transients are as fast as predicted in simulations and the new calculated voltage unbalance factor is 1.14%, ten times less than the initial condition. Line currents increased in the same manner predicted in simulations, with the affected phase current $i_c$ experiencing a 32% variation and $i_b$ reaching the highest amplitude of 1.55 pu.

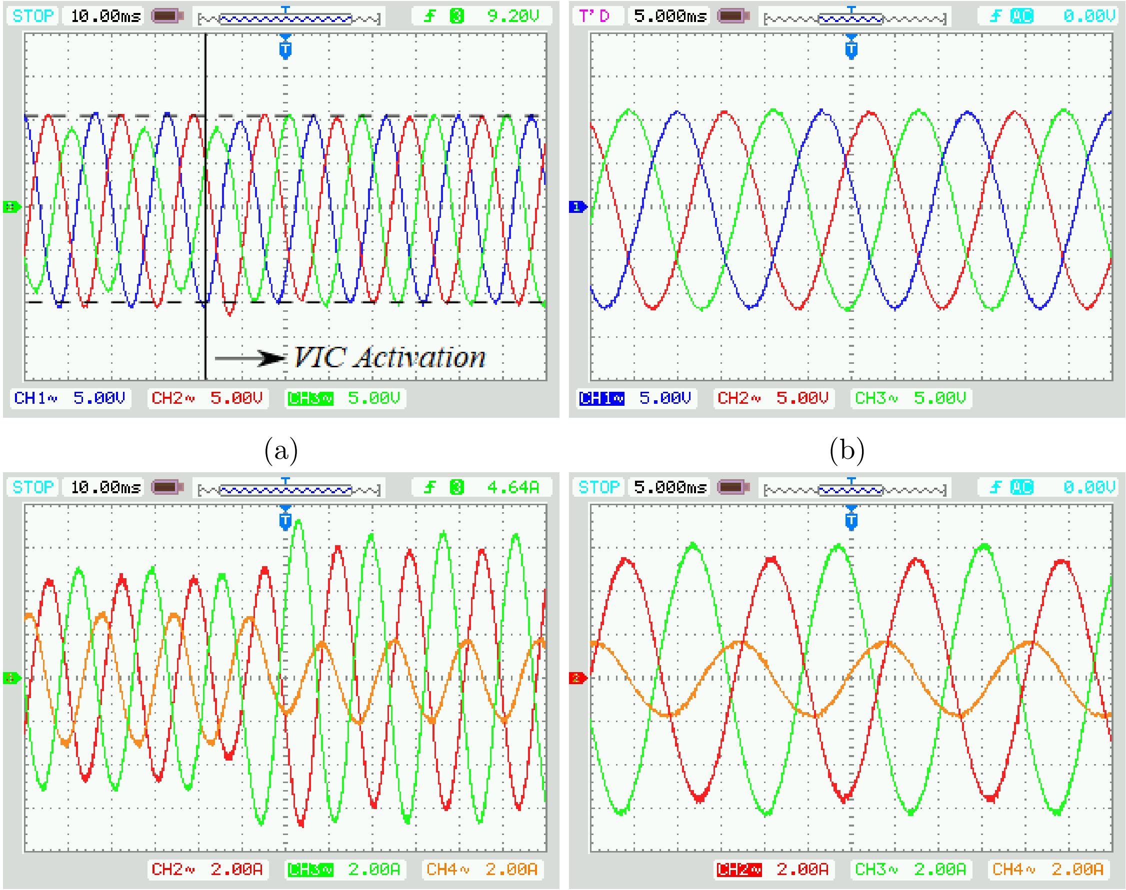

(a) (b)

(c) (d)

Figure 5.31: Measurements for VIC-mode. (a) VIC-mode activation transients of the three-phase voltages, (b) Three-phase voltages at steady-state with VIC-mode activated, (c) VIC-mode activation transients of the three line currents, (d) Three line currents at steady-state with VIC-mode activated.

## 5.5 Results discussion

In this chapter, two systems were simulated to evaluate the S-STATCOM's control performance in several modes of operation its. The first was a large-scale setup with a ±3 MVA system in a twin converter configuration, connected to a 25kV distribution grid equivalent circuit. The second was a small-scale 80 VA system with a single three-phase converter, intended as a validation step to the implementation of an experimental setup and lastly the experimental setup itself.

Both scenarios show that there is no limitation regarding converter topology and any PWM based strategy can be implemented to drive the converter, using the back-EMF signal $\mathbf{e}$ of the model as control signal. Parameter tuning of the DC bus voltage PI controller through the developed guidelines was effective, with DC bus voltage dynamic showing a well balanced compromise between settling time and overshoot. Also, the S-STATCOM control itself performed well in all scenarios and operation modes, reaching their designated set points with smooth dynamics and withstanding the transitions from balanced to unbalanced grid conditions.

When the S-STATCOM VIC-mode is on, it essentially acts as an active filter supplying oscillating power locally and compensating voltage imbalance at the PCC and buses upstream. Therefore, to generate the oscillating power with a balanced set of voltages, the negative sequence current component must increase, causing significant variations in the amplitude of each line current. Such effect is noticed in all scenarios and in the experimental setup, with an average of 30% variation in the amplitude of the current in the affected phase that originated the unbalanced condition. Current amplitudes reached as high as 60% above nominal capacity, which would certainly trigger overcurrent protection. However, even considering this situation a control limitation or design factor, it must be taken into account that it was observed under extreme steady-state operation conditions unlikely to occur in a real world scenario. In V and Droop modes with VIC activated, currents were well within range in both systems. Even with the highly unbalanced currents when VIC was on, the S-STATCOM modes were not significantly affected, mainly because of the filtering in $T_e$ and $q$ calculations, as well as in the voltage measurement signals by the DSOGI+PNSC structure.

# Chapter 6

# Conclusions and Future Work

In this thesis, a synchronverter based STATCOM control was developed with voltage imbalance compensation capabilities to be used in distribution and micro-grids. A synchronous machine model is developed in space vector representation to serve as basis of the main model, due to its simplicity of implementation, reduced computational effort and easier compatibility with resonant controllers. The Voltage Imbalance Control Loop takes advantage of this feature by utilizing a DSOGI tuned by the active power loop to detect the negative sequence voltage of the grid and compensate it through PR controllers.

In addition to the standard modes of operation of a STATCOM, the proposed solution is also capable of synchronizing with the grid without PLL of FLL circuits. A small-signal model is developed to better understand the system dynamic behavior and tune its parameters. Simulations in large and small scale were conducted to evaluate the control performance in each mode of operation. In both scenarios, the control performed well and reached all of its designated set points, showing that it is capable of performing the tasks of a regular D-STATCOM. The voltage imbalance compensation capabilities makes the S-STATCOM perform as an active filter, locally supplying the oscillating power required by the source of imbalance and fully compensating the voltage imbalance at the PCC and upstream, which is clearly seen in the large scale simulation.

The S-STATCOM manages to compensate the voltage imbalance in all scenarios, at the cost of highly unbalanced line currents with amplitudes reaching as high as 1.6 pu under extreme conditions. However, they did not interfere significantly in the control modes due to filtering of the S-STATCOM voltage and power signals.

An experimental prototype based in the small scale simulations was also built to validate the control and it performed as expected, following its designated control references with dynamics close to the ones observed in simulations. Although the S-STATCOM showed excellent performance compensating voltage imbalance, the highly unbalanced currents are a limitation for its deployment in the field, which requires higher converter ratings then the nominal capacity of the system, along with additional overcurrent protection.

## Suggestions for future work

- Evaluate the S-STATCOM performance on grid disturbances (faults, load shedding, voltage flickering, etc);
- Oscillating power-flow analysis and oscillating power sharing at fundamental frequency;
- Include converter safety measures, i.e peak current limitation;
- Evaluate reactive power sharing through voltage droop control with several units (S-STATCOM or other systems with voltage droop control).

# Bibliography

[1] BEVRANI, H., ISE, T., MIURA, Y. "Virtual synchronous generators: A survey and new perspectives", *International Journal of Electrical Power Energy Systems*, v. 54, pp. 244 – 254, 2014. ISSN: 0142-0615. doi: https://doi.org/10.1016/j.ijepes.2013.07.009. Disponível em: <`http://www.sciencedirect.com/science/article/pii/S0142061513003062`>.

[2] ZHONG, Q. C., WEISS, G. "Synchronverters: Inverters That Mimic Synchronous Generators", *IEEE Transactions on Industrial Electronics*, v. 58, n. 4, pp. 1259–1267, April 2011. ISSN: 0278-0046. doi: 10.1109/TIE.2010.2048839.

[3] NGUYEN, P.-L., ZHONG, Q. C., BLAABJERG, F., et al. "Synchronverter-based operation of STATCOM to Mimic Synchronous Condensers". In: *2012 7th IEEE Conference on Industrial Electronics and Applications (ICIEA)*, pp. 942–947, July 2012. doi: 10.1109/ICIEA.2012.6360859.

[4] VAN EMMERIK, E. L., FRANÇA, B. W., AREDES, M. "A synchronverter to damp electromechanical oscillations in the Brazilian transmission grid". In: *2015 IEEE 24th International Symposium on Industrial Electronics (ISIE)*, pp. 221–226, June 2015. doi: 10.1109/ISIE.2015.7281472.

[5] VAN EMMERIK, E. L. *Synchronverter Applied to Power Systems.* Tese de D.Sc., COPPE/UFRJ, Rio de Janeiro, RJ, Brasil, 2018.

[6] DOS SANTOS, C. F., GRIGOLETTO, F. B., STEFANELLO, M. "Power quality improvement in a grid connected voltage source inverter using the concept of virtual synchronous machine". In: *2015 IEEE 13th Brazilian Power Electronics Conference and 1st Southern Power Electronics Conference (COBEP/SPEC)*, pp. 1–5, Nov 2015. doi: 10.1109/COBEP.2015.7420075.

[7] CAICEDO, J., DE CASTRO, A. R., FRANÇA, B., et al. "Resonant harmonic compensation for synchronverter, integrating wind and photovoltaic power generation into an electrical grid, case study: Nonlinear and

unbalanced load", *14th Brazilian Power Electronics Conference, COBEP 2017*, v. 2018-Janua, pp. 1–6, 2017. doi: 10.1109/COBEP.2017.8257275.

[8] TEODORESCU, R., LISERRE, M., RODRIGUEZ, P. *Grid converters for photovoltaic and wind power systems*, v. 29. John Wiley & Sons, 2011.

[9] RODRÍGUEZ, P., LUNA, A., MUÑOZ-AGUILAR, R. S., et al. "A stationary reference frame grid synchronization system for three-phase grid-connected power converters under adverse grid conditions", *IEEE Transactions on Power Electronics*, v. 27, n. 1, pp. 99–112, 2012. ISSN: 08858993. doi: 10.1109/TPEL.2011.2159242.

[10] GIROUX, P., SYBILLE, G. "Modeling and Simulation of a Distribution STATCOM using Sirnulink's Power System Blockset", v. 00, n. C, pp. 990–994, 2001.

[11] J. M. CARRASCO, MEMBER, IEEE, L. G. FRANQUELO, FELLOW, IEEE, J.T.BIALASIEWICZ, S. M., IEEE, E. GALVAN, MEMBER, IEEE, R. PORTILLO, M. M. PRATS, MEMBER, IEEE, J. I. LEÓN STUDENT MEMBER, IEEE, MORENO., N. "Power Electronic Systems for the Grid Integration of Renewable Energy Sources: a Survey", *Advances in Intelligent Systems and Computing*, v. 673, pp. 37–46, 2006. ISSN: 21945357. doi: 10.1007/978-981-10-7245-1_5.

[12] TIELENS, P., VAN HERTEM, D. "The relevance of inertia in power systems", *Renewable and Sustainable Energy Reviews*, v. 55, pp. 999–1009, 2016. ISSN: 18790690. doi: 10.1016/j.rser.2015.11.016. Disponível em: <`http://dx.doi.org/10.1016/j.rser.2015.11.016`>.

[13] OLIVARES, D. E., MEHRIZI-SANI, A., ETEMADI, A. H., et al. "Trends in microgrid control", *IEEE Transactions on Smart Grid*, v. 5, n. 4, pp. 1905–1919, 2014. ISSN: 19493053. doi: 10.1109/TSG.2013.2295514.

[14] VON JOUANNE, A., BANERJEE, B. "Assessment of voltage unbalance", *IEEE Transactions on Power Delivery*, v. 16, n. 4, pp. 782–790, Oct 2001. ISSN: 0885-8977. doi: 10.1109/61.956770.

[15] BASAK, P., CHOWDHURY, S., HALDER NEE DEY, S., et al. "A literature review on integration of distributed energy resources in the perspective of control, protection and stability of microgrid", *Renewable and Sustainable Energy Reviews*, v. 16, n. 8, pp. 5545–5556, 2012. ISSN: 13640321. doi: 10.1016/j.rser.2012.05.043. Disponível em: <`http://dx.doi.org/10.1016/j.rser.2012.05.043`>.

[16] SINGH, B. "Static synchronous compensators (STATCOM): a review", *IET Power Electronics*, v. 2, pp. 297–324(27), July 2009. ISSN: 1755-4535. Disponível em: <`http://digital-library.theiet.org/content/journals/10.1049/iet-pel.2008.0034`>.

[17] TELEKE, S., ABDULAHOVIC, T., THIRINGER, T., et al. "Dynamic performance comparison of synchronous condenser and SVC", *IEEE Transactions on Power Delivery*, v. 23, n. 3, pp. 1606–1612, 2008. ISSN: 08858977. doi: 10.1109/TPWRD.2007.916109.

[18] MAJUMDER, R., GHOSH, A., LEDWICH, G., et al. "Power sharing and stability enhancement of an autonomous microgrid with inertial and non-inertial DGs with DSTATCOM", *2009 International Conference on Power Systems, ICPS '09*, pp. 1–6, 2009. doi: 10.1109/ICPWS.2009.5442666.

[19] LEE, G. M., LEE, D. C., SEOK, J. K. "Control of Series Active Power Filters Compensating for Source Voltage Unbalance and Current Harmonics", *IEEE Transactions on Industrial Electronics*, v. 51, n. 1, pp. 132–139, 2004. ISSN: 02780046. doi: 10.1109/TIE.2003.822040.

[20] GHOSH, A., LEDWICH, G. "A unified power quality conditioner (UPQC) for simultaneous voltage and current compensation", *Electric Power Systems Research*, v. 59, n. 1, pp. 55–63, 2001. ISSN: 03787796. doi: 10.1016/S0378-7796(01)00141-9.

[21] OE, S. P., CHRISTOPHER, E., SUMNER, M., et al. "Microgrid unbalance compensator - Mitigating the negative effects of unbalanced microgrid operation", *2013 4th IEEE/PES Innovative Smart Grid Technologies Europe, ISGT Europe 2013*, pp. 1–5, 2013. ISSN: 0885-8977. doi: 10.1109/ISGTEurope.2013.6695388.

[22] SAVAGHEBI, M., JALILIAN, A., VASQUEZ, J. C., et al. "Autonomous voltage unbalance compensation in an islanded droop-controlled microgrid", *IEEE Transactions on Industrial Electronics*, v. 60, n. 4, pp. 1390–1402, 2013. ISSN: 02780046. doi: 10.1109/TIE.2012.2185914.

[23] M. SAVAGHEBI, A. JALILIAN, J. C. V., GUERRERO, J. M. "Secondary Control Scheme for Voltage Unbalance Compensation in an Islanded", *IEEE Transactions on Smart Grid*, v. 3, n. 2, pp. 1–12, 2012. ISSN: 1553-572X. doi: 10.1109/IECON.2011.6119815.

[24] ZHONG, Q.-C., WEISS, G. “Static synchronous generators for distributed generation and renewable energy”. In: *Power Systems Conference and Exposition, 2009. PSCE'09. IEEE/PES*, pp. 1–6. IEEE, 2009.

[25] KONG, X., PAN, J., GONG, X., et al. “Emulating the features of conventional generator with virtual synchronous generator technology: an overview”, *The Journal of Engineering*, v. 2017, n. 13, pp. 2135–2139, 2017. ISSN: 2051-3305. doi: 10.1049/joe.2017.0707.

[26] CHEN, Y., HESSE, R., TURSCHNER, D., et al. “Improving the grid power quality using virtual synchronous machines”, *International Conference on Power Engineering, Energy and Electrical Drives*, , n. May, pp. 1–6, 2011. ISSN: 21555516. doi: 10.1109/PowerEng.2011.6036498.

[27] SAKIMOTO, K., MIURA, Y., ISE, T. “Stabilization of a power system including inverter-type distributed generators by a virtual synchronous generator”, *Electrical Engineering in Japan (English translation of Denki Gakkai Ronbunshi)*, v. 187, n. 3, pp. 7–17, 2014. ISSN: 04247760. doi: 10.1002/eej.22426.

[28] FRANÇA, B. W., DE CASTRO, A. R., AREDES, M. “Wind and photovoltaic power generation integrated to power grid through dc link and synchronverter”. In: *2015 IEEE 13th Brazilian Power Electronics Conference and 1st Southern Power Electronics Conference (COBEP/SPEC)*, pp. 1–6, Nov 2015. doi: 10.1109/COBEP.2015.7420216.

[29] ZHENG, T. “Control strategy for suppressing power oscillation of virtual synchronous generator under unbalanced grid voltage”, *IET Conference Proceedings*, pp. 5 .–5 .(1), January 2015. Disponível em: <`http://digital-library.theiet.org/content/conferences/10.1049/cp.2015.0313`>.

[30] WANG, J., LUO, F., GU, B., et al. “Improved control strategies for three-phase four-leg virtual synchronous generator with unbalanced loads”, *2017 19th European Conference on Power Electronics and Applications, EPE 2017 ECCE Europe*, v. 2017-Janua, pp. 1–10, 2017. ISSN: 10006753. doi: 10.23919/EPE17ECCEEurope.2017.8099135.

[31] ZHENG, T., CHEN, L., GUO, Y., et al. “Flexible unbalanced control with peak current limitation for virtual synchronous generator under voltage sags”, *Journal of Modern Power Systems and Clean Energy*, v. 6, n. 1, pp. 61–72, Jan 2018. ISSN: 2196-5420. doi: 10.1007/s40565-017-0295-y. Disponível em: <`https://doi.org/10.1007/s40565-017-0295-y`>.

[32] ZHONG, Q., BOROYEVICH, D. "A droop controller is intrinsically a phase-locked loop". In: *IECON 2013 - 39th Annual Conference of the IEEE Industrial Electronics Society*, pp. 5916–5921, Nov 2013. doi: 10.1109/IECON.2013.6700105.

[33] ZHENG, T. "Comprehensive control strategy of virtual synchronous generator under unbalanced voltage conditions", *IET Generation, Transmission Distribution*, v. 12, pp. 1621–1630(9), April 2018. ISSN: 1751-8687. Disponível em: <`http://digital-library.theiet.org/content/journals/10.1049/iet-gtd.2017.0523`>.

[34] CAO, Y. Z., WANG, H. N., CHEN, B. "Unbalanced voltage control of virtual synchronous generator in isolated micro-grid", *IOP Conference Series: Materials Science and Engineering*, v. 211, n. 1, pp. 012020, 2017. Disponível em: <`http://stacks.iop.org/1757-899X/211/i=1/a=012020`>.

[64] ZHONG, Q. C., NGUYEN, P. L., MA, Z., et al. "Self-Synchronized Synchronverters: Inverters Without a Dedicated Synchronization Unit", *IEEE Transactions on Power Electronics*, v. 29, n. 2, pp. 617–630, Feb 2014. ISSN: 0885-8993. doi: 10.1109/TPEL.2013.2258684.

[36] LEONHARD, W. *Control of electrical drives.* Springer Science & Business Media, 2001.

[37] FERREIRA, R. V. *Comparative Analysis of Techniques to Emulate Synchronous Machines in Grid-connected Converters.* Tese de D.Sc., UFMG, Belo Horizonte, MG, Brasil, 2020.

[38] HIRASE, Y., SUGIMOTO, K., SAKIMOTO, K., et al. "Analysis of Resonance in Microgrids and Effects of System Frequency Stabilization Using a Virtual Synchronous Generator", *IEEE Journal of Emerging and Selected Topics in Power Electronics*, v. 4, n. 4, pp. 1287–1298, Dec 2016. ISSN: 2168-6777. doi: 10.1109/JESTPE.2016.2581818.

[39] ALIPOOR, J., MIURA, Y., ISE, T. "Distributed generation grid integration using virtual synchronous generator with adoptive virtual inertia", *2013 IEEE Energy Conversion Congress and Exposition, ECCE 2013*, pp. 4546–4552, 2013. doi: 10.1109/ECCE.2013.6647309.

[40] KUNDUR, P., BALU, N. J., LAUBY, M. G. *Power system stability and control*, v. 7. McGraw-hill New York, 1994.

[41] WANG, S., QI, R., LI, Y. "Fuzzy Control Scheme of Virtual Inertia for Synchronverter in Micro-Grid", *ICEMS 2018 - 2018 21st International Conference on Electrical Machines and Systems*, pp. 2028–2032, 2018. doi: 10.23919/ICEMS.2018.8549309.

[42] PIYA, P., KARIMI-GHARTEMANI, M. "A stability analysis and efficiency improvement of synchronverter". In: *Applied Power Electronics Conference and Exposition (APEC), 2016 IEEE*, pp. 3165–3171. IEEE, 2016.

[43] WEISS, G., NATARAJAN, V. "Modifications to the synchronverter algorithm to improve its stability and performance", *19th International Symposium on Power Electronics, Ee 2017*, v. 2017-Decem, n. 800, pp. 1–6, 2017. ISSN: 08908044. doi: 10.1109/PEE.2017.8171684.

[44] JIN-SONG MENG, SHU-HENG CHEN, CHANG-HUA ZHANG, et al. "An Improved Synchronverter Model and its Dynamic Behaviour Comparison with Synchronous Generator", *2nd IET Renewable Power Generation Conference (RPG 2013)*, pp. 4.13–4.13, 2013. ISSN: 0039-2499. doi: 10.1049/cp.2013.1879. Disponível em: <`http://digital-library.theiet.org/content/conferences/10.1049/cp.2013.1879`>.

[45] WANG, J., WANG, Y., GU, Y., et al. "Synchronous frequency resonance of virtual synchronous generators and damping control", *9th International Conference on Power Electronics - ECCE Asia: "Green World with Power Electronics", ICPE 2015-ECCE Asia*, pp. 1011–1016, 2015. ISSN: 0962-8452. doi: 10.1109/ICPE.2015.7167905.

[46] BRAHMA, A. R., KUMARAVEL, S., THOMAS, V., et al. "Impact of System Parameters on the Performance of Synchronverter", *Proceedings of 2019 IEEE Region 10 Symposium, TENSYMP 2019*, v. 7, pp. 120–125, 2019. doi: 10.1109/TENSYMP46218.2019.8971384.

[35] AOUINI, R., MARINESCU, B., KILANI, K. B., et al. "Improvement of transient stability in an AC/DC system with synchronverter based HVDC". In: *2015 IEEE 12th International Multi-Conference on Systems, Signals Devices (SSD15)*, pp. 1–6, March 2015. doi: 10.1109/SSD.2015.7348137.

[47] WEI, Z., JIE, C., CHUNYING, G. "Small signal modeling and analysis of synchronverters". In: *2015 IEEE 2nd International Future Energy Electronics Conference (IFEEC)*, pp. 1–5, Nov 2015. doi: 10.1109/IFEEC.2015.7361434.

[48] DONG, S., CHEN, Y. C. “A Method to Directly Compute Synchronverter Parameters for Desired Dynamic Response”, *IEEE Transactions on Energy Conversion*, v. 33, n. 2, pp. 814–825, 2018. ISSN: 08858969. doi: 10.1109/TEC.2017.2771401.

[49] MING, W. L., ZHONG, Q. C. “Synchronverter-based transformerless PV inverters”, *IECON Proceedings (Industrial Electronics Conference)*, pp. 4396–4401, 2014. doi: 10.1109/IECON.2014.7049164.

[50] ZHONG, Q.-C., MA, Z., MING, W.-L., et al. “Grid-friendly wind power systems based on the synchronverter technology”, *Energy Conversion and Management*, v. 89, pp. 719 – 726, 2015. ISSN: 0196-8904. doi: https://doi.org/10.1016/j.enconman.2014.10.027. Disponível em: <`http://www.sciencedirect.com/science/article/pii/S019689041400908X`>.

[51] BROWN, E., WEISS, G. “Using synchronverters for power grid stabilization”, *2014 IEEE 28th Convention of Electrical and Electronics Engineers in Israel, IEEEI 2014*, pp. 1–5, 2014. doi: 10.1109/EEEI.2014.7005736.

[52] LI, C., BURGOS, R., CVETKOVIC, I., et al. “Analysis and design of virtual synchronous machine based STATCOM controller”, *2014 IEEE 15th Workshop on Control and Modeling for Power Electronics, COMPEL 2014*, pp. 1–6, 2014. doi: 10.1109/COMPEL.2014.6877134.

[53] LI, C., BURGOS, R., CVETKOVIC, I., et al. “Design, analysis and experimental evaluation of a virtual-synchronous-machine-based STATCOM with LCL filter”, *2015 IEEE Energy Conversion Congress and Exposition, ECCE 2015*, pp. 5771–5778, 2015. doi: 10.1109/ECCE.2015.7310470.

[54] LI, C., BURGOS, R., CVETKOVIC, I., et al. “Evaluation and control design of virtual-synchronous-machine-based STATCOM for grids with high penetration of renewable energy”, *2014 IEEE Energy Conversion Congress and Exposition, ECCE 2014*, pp. 5652–5658, 2014. doi: 10.1109/ECCE.2014.6954176.

[55] AKAGI, H., WATANABE, E. H., AREDES, M. *Instantaneous power theory and applications to power conditioning*, v. 62. John Wiley & Sons, 2017.

[56] ZMOOD, D. N., HOLMES, D. G. “Stationary frame current regulation of PWM inverters with zero steady-state error”, *IEEE Transactions on Power Electronics*, v. 18, n. 3, pp. 814–822, May 2003. ISSN: 0885-8993. doi: 10.1109/TPEL.2003.810852.

[57] ANEEL. "Procedimentos de Distribuição de Energia Elétrica no Sistema Elétrico Nacional - PRODIST, Módulo 8 Qualidade da Energia Elétrica". Disponível em: <`https://www.aneel.gov.br/modulo-8`>.

[58] SEIPHETLHO, T. E., RENS, A. P. J. "On the assessment of voltage unbalance". In: *Proceedings of 14th International Conference on Harmonics and Quality of Power - ICHQP 2010*, pp. 1–6, Sept 2010. doi: 10.1109/ICHQP.2010.5625366.

[59] PANSAKUL, C., HONGESOMBUT, K. "Analysis of voltage unbalance due to rooftop PV in low voltage residential distribution system", *2014 International Electrical Engineering Congress, iEECON 2014*, , n. 2, pp. 1–4, 2014. doi: 10.1109/iEECON.2014.6925883.

[60] KLAYKLUENG, T., DECHANUPAPRITTHA, S. "Impact analysis on voltage unbalance of EVs charging on a low voltage distribution system", *2014 International Electrical Engineering Congress, iEECON 2014*, pp. 1–4, 2014. doi: 10.1109/iEECON.2014.6925899.

[61] HSU, S. M. "Discussion of "Using a Static Var Compensator to Balance a Distribution System"", *IEEE Transactions on Industry Applications*, v. 35, n. 5, pp. 1174–1176, 1999. ISSN: 19399367. doi: 10.1109/28.793380.

[62] LEE, G. M., LEE, D. C., SEOK, J. K. "Control of Series Active Power Filters Compensating for Source Voltage Unbalance and Current Harmonics", *IEEE Transactions on Industrial Electronics*, v. 51, n. 1, pp. 132–139, 2004. ISSN: 02780046. doi: 10.1109/TIE.2003.822040.

[63] XU, Y., TOLBERT, L. M., KUECK, J. D., et al. "Voltage and current unbalance compensation using a static var compensator", *IET Power Electronics*, v. 3, n. 6, pp. 977–988, 2010. ISSN: 17554535. doi: 10.1049/iet-pel.2008.0094.

[65] MA, Z., ZHONG, Q. C., YAN, J. D. "Synchronverter-based control strategies for three-phase PWM rectifiers". In: *2012 7th IEEE Conference on Industrial Electronics and Applications (ICIEA)*, pp. 225–230, July 2012. doi: 10.1109/ICIEA.2012.6360727.

[66] GOLNARAGHI, F., KUO, B. C. *Automatic Control Systems*. Wiley Publishing, 2009. ISBN: 0470048964.

[67] PIYA, P., KARIMI-GHARTEMANI, M. "A stability analysis and efficiency improvement of synchronverter". In: *2016 IEEE Applied Power Electron-*

*ics Conference and Exposition (APEC)*, pp. 3165–3171, March 2016. doi: 10.1109/APEC.2016.7468317.

[68] FRANÇA, B. W. *Static Synchronous Generator with Sliding Droop Control for Distributed Generation in Microgrids.* Tese de D.Sc., COPPE/UFRJ, Rio de Janeiro, RJ, Brasil, 2016.

[69] DE KELPER, B., DESSAINT, L. A., AL-HADDAD, K., et al. "A comprehensive approach to fixed-step simulation of switched circuits", *IEEE Transactions on Power Electronics*, v. 17, n. 2, pp. 216–224, 2002. ISSN: 08858993. doi: 10.1109/63.988832.

[70] LIAN, K. L., LEHN, P. W. "Real-time simulation of voltage source converters based on time average method", *IEEE Transactions on Power Systems*, v. 20, n. 1, pp. 110–118, 2005. ISSN: 08858950. doi: 10.1109/TPWRS.2004.831254.

[71] MARTI, J. R., LIN, J. "Suppression of numerical oscillations in the EMTP power systems", *IEEE Transactions on Power Systems*, v. 4, n. 2, pp. 739–747, May 1989. ISSN: 0885-8950. doi: 10.1109/59.193849.

[72] DE SIQUEIRA, J. C. G., BONATTO, B. D., MARTÍ, J. R., et al. "A discussion about optimum time step size and maximum simulation time in EMTP-based programs", *International Journal of Electrical Power and Energy Systems*, v. 72, pp. 24–32, 2015. ISSN: 01420615. doi: 10.1016/j.ijepes.2015.02.007.

[73] RODRIGUEZ, P., LUNA, A., ETXEBERRÍA, I., et al. "Multiple second order generalized integrators for harmonic synchronization of power converters", *2009 IEEE Energy Conversion Congress and Exposition, ECCE 2009*, , n. 1, pp. 2239–2246, 2009. doi: 10.1109/ECCE.2009.5316279.

[74] MOHAN, N., UNDELAND, T., ROBBINS, W. *Power Electronics: Converters, Applications, and Design.* Power Electronics: Converters, Applications, and Design. John Wiley & Sons, 2003. ISBN: 9788126510900. Disponível em: <`https://books.google.com.br/books?id=oxR8vB2XjgIC`>.

[75] CORSO, T. C. "Projeto e Implementação de um Filtro Ativo Monofásico para Compensação de Harmônicos de Corrente". 2017.

# Appendix A

# Space Vector Concept

Vector representation is a widely used technique in the field of power electronics [55]. It consists of taking time varying quantities to compose vectors on the complex plane. For instance, consider the set of three-phase balanced sinusoidal voltages

$$\begin{aligned} v_a &= V_o \sin(\omega t + \phi_V), \\ v_b &= V_o \sin(\omega t + \phi_V - 2\pi/3), \\ v_c &= V_o \sin(\omega t + \phi_V - 4\pi/3), \end{aligned} \tag{A.1}$$

where $V_o$ is the voltage amplitude, $\omega$ the angular frequency and $\phi_V$ the phase. A space vector representation of this voltages will be

$$\underline{\mathbf{v}}_{abc} = v_a e^{j0} + v_b e^{j2\pi/3} + v_c e^{j4\pi/3}, \tag{A.2}$$

where $e^{j2n\pi/3}, \quad n = 0, 1, 2$ is a unitary complex phase shifter. By replacing (A.1) in (A.2) and using the identity $e^{j\theta} = \cos(\theta) + j\sin(\theta)$, the voltage vector $\underline{\mathbf{v}}_{abc}$ can be rewritten as

$$\underline{\mathbf{v}}_{abc} = \frac{3}{2} V_o [\cos(\omega t + \phi_V) + j\sin(\omega t + \phi_V)] = \frac{3}{2} V_o e^{j(\omega t + \phi_V)}, \tag{A.3}$$

demonstrating that the voltage vector $\mathbf{v}_{abc}$ has constant amplitude and rotates with the same angular frequency $\omega$, direction and sequence of the time varying voltages (A.1). Now, when applying the Clarke's power invariant and amplitude invariant transformations to voltages (A.1), it results in the following:

$$Power\ Invariant \rightarrow \begin{cases} v_\alpha = \sqrt{\frac{3}{2}} V_o \cos(\omega t + \phi_V) \\ v_\beta = \sqrt{\frac{3}{2}} V_o \sin(\omega t + \phi_V) \end{cases} ; \tag{A.4}$$

$$Amplitude\ Invariant \rightarrow \begin{cases} v_\alpha = V_o \cos(\omega t + \phi_V) \\ v_\beta = V_o \sin(\omega t + \phi_V) \end{cases}. \tag{A.5}$$

Notice that the $\alpha$ and $\beta$ components of both Clarke transformations are similar to the real and imaginary parts of A.3, respectively. This means they can compose a vector in the complex plane that rotates in the same way (A.3) does, and has the form:

$$\mathbf{v}_{\alpha\beta} = v_\alpha + jv_\beta. \tag{A.6}$$

Therefore, the relationships between norms, i.e amplitudes of the space vector representation and Clarke's complex vectors are:

$$Power\ Invariant \rightarrow \mathbf{v}_{\alpha\beta} = \sqrt{\frac{2}{3}}\underline{\mathbf{v}}_{abc}, \tag{A.7}$$

$$Amplitude\ Invariant \rightarrow \mathbf{v}_{\alpha\beta} = \frac{2}{3}\underline{\mathbf{v}}_{abc}. \tag{A.8}$$

Now, consider the following set of three-phase currents:

$$\begin{aligned} i_a &= I_o \sin(\omega t + \phi_I), \\ i_b &= I_o \sin(\omega t + \phi_I - 2\pi/3), \\ i_c &= I_o \sin(\omega t + \phi_I - 4\pi/3), \end{aligned} \tag{A.9}$$

where $I_o$ is the current amplitude, $\omega$ is the angular speed and $\phi_I$ the phase. By creating the $\mathbf{i}_{abc}$ space vector as in (A.2) along with complex vectors using each of the Clarke's transformations, apparent power $S = \mathbf{vi}^*$ can be calculated and compared for each representation. Active and reactive power as stated by the instantaneous power theory [55] uses Clarke's power invariant transformation and will be used as baseline for comparison:

$$\begin{aligned} \mathbf{v}_{\alpha\beta}\mathbf{i}^*_{\alpha\beta} &= v_\alpha i_\alpha + v_\beta i_\beta + j(v_\beta i_\alpha - v_\alpha i_\beta) \\ &= \frac{3}{2}V_o I_o \cos(\phi_V - \phi_I) + j\frac{3}{2}V_o I_o \sin(\phi_V - \phi_I) \\ &= P_{3\phi} + jQ_{3\phi}, \end{aligned} \tag{A.10}$$

where $P_{3\phi}$ is the three-phase active power of the system and $Q_{3\phi}$ is the three-phase reactive power. If the same calculation os repeated for voltages and currents represented in Clarke's amplitude invariant transformation, active and reactive power would result in:

$$\begin{aligned}\mathbf{v}_{\alpha\beta}\mathbf{i}^*_{\alpha\beta} &= v_\alpha i_\alpha + v_\beta i_\beta + j(v_\beta i_\alpha - v_\alpha i_\beta) \\ &= V_o I_o \cos(\phi_V - \phi_I) + jV_o I_o \sin(\phi_V - \phi_I) \\ &= \frac{2}{3}P_{3\phi} + j\frac{2}{3}Q_{3\phi}.\end{aligned} \tag{A.11}$$

As for the space vector representation, active and reactive power are:

$$\begin{aligned}\underline{\mathbf{v}}_{abc}\underline{\mathbf{i}}^*_{abc} &= \left(\frac{3}{2}\right)^2 V_o I_o e^{j(\phi_V - \phi_I)} \\ &= \left(\frac{3}{2}\right)^2 V_o I_o \cos(\phi_V - \phi_I) + j\left(\frac{3}{2}\right)^2 V_o I_o \sin(\phi_V - \phi_I)\cdot \\ &= \frac{3}{2}P_{3\phi} + j\frac{3}{2}Q_{3\phi}\end{aligned} \tag{A.12}$$

In conclusion, a control strategy on the stationary frame of reference using Clarke's power invariant transformation will be in compliance with the instantaneous power theory, with power calculations representing the actual three-phase power of the controlled system but stationary frame voltage and current amplitudes scaled by a $\sqrt{3/2}$ factor compared to the actual phase amplitudes. However, if the control uses Clarke's amplitude invariant transformation, stationary frame components amplitudes will match the actual phase amplitudes, but calculated power will represent only 2/3 of the three-phase power, meaning that a reference value for a power control loop would need so be scaled by 3/2 to compensate. As for the space vector representation, calculated power represents 3/2 of the actual three-phase power and stationary frame components amplitudes are also scaled by 3/2 in comparison with the actual phase values. But notice that if a control strategy based in a space vector model is fed with quantities in the stationary reference frame represented by Clarke's amplitude invariant transformation, their scaling factors cancel out and calculated power will represent the actual three-phase power of the system, besides the stationary frame components amplitudes of voltages and currents matching the actual phase values.